Master's thesis

NTNU
Norwegian University of Science and Technology
Faculty of Engineering
Department of Geoscience and Petroleum

Nandito Davy

Velocity Depth Trends Prediction on the Norwegian Continental Shelf (NCS) Wells Using the Bounding Average Method

Master's thesis in Petroleum Geosciences (MSG2)
Specialization: Petroleum Geophysics
Supervisor: Kenneth Duffaut
June 2021

NTNU
Norwegian University of
Science and Technology

Nandito Davy

Velocity Depth Trends Prediction on the Norwegian Continental Shelf (NCS) Wells Using the Bounding Average Method

Master's thesis in Petroleum Geosciences (MSG2)
Specialization: Petroleum Geophysics
Supervisor: Kenneth Duffaut
June 2021

Norwegian University of Science and Technology
Faculty of Engineering
Department of Geoscience and Petroleum

NTNU

Kunnskap for en bedre verden

Preface

This thesis is submitted as one of the fulfillment requirements for the degree Master of Sciences (MSc) at the Norwegian University of Science and Technology (NTNU). The MSc thesis is carried out at the Department of Geoscience and Petroleum Engineering in Trondheim, Norway. The general theme of the MSc thesis is designed for the specialization of Petroleum Geophysics. The MSc thesis is titled "**Velocity Depth Trends Prediction on the Norwegian Continental Shelf (NCS) Wells Using the Bounding Average Method**". This thesis's main objective is to proposed and implemented a complete methodology to predict the velocity depth trends in vertically transversely isotropic (VTI) media, combining rock-physics models and petrophysical depth trends from the borehole data.

I want to thank my supervisor, Professor Kenneth Duffaut, for sharing his knowledge and experience and 20 weekly productive and enlightening meetings throughout the semester. He helped me by giving me guidance and inspiration to be a better geophysicist in many aspects, both professionally and academically. It would be a privilege for me if someday I can work and cooperate again with Professor Kenneth Duffaut in other exciting opportunities or challenges ahead. I always remember one jargon from him: "*The devil is in the detail*", where it motivates me to write everything in a detailed mannered as possible. No detail is left behind, and everything must be justified.

I would also like to thank my parents in Indonesia, Onnie Ridaliani and Khairul Anwar. Without their support, both material and moral, I would not finish this MSc thesis. One motivation that pushes me to pursue this degree is that I want to make my parent proud to have me as their only son in this world. By obtaining this MSc degree, I feel that I accomplished one of the goals of my life. However, finishing this MSc thesis is not an end; instead, it is a sign of entering a new phase of my life. I am looking forward to landing a job or pursuing a Ph.D. degree everywhere in the world. I will give my best in every given circumstance. As a Muslim, I believe that Allah will give me something that I deserved to have, which not necessary or always means something that I want, as long as I give my total effort and strong faith to Allah.

The COVID situation in Indonesia is still in a terrible situation. Vaccination is in process, and I grateful that both of my parents had already received their doses. I hope that all the people in Indonesia, Norway, and other countries in the world could obtain their doses as soon as possible. All in all, it was an unforgettable memory to be able to study at NTNU. I send my sincere prayers for everybody who helped me along the way, especially for Professor Kenneth Duffaut and my parents in Indonesia.

Trondheim, June 2021.

Nandito Davy

"Tesis S2 ini Davy persembahkan untuk ibu dan ayah di Indonesia. Semoga Davy selalu bisa menjadi individu yang tidak lupa bersyukur kepada Allah, tidak sombong, dan selalu giat bekerja keras. Terima kasih untuk pengorbanan yang telah diberikan sejak Davy lahir sampai saat ini bisa menyelesaikan pendidikan S2 di Norwegia. Semoga Davy bisa terus berbakti kepada Ibu dan Ayah hingga waktu memisahkan kita semua."

- Nandito Davy, 2021

English translation: *This Master's thesis is specifically present for both of my parents in Indonesia. I always aim to be a person who never forgets to count Allah's blessings, not arrogant, and simultaneously always working hard for any given challenges. I wholeheartedly thank my parents for their sacrifices from when I was born until I finished this MSc degree in Norway. I hope that I could always devote myself to my parents until time separates all of us.*

Abstract

Earth consists of heterogeneous layers due to the complex sedimentation processes, in which lithifies both unconsolidated sand and siliciclastic clays into sandstone and shale. These two sedimentary rocks are the most abundant in the hydrocarbon reservoir, usually in the form of shaly sand or sandy shale mixture. As the advantage of the technology, geophysicists can distinguish these sedimentary rocks by using a seismic reflection method that relies on their elastic properties; P-wave (V_p) and S-wave (V_s) velocities along with density. One option to estimate these velocities are from both compressional and shear sonic logs since these two are reciprocal to the elastic velocities. However, sonic logs may not be available or partially available at specific depth intervals. Lack of these measurements could potentially be problematic for geophysicists that need accurate velocity estimations.

Many rock-physics-based empirical approaches are available for elastic velocities estimations, relying on other parameters such as porosity (ϕ), clay volume (V_{cl}), differential stress (σ'), et cetera. However, these empirical approaches are only valid and optimum in the dataset they are using. Therefore, these empirical approaches are susceptible to the robustness issue. We propose a methodology to estimate the vertical velocity depth trends for the three wells taken from the Norwegian Continental Shelf (NCS). The proposed methodology mainly utilizes the rock-physics analysis of Voight-Reuss Bounds and the Bounding Average Method (BAM). It also implements the petrophysical analysis to estimate the lithological volume fraction of sand, clay, and silt. We designed two different models, namely the implicit and explicit clay-bound water.

The challenges of this proposed methodology are to simulate the depositional variations between (1) Clean sand and clay; (2) Consolidation states as the rock changes from freshly deposited and later compacted; and (3) Velocity stress-sensitivity along with the burial depth. This proposed methodology yield correlation coefficients and error percentages, respectively between 0.7326 - 0.9521 and 7.73% - 15.07% for V_p; and respectively between 0.7495 - 0.9585 and 16.2% - 27.66% for V_s. These values show that the methodology is reliable but straightforward enough to perform robust predictions for the vertically-propagating elastic velocity depth trends.

Table of Content

List of Figures

List of Tables

List of Equations

1 Introduction

Earth consists of heterogeneous layers due to the complex sedimentation processes in a certain period of geological events, between thousands to millions of years. The layers were once initially deposited as the unconsolidated sediments, in which, as the process continues, the younger sediments gradually buried the older sediments. Changes in temperature and pressure are the main factors that transform the unconsolidated sediments into consolidated rocks. Hence, both the unconsolidated sand and siliciclastic clay are lithified into sandstone and shale (Rieke and Chilingarian, 1974; Magara, 1980; Bjørlykke, 1989; Mondol et al., 2007; Duffaut, 2011).

Sandstone is one of the most common hydrocarbon-bearing reservoir rocks, where around 50 - 60% of hydrocarbon reserves globally are found within the sandstone reservoir (Berg, 1986; McDonald and Schmidt, 1991). Several studies show that the sandstone is the primary lithology for Norwegian hydrocarbon reservoir (Nystuen and Fält, 1995; Odden et al., 1998; Grogan et al., 1999). On the other hand, shale is the most common sedimentary rock, where it could be deposited in any environment such as river floodplain, lake, delta, marine shelf, deep marine, et cetera (Tucker, 2003). Due to their abundance in nature, it is reasonable for sandstone and shale to be mixed. Therefore, it is beneficial to have excellent understandings of these two sedimentary rocks.

As the advantage of technology, Geophysics is now one of the vital elements in hydrocarbon exploration. Geophysicists could implement a seismic survey based on the principle of reflectivity, known as the seismic reflection method. This method depends on the elastic waves' (P-wave (V_p) and S-wave (V_s) velocities) propagation through the earth's layers, where the waves are reflected due to an impedance contrast between two layers. In practice, both V_p and V_s are calculated based on specific well log data, respectively the compressional and shear sonic log. The sonic log describes the transit time between a transmitter that emits a sound pulse and a receiver that records the pulse as it passes the receiver. This transit time could also be considered as the slowness, which is a reciprocal of the sound wave's velocity (Schlumberger, 1990). However, it is possible for the sonic log data of a well is not available or partially available only on a specific depth interval. Furthermore, the sonic tool's measurement might also have shortcomings due to the significant acoustic discontinuity within the borehole. The sonic log's flaw could potentially be problematic for geophysicists that need accurate estimations of elastic velocities.

Various rock-physics-based empirical approaches for the elastic wave velocities estimation are developed from the laboratory measurement and in-situ data: based on the time-average equation (Wyllie et al., 1955); the velocity to traveltime relation (Raymer et al., 1980); regression of the porosity and clay content for shaly sandstones (Han, 1986; Eberhart-Phillips et al., 1989; Tosaya and Nur, 1982); regression of the porosity and clay content under water-saturated condition (Castagna et al., 1985); data compilation of the crustal rocks (Brocher, 2005); arithmetic and harmonic means of the lithology's pure constituent (Greenberg and Castagna, 1992); and the V_p - V_s relation (Castagna et al., 1993; Vernik and Fisher, 2002; Williams, 1990; Xu and White, 1996). However, empirical ap-

proaches only valid and optimum for the dataset they used. Hence, empirical approaches are susceptible to the robustness issue.

By realizing the drawbacks of the sonic log and the robustness of the empirical approaches, this study aims to develop a methodology to predict the vertically-propagating velocity depth trends based on the available borehole logs. The proposed methodology is based on several rock-physics models, with the most crucial one is the Bounding Average Method or BAM (Marion, 1990). The BAM depends on a fitting parameter or weight parameter that acts as the balance between the Reuss (1929) Bound and the Voigt (1928) Bound. These Voigt-Reuss bounds differentiate stiffer sand and softer shale. This study also proposes a physical explanation for the appropriate weight parameters. Some petrophysical approaches are included for the proposed methodology, particularly the estimation for clay content based on lithological baselines and neutron porosity log (La Vigne et al., 1994). Several similar studies for the velocity predictions could be seen on Durrani et al. (2014), Egemen (2015), and Guo and Li (2015). However, none of these references uses the BAM in their procedures, and they only focus on V_s prediction.

Stress sensitivity of sedimentary rocks is also considered inside the proposed methodology, where it is linked primarily to porosity and elastic velocity changes. Han (1986) and Dong et al. (2010) show that the stress sensitivity of porosity for sand is significantly greater than that for shale. Additionally, MacBeth (2004) shows the stress sensitivity of both bulk and shear modulus of sandstone samples, where unconsolidated higher-porosity samples tend to be more stress sensitive than that for the consolidated samples. Dvorkin and Nur (2000) state that the higher-porosity sandstone follows the critical porosity concept. Since the elastic velocities are the function for Poisson's ratio, where those are related to the porosity and elastic moduli, it is decided to include stress-sensitivity prediction based on the Poisson's ratio and critical porosity.

The challenges of this proposed methodology are to simulate the depositional variations between (1) Clean sand and clay, based on the Voigt-Reuss bounds; (2) Consolidation states as the rock changes from freshly deposited and later compacted, based on the Poisson's ratio and critical porosity; (3) Stress sensitivity following the burial depth, based on the Poisson's ratio and the weight parameters from the BAM. Therefore, this proposed methodology is reliable but straightforward enough to perform robust elastic velocity predictions.

This thesis is organized as follows: First, the related theoretical explanations of the proposed methodology. Second, the database overview for the three wells from the Norwegian Continental Shelf (NCS). Third, the proposed methodology workflow is discussed based on the implicit and explicit clay-bound water models. Fourth, the results of the applied workflow, comparing modeled vertically-propagating velocity depth trends with corresponding depth trends of wellbore measurements of the wells. Fifth, the discussions for the obtained results. Sixth, the conclusions and the further works from this study. The results show that both models can predict the vertically-propagating V_p and V_s with correlation coefficients from 0.7326 to 0.9585 and error percentages from 7.73% to 27.66%.

2 Theory

2.1 Bounding Model: Voight and Reuss Bounds

Three parameters need to be specified to theoretically predict the effective moduli of a mixture, namely the volume fractions, the elastic moduli, and the geometric details of the various phases (Mavko et al., 2009). However, in practice, only the volume fractions and the constituent moduli are available; hence, the reasonable approach to approximate the mixture's effective moduli is by using both the upper and lower bounds, as shown in Figure 1. Thus, the mixture's effective moduli would be found between the bounds, where the upper and lower bounds respectively describe the stiffer and softer moduli. This thought of using both the lower and upper bounds to predict the effective moduli is called the Bounding Model. However, the major shortcoming of this model is the absence of geometrical consideration within the model.

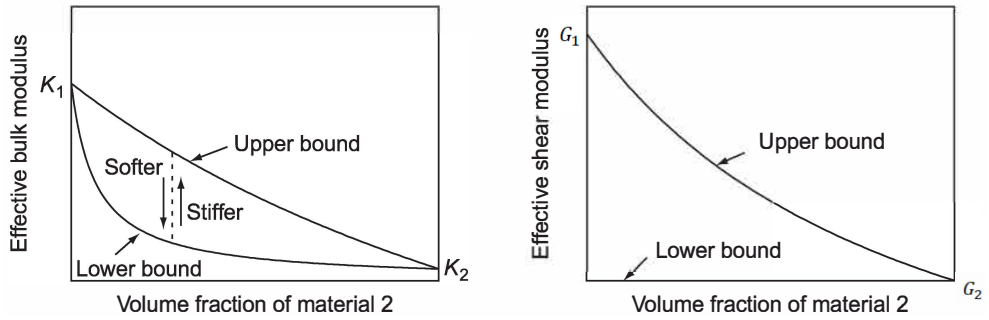

Figure 1: The upper and lower bounds for effective bulk modulus (left) and shear modulus (right). (Modified from Mavko et al. 2009)

The upper bound is considered as the Voigt (1928) Bound or the isostrain average, where the constituents are exposed to the same strain. On the other hand, the lower bound is considered as the Reuss (1929) Bound or the isostress average where the constituents are exposed to the same stress. Figure 2 shows the physical illustration for both Voigt and Reuss bound.

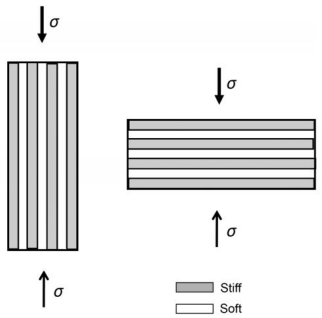

Figure 2: The physical illustrations for Voigt Bound (left) and Reuss Bound (right). (taken from Castagna et al., 2014)

The general equations for the Voigt (M_V) and Reuss (M_R) Bounds of the effective elastic modulus, based on the i-th given volume fraction (f_i) and elastic modulus (M_i), are seen in Equations 1 and 2, respectively.

$$M_V = \sum_{i=1}^{N} f_i M_i \tag{1}$$

$$M_R = \sum_{i=1}^{N} \frac{f_i}{M_i} \tag{2}$$

The Voigt and Reuss Bounds are useful for several purposes, such as estimating the range of the average mineral moduli for a mixture of mineral grains and the upper-lower bounds for a combination between mineral and pore fluids. This model assumes that the constituents are isotropic, linear, and elastic.

2.2 Bounding Average Method (BAM)

Marion (1990) conducts some studies for the dependence of velocity by several parameters such as (1) porosity and compaction, (2) clay content, (3) packing properties and coordination number, and (4) fluid types. He discovers that these parameters are not independent of each other. Therefore, a complete understanding of one given property's influence on velocity is a complex problem that requires knowledge of the relationship between the mentioned dependent parameters.

Marion realizes the dependence of elastic properties on porosity is not a simple relationship; therefore, he proposes a heuristic approach based on a theoretical bound for estimating the elastic moduli and velocities, called the Bounding Average Method or BAM. This method recognizes that at any given volume fraction of constituents, the effective moduli fall between the bounds, where the precise value depends on the geometric detail of the grains and pores (Mavko et al., 2009). Marion proposes a weighted modulus ($M_{weighted}$) based on a weight parameter or W, as seen in Equation 3.

$$W = \frac{M_{weighted} - M_{lower}}{M_{upper} - M_{lower}}$$

$$M_{weighted} = M_{lower} + W\ (M_{upper} - M_{lower}) \tag{3}$$

A crucial remark about Equation 3 is that the weight parameter (W) acts as a fitting parameter. If W sets to be 0, then the weighted moduli become the lower moduli. On the contrary, if it sets to 1, then the weighted moduli become the upper moduli. From this behavior of the weighted equation, we can see that every dataset might use different W from one and the others; this could potentially be a problem for a prediction model. Therefore, we are proposing the physical definition of how to estimate the W.

It is challenging to model the elastic properties of clay-rich sediments due to their complexity concerning the mineral composition. We propose a new twist to this challenge by combining the BAM itself with elastic Voigt-Reuss bounds based on Vernik and Kachanov (2010) approach; hence, the general equation for the BAM (Equation 3), particularly for the vertically-propagating anisotropic P-wave modulus or C_{33}, could be rewritten as shown below.

$$C_{33} = C_{33,Reuss} + W_{C_{33}}(C_{33,Voigt} - C_{33,Reuss}) \tag{4}$$

Analogous to the general BAM equation, Equation 4 also has W as its fitting parameter, where the C_{33} would be equal to the softer bound (Reuss bound) if W sets to be 0, and the C_{33} would be equal to the stiffer bound (Voigt bound) if W sets to be 1. It is important to realize that Equation 4 is a modified BAM based on the bounding model mentioned in subchapter 2.1. Therefore, the equation only specifies the elastic moduli and the volume fraction, leaving the geometrical detail behind. To rectify this drawback, we would physically define the fitting parameters (weight parameter) by including the Poisson's ratio and the modified critical porosity, as later shown in the following chapters, where W acts as the primary mechanism to estimate geometrical detail. As previously seen in Equation 4, the C_{33} for the Reuss and Voigt bounds are shown in Equations 5 and 6, respectively.

$$C_{33,Reuss} = \left[(1-\phi)\left[\frac{V_{cl}}{C_{33,cl}} + \frac{(1-V_{cl})}{M_{non-cl}}\right] + \frac{\phi}{K_{fl}}\right]^{-1} \tag{5}$$

$$C_{33,Voigt} = (1-\phi)[V_{cl}\ C_{33,cl} + (1-V_{cl})\ M_{non-cl}] + \phi K_{fl} \tag{6}$$

Where ϕ is the porosity, V_{cl} is the clay volume, K_{fl} is the fluid's bulk modulus, $C_{33,cl}$ is a vertically-propagating anisotropic P-wave modulus for the clay compartment, and M_{non-cl} is an isotropic P-wave parameter for the non-clay compartment. Both equations consist of solid and pore-fluid compartments, respectively shown with terms of '$1-\phi$' and 'ϕ'. An essential remark from these equations is that they violate the isotropic Voigt-Reuss assumption since they only calculate the property of the vertically propagating velocity; hence, the model assumes that the isotropic M_{non-cl} is equivalent to the anisotropic $C_{33,non-cl}$.

2.3 Effective, Total, and Critical porosity

Porosity is one of the important parameters for sedimentary rock, which describes the reservoir's storage capacity. Tiab and Donaldson (2004) state that the porosity could mathematically be defined as the fraction of the bulk volume of the reservoir that is not occupied by the solid framework of the reservoir, as shown in Equation 7.

$$\phi = \frac{V_b - V_{gr}}{V_b} = \frac{V_{pore}}{V_b} \tag{7}$$

Where ϕ is the porosity, V_b is the bulk volume of the reservoir, V_{gr} is the grain volume, and V_{pore} is the pore volume. The typical porosity of sedimentary rocks is lower than 50%. Furthermore, Schlumberger (1990) provides the typical porosity values for several lithologies: practically zero porosity for dense carbonate (limestone and dolomite) and evaporite (salt, anhydrite, gypsum, sylvite, et cetera.); 10 to 15% for well-consolidated sandstone; around or more than 30% for unconsolidated sandstone; and around or more than 40% for water-filled shale or clay.

Several parameters affect the porosity of sedimentary rocks at the time of its deposition, such as the size, shape, degree of uniformity of size and shape, and the mode of grain's packing (Athy, 1930). For example, the porosity for fine materials would be very high. At the same time, the bulk density is very low due to the enormous surface area and the irregularity of the grains' shape. For sand, the porosity is independent of the coarseness since the grains typically have a similar spherical shape; hence, the highest porosity sand is coarse and even-textured. Other parameters that affect the porosity after the deposition and burial process are closer spacing of grains, deformation or granulation of grains, re-crystallization, secondary growth, and cementation.

2.3.1 Porosity and Well Log

In practice, the porosity could be obtained either from the density log or the neutron porosity log. A density log is a continuous record of a formation's bulk density, representing the density of the minerals or matrix and the volume of free fluids it encloses (Rider, 1999). From this log, then the porosity could be calculated as shown in Equation 8.

$$\phi_D = \frac{\rho_{ma} - \rho_b}{\rho_{ma} - \rho_{fl}} \tag{8}$$

Where ϕ_D is the density porosity, ρ_{ma} is the matrix (or grain) density, ρ_{fl} is the fluid density, and ρ_b is the measured bulk density. It is a common practice to define the ρ_{fl} as water (ρ_w), with a density of 1 g/cc. As for the ρ_{ma}, it is common to use the value from

the density of quartz, 2.65 g/cc, according to Mavko et al. (2009). The neutron log is a continuous record of a formation's reaction to fast neutron bombardment related to the hydrogen index or richness in hydrogen (Rider, 1999). Due to its nature, then the neutron log is measuring the formation's water content. Therefore, the neutron porosity is a real porosity for clean limestone, where the other lithologies need some conversion factors.

2.3.2 Effective and Total Porosity

In a shaly sand reservoir, it is expected for several minerals to be present in the solid compartment, such as quartz, mica, feldspar, and clay. For the clay itself, it could be further classified into dry clay and clay-bound water. The non-solid compartment consists of either free water, hydrocarbon, or both. In this regard, the porosity could be classified into two different terms based on the fluid's mobility, namely, effective porosity and total porosity.

Simm (2007) states that effective porosity is defined as the moveable fluid in the rock. In contrast, total porosity is defined as the combination of effective porosity and bound water. Similarly, Ezekwe (2010) states that effective porosity is the total porosity less the fraction of pore space occupied by shale or clay. In contrast, total porosity is defined as the ratio of the entire pore space in a rock to its bulk volume. From these two references, it is clear that the existence of bound water inside the shale or clay is the main difference between the two terms, where effective porosity excludes it, and the total porosity includes it. A schematic diagram for both effective and total porosity in a shaly sand reservoir is shown in Figure 3, where the total volume (V_{total}) could be defined as stated in Equation 9.

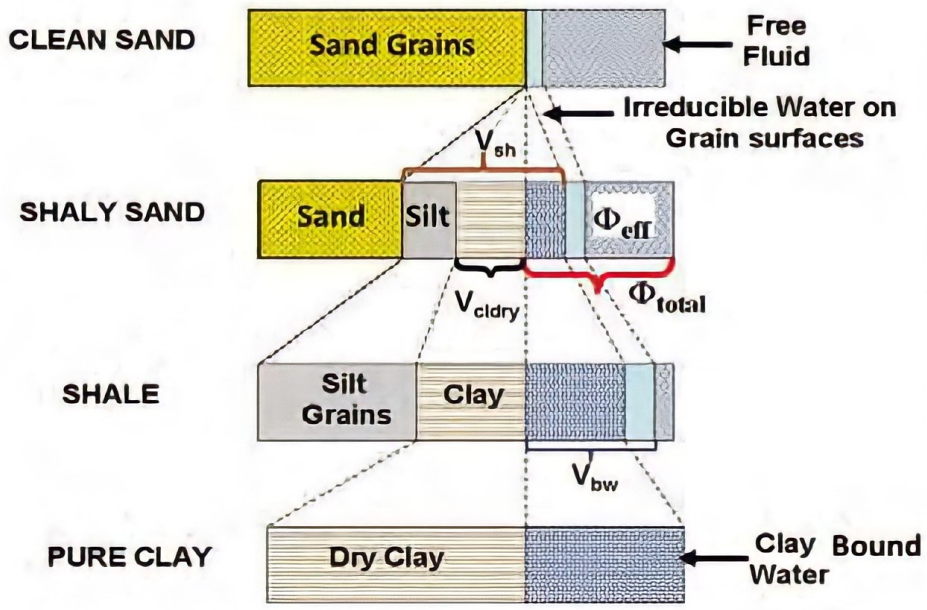

Figure 3: Schematic diagram for effective and total porosity in a shaly sand reservoir (Taken from Peeters and Holmes, 2014)

$$V_{total} = V_{sand} + V_{shale} + \phi_{effective} \tag{9}$$

Where V_{sand} and V_{shale} are respectively the volume fraction for sand and shale, assuming that the irreducible water on grain surface belongs inside the V_{shale}. Both Simm and Ezekwe agree that the effective porosity is obtained from the density porosity (Equation 8), so that:

$$\phi_{effective} = \phi_D \tag{10}$$

However, they have slightly different equations to calculate the total porosity, respectively shown in Equations 11 and 12.

$$\phi_{total} = \phi_{effective} + V_{shale}(1 - \phi_{effective}) \left(\frac{\rho_{cl} - \rho_{sh}}{\rho_{cl} - \rho_w} \right) \tag{11}$$

$$\phi_{total} = \phi_{effective} + V_{shale} \; \phi_{total} = \phi_{effective} + V_{cbw} \tag{12}$$

Where ρ_{sh} is the shale density, ρ_{cl} is the dry clay density, and V_{cbw} is the clay-bound water volume. Ezekwe suggested that the elemental capture spectroscopy (ECS) log could be used to estimate the effective porosity and clay-bound water volume more accurately. There is also another way to estimate the effective porosity based on the cation exchange capacity, proposed by Hill et al. (1979) and Juhasz (1979), as shown in Equation 13.

$$\phi_{effective} = \phi_{total} \left[1 - \left(\frac{0.084}{\sqrt{C_0}} + 0.22 \right) \frac{Q_v}{\rho_{cbw}} \right] \tag{13}$$

Where Q_v is the cation exchange capacity, ρ_{cbw} is the density of the clay-bound water, and C_0 is the salinity of the formation water. Later in this thesis, The total porosity is estimated from the summation of the effective porosity and the clay-bound water volume. The latter is obtained from the multiplication of dry-clay volume fraction (V_{dry-cl}) and the average dry-clay neutron porosity ($\phi_{N,dry-cl}$), as seen in Equation 14. The effective porosity is equal to the density porosity, the same concept as Equation 10. The $\phi_{N,dry-cl}$ for four typical clay types is shown in Table 1. Hence, the value of $\phi_{N,dry-cl}$ then can be calculated as shown in Equation 15.

$$\phi_{total} = \phi_{effective} + V_{cbw} = \phi_{effective} + V_{dry-cl} \cdot \phi_{N,dry-cl} \tag{14}$$

Table 1: The neutron log values of some common clay types, taken from Weaver and Pollard (1973), Serra (1979), and Rider (1999).

Clay type	% Water Average	Hydrogen Index	Neutron porosity value (NCL)
Illite	8	0.09	30
Kaolinite	13	0.37	37
Chlorite	14	0.32	52
Smectite	18-22	0.17	44

$$\phi_{N,dry-cl} = \frac{(30+37+52+44)/100}{4} = 0.4075 = 40.75\% \tag{15}$$

2.3.3 Critical Porosity

The critical-porosity model (Nur et al. 1991, 1998) introduces a certain porosity limit that separates the load-bearing sediments and the suspensions; this porosity limit is called the critical porosity (ϕ_c). Suppose a sedimentary rock's porosity is less than the critical porosity ($\phi < \phi_c$), then the rock is frame-supported. However, if the porosity is greater than the critical porosity ($\phi > \phi_c$), then the rock is fluid-supported. Figure 4 shows the physical illustration for the critical porosity.

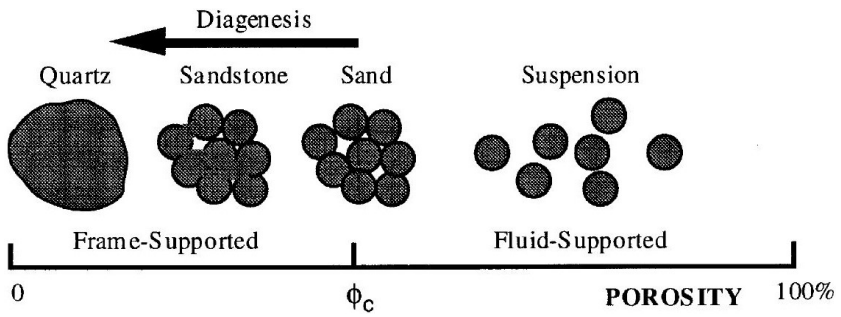

Figure 4: The physical meaning of the critical porosity for sand; differentiating frame-supported and fluid-supported conditions (Taken from Nur et al., 1998)

Figure 5 shows the load-bearing sediments and suspensions overlayed by the P-wave velocity (V_p) dataset from several references such as Yin (1992), Han (1986), and Hamilton (1956). The sediments with porosity less than 40% exist just above the Reuss bound, where sedimentary processes such as compaction and diagenesis occurred. On the other hand, the sediments with porosity of more than 40% exist exactly on the Reuss bound as a suspension. The sediments located in the 40% porosity value are typically the newly deposited clean sand. In this regard, the typical critical porosity for sedimentary rocks is 40%. Nur et al. (1998) summarize the critical porosity for various rocks as shown in Table 2.

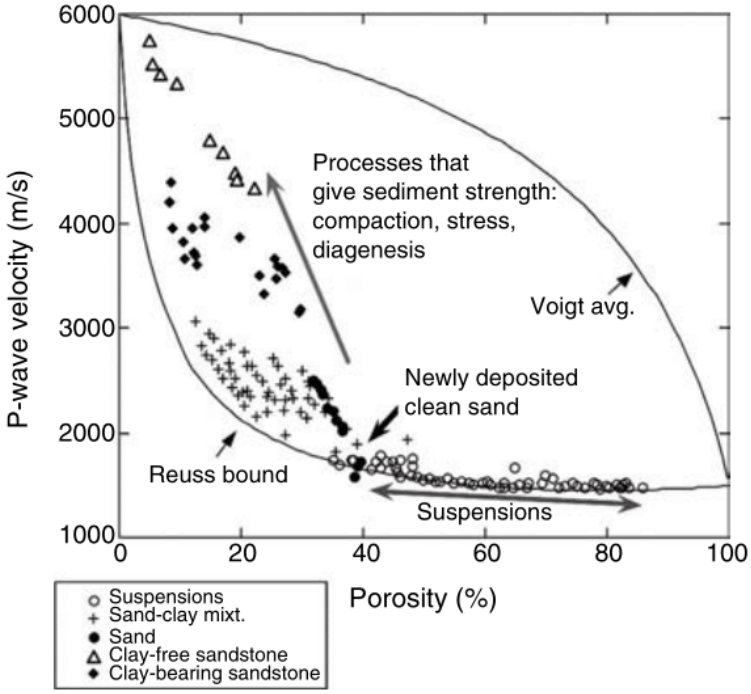

Figure 5: The P-wave velocity (V_p) dataset versus porosity of water-saturated sediments from Yin (1992), Han (1986), and Hamilton (1956), alongside with the separation of load-bearing sediments - suspension, between the Voigt - Reuss Bounds (Avseth et al., 2010).

Table 2: Several critical porosity values for various rocks or materials (Nur et al., 1998).

Material	**Critical Porosity** (ϕ_c)	**Material**	**Critical Porosity** (ϕ_c)
Sandstones	40%	Rock Salt	40%
Limestones	40%	Cracked Igneous Rocks	5%
Dolomites	40%	Oceanic Basalts	20%
Pumice	80%	Sintered Glass Beads	40%
Chalks	65%	Glass Foam	90%

Several references suggest the methodologies for estimating the critical porosity: by utilizing an extrapolation with the Hashin-Shtrikman Lower Bound (Smith and Brown, 2005); integrating the elastic-property measurements, quantitative mineralogic and petrographic analysis (Fournier and Borgomano, 2009); based on a regression model on percolation theory (Boadu, 2018); and based on the pore geometry and structure (Prakoso et al., 2018). Later in this thesis, the critical porosity estimation is based on the lithological consideration from the volume fraction percentage for sand, silt, and clay.

2.4 Poisson's Ratio and Stress Sensitivity

2.4.1 Poisson's Ratio

Poisson's ratio (ν) is a dimensionless parameter that describes the material's deformation in respect to the perpendicular direction to the applied force. It also describes the rock's strength, related to the closure stress (Poisson, 1829; Belyadi et al., 2019). Most materials have a range of ν between 0.1 to 0.45, where stiffer and softer materials have lower and higher values of ν, in that order. Mathematically, the Poisson's ratio is expressed by a negative ratio between transverse strain to axial strain when an isotropic material is subjected to uniaxial stress, as shown in Figure 6 and Equation 16.

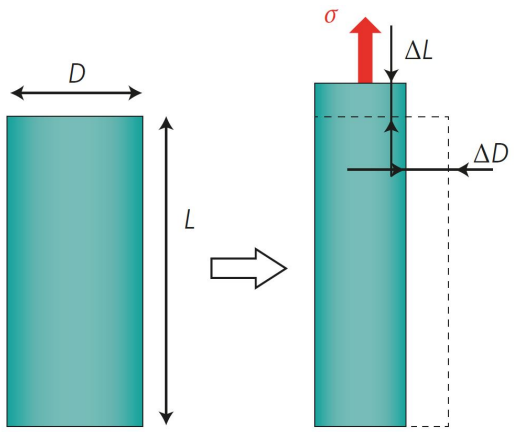

Figure 6: An illustration for a material that exposed into an axial tension or stretching (Taken from Greaves et al., 2011)

$$\nu = -\frac{\epsilon_y}{\epsilon_x} = -\frac{\Delta D/D}{\Delta L/L} \tag{16}$$

Where ϵ_y is the transverse strain and ϵ_x is the axial strain. The signs of these strains will be respectively negative and positive in the setting of axial tension or stretching. Conversely, it would be the other way for axial compression. As for sedimentary rock, the typical Poisson's ratio value is around 0.2 for sandstone and siltstone, 0.3 for carbonate, and more than 0.3 for shale and clay (Yale and Jamieson, 1994; Gercek, 2007). From this nature, then the Poisson's ratio can differentiate stiffer consolidated and softer unconsolidated sediments.

In practice, there are several ways to calculate Poisson's ratio. One of the ways is by using the sonic log in the depth of interest, in which the log provides both shear and compression wavelength travel time, as shown in Equations 17 and 18.

$$\nu = \frac{0.5R_v^2 - 1}{R_v^2 - 1} \tag{17}$$

Where R_v is:

$$R_v = \frac{\Delta t_s}{\Delta t_c} \tag{18}$$

Δt_s is the shear wave travel time, and Δt_c is the compression wave travel time. Both of these parameters are usually in the unit of $\mu s/ft$. It can be seen that these travel time parameters are reciprocal to the elastic waves' velocity as seen in Equation 19.

$$\frac{\Delta t_s}{\Delta t_c} = \frac{V_p}{V_s} \tag{19}$$

Hence, the Equation 17 could be rewritten as:

$$\nu = \frac{0.5\left(\frac{\Delta t_s}{\Delta t_c}\right)^2 - 1}{\left(\frac{\Delta t_s}{\Delta t_c}\right)^2 - 1} \cdot \frac{2}{2} = \frac{\left(\frac{\Delta t_s}{\Delta t_c}\right)^2 - 2}{2\left(\left(\frac{\Delta t_s}{\Delta t_c}\right)^2 - 1\right)}$$

$$\nu = \frac{1}{2}\frac{\left(\frac{V_p}{V_s}\right)^2 - 2}{\left(\frac{V_p}{V_s}\right)^2 - 1} \tag{20}$$

Furthermore, the elastic velocity could be expressed in terms of elastic moduli as seen in Equation 21.

$$\left(\frac{V_p}{V_s}\right)^2 = \frac{(K + 4/3G)/\rho}{G/\rho} = \frac{K + 4/3G}{G} \cdot \frac{3}{3} = \frac{3K + 4G}{3G} \tag{21}$$

then Equation 20 could also be rewritten as:

$$\nu = \frac{1}{2}\frac{\frac{3K+4G}{3G} - 2}{\frac{3K+4G}{3G} - 1} = \frac{1}{2}\frac{\frac{3K+4G}{3G} - \frac{6G}{3G}}{\frac{3K+4G}{3G} - \frac{3G}{3G}} = \frac{1}{2}\frac{\frac{3K-2G}{3G}}{\frac{3K+G}{3G}}$$

$$\nu = \frac{3K - 2G}{2(3K + G)} \tag{22}$$

From the three equations (Equations 17, 20, and 22), it could be said that the Poisson's ratio could be obtained either from the sonic log, elastic velocities, or elastic moduli.

2.4.2 Stress Sensitivity

Han (1986) conducts a study to see the compaction effect of sand-clay mixture, as seen in Figure 7. The figure shows that as the confining pressure (or lithostatic stress) increases, the decrements of porosity for pure sand (0% clay mixture) are more significant than for the 30% clay mixture. Similarly, the increments of compressional wave (P-wave) velocity for the pure sand are also more significant.

Dong et al. (2010) and MacBeth (2004) provide experimental results of stress dependence for porosity and elastic moduli. Figure 8 shows the comparison of the decrements for the porosity as the effective confining pressure (net stress or differential stress) increases for fine-grained sandstone and silty-shale samples. From this figure, it is seen that the decrements of the porosity for fine-grained sandstone are relatively more significant than for the silty-shale. Subfigures (a) and (b) of Figure 9 respectively show the stress dependence of bulk and shear moduli for three sandstone samples. The samples consist of well-cemented sandstones, unconsolidated sands, and manually disaggregated and then reassembled sand pack. MacBeth states that the porosity stress dependence is related to the overall rock-frame compressibility, where the unconsolidated higher-porosity sandstone is more sensitive to stress.

The Poisson's ratio is a function of elastic velocities related to porosity, bulk modulus, and shear modulus. Therefore, it is reasonable to set the Poisson's ratio as the primary mechanism to predict the stress sensitivity and differentiate consolidation states (consolidated and unconsolidated sediments).

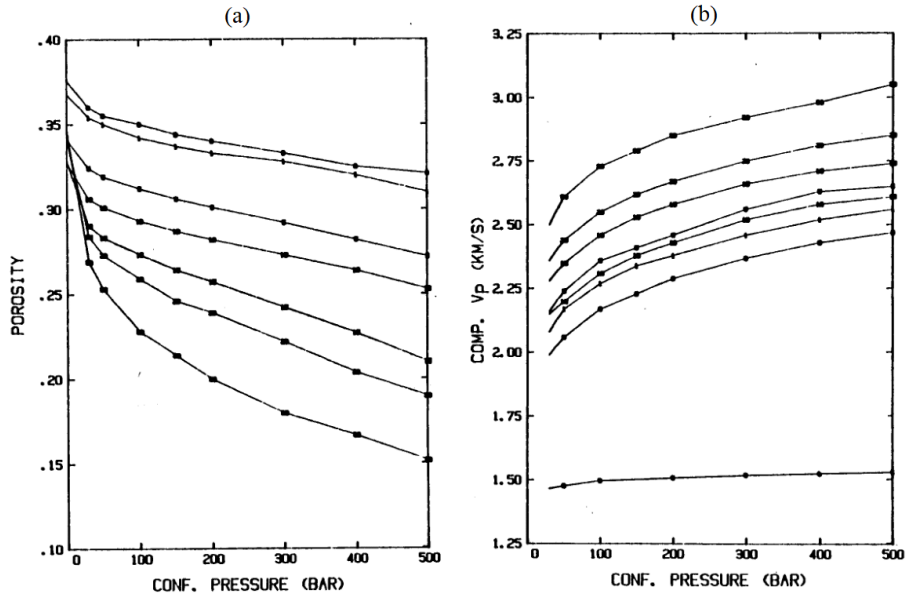

Figure 7: (a) The porosity versus confining pressure for sand-clay mixture with various clay content values. From top to bottom: 30%, 20%, 15%, 10%, 5%, 1%, 0%. (b) The compressional wave velocity (V_p) versus confining pressure for sand-clay mixture with various clay content values. From top to bottom: 0%, 1%, 5%, 10%, 15%, 20%, 30%, and pure clay of smectite.
(Modified from Han, 1986)

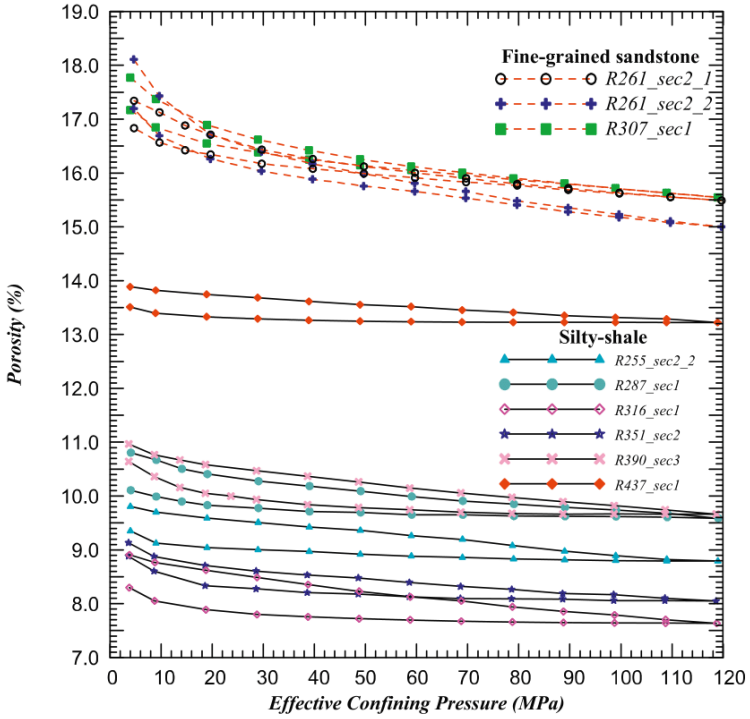

Figure 8: Stress dependence of porosity for fine-grained sandstone and silty-shale samples from Taiwan Chelungpu fault Drilling Project or TCDP.
(Modified from Dong et al., 2010)

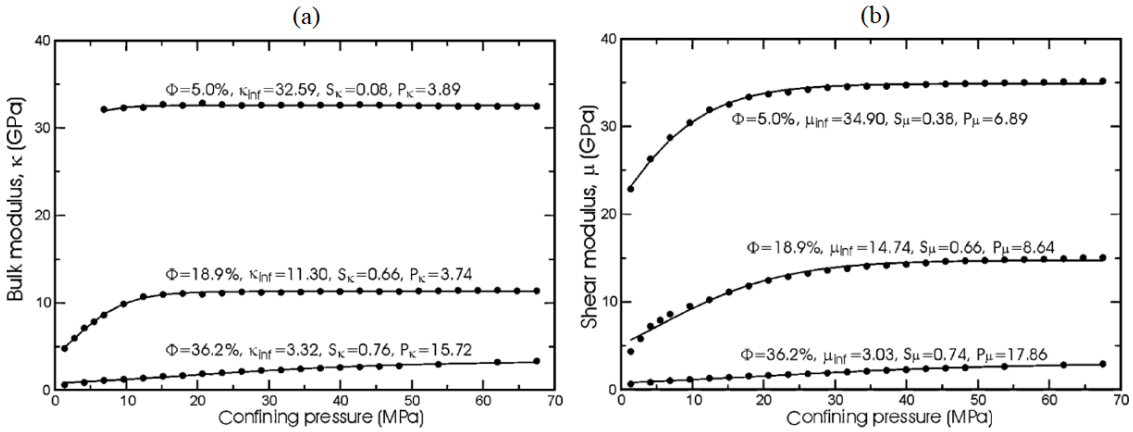

Figure 9: Stress dependence of (a) bulk modulus and (b) shear modulus. The samples represent three different conditions: well-cemented (5.0% porosity), unconsolidated (18.9% porosity), and manually disaggregated sand pack (36.2% porosity).
(Modified from MacBeth, 2004)

2.5 Horizontal-to-vertical Net Stress Ratio

The hydrostatic pressure is a condition when the pore pressure and the atmospheric pressure at the surface reach equilibrium, in which the two are interconnected through a pore network (Moss et al., 2003). In a formation pore pressure, exist an upper limit where the fractures are created, or the pre-existing fractures re-opened. The fracture pressure gradient is typically below the lithostatic pressure gradient related to the regional stress field. According to Hubbert and Willis (1957) and Eaton (1969), three variables that controlled the fracture pressure gradients are: (1) the lithostatic or overburden gradient, (2) hydrostatic or pore pressure gradient, and (3) the horizontal matrix stress to vertical stress ratio. The third parameter is considered equal to $\nu/(1-\nu)$, where ν is the Poisson's ratio. Equation 23 shows the fracture pressure gradients.

$$\frac{F}{D} = \frac{\nu}{1-\nu}\left(\frac{S}{D} - \frac{p}{D}\right) + \frac{p}{D} \tag{23}$$

Where F/D is the fracture pressure gradient, p/D is the pore pressure gradient, and S/D is the overburden pressure gradient. Figure 10 shows the leak-off pressure (LOP) data from the central North Sea, where this LOP data could be used to determine the fracture gradient. From this figure, the fracture gradient could be considered as the minimum horizontal stress. In practice, this information is helpful for drillers to assess the formation's strength around the casing shoe.

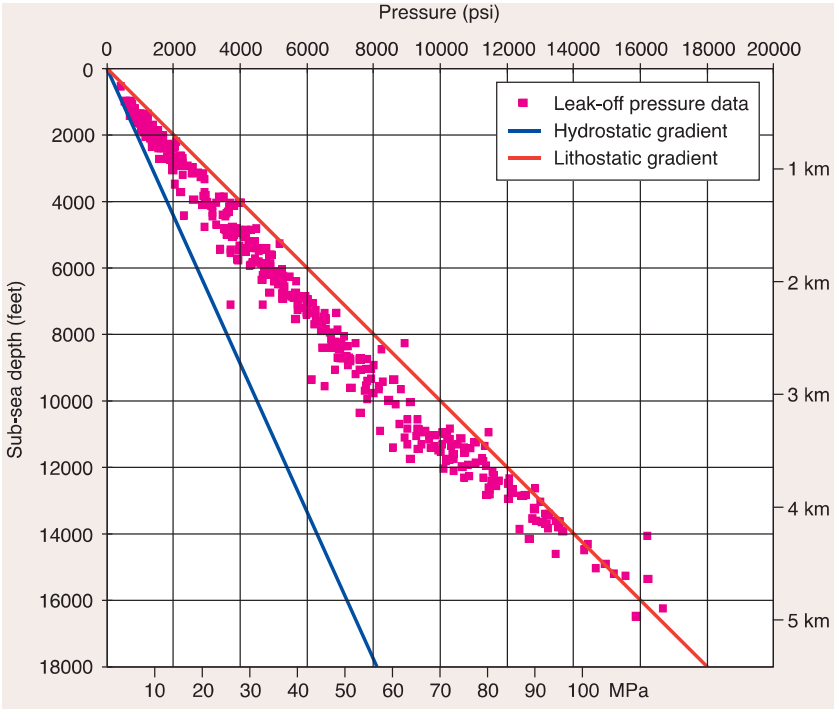

Figure 10: The fracture gradient or leak-off pressure data from the central North Sea. (Taken from Moss et al., 2003)

Figure 10 shows that the fracture gradient is slightly less than the lithostatic gradient, so that the minimum stress (horizontal stress) constitutes about 85% of the vertical stress, then increases to 95% for the depth more than 4 km (Grauls, 1997). This ratio of horizontal-to-vertical stress (or net stress) is considered inside the proposed methodology as the parameter of K'_o. This parameter affects the Bounding Average Method's weight parameter (W), particularly for the C_{44} (vertically-propagating S-wave modulus) prediction.

3 Database

This thesis's three wells are taken from the Norwegian Continental Shelf (NCS) area, namely Well 34/7-1, 6704/12-1, and Well 7220/8-1. Each of these wells has a list of several recorded data or logs, which could be seen in Table 3. The three wells' relevant information is available on the Norwegian Petroleum Directorate (NPD) fact pages in their respective final or completion reports, available for the public. However, some additional external references will also be considered.

Table 3: Several available log data for the three wells.

Log	**Well 34/7-1**	**Well 6704/12-1**	**Well 7220/8-1**
Depth	✓	✓	✓
Density Correction	✓	✓	✓
Bulk Density	✓	✓	✓
Neutron Density	✓	✓	✓
Compressional Sonic Log	✓	✓	✓
Shear Sonic Log		✓	✓
Gamma Ray (GR)	✓	✓	✓
Spectral GR - K		✓	✓
Spectral GR - Th		✓	✓
Spectral GR - U		✓	✓
Photoelectric Factor (PEF)		✓	✓
Shallow/Micro Resistivity	✓	✓	✓
Medium Resistivity	✓	✓	✓
Deep Resistivity	✓	✓	✓
Spontaneous Potential (SP)		✓	
Caliper	✓	✓	✓
Bit Size		✓	✓
Rate of penetration (ROP)		✓	✓

3.1 Well 34/7-1

Well 34/7-1 was an exploration well located in the Snorre field, North Sea, Norway (Figure 11), particularly in block number 34 of the North Viking Graben (Figure 12). This well's primary purpose was to test the Triassic Upper Lunde section's reservoir quality and fluid distribution, based on the nearby hydrocarbon-bearing well, 34/4-4. Well 34/7-1 encountered hydrocarbons in the Triassic sandstones from 2392 m RKB (top reservoir) and 2586 m RKB (oil-water contact). The average porosity and water saturation of the reservoir are respectively 23.2% and 36%.

Figure 13 shows the North Sea pressure profile, where it is seen that the pore pressure of the Norwegian North Viking Graben is higher than the hydrostatic stress; this is a clear indication of an overpressure condition.

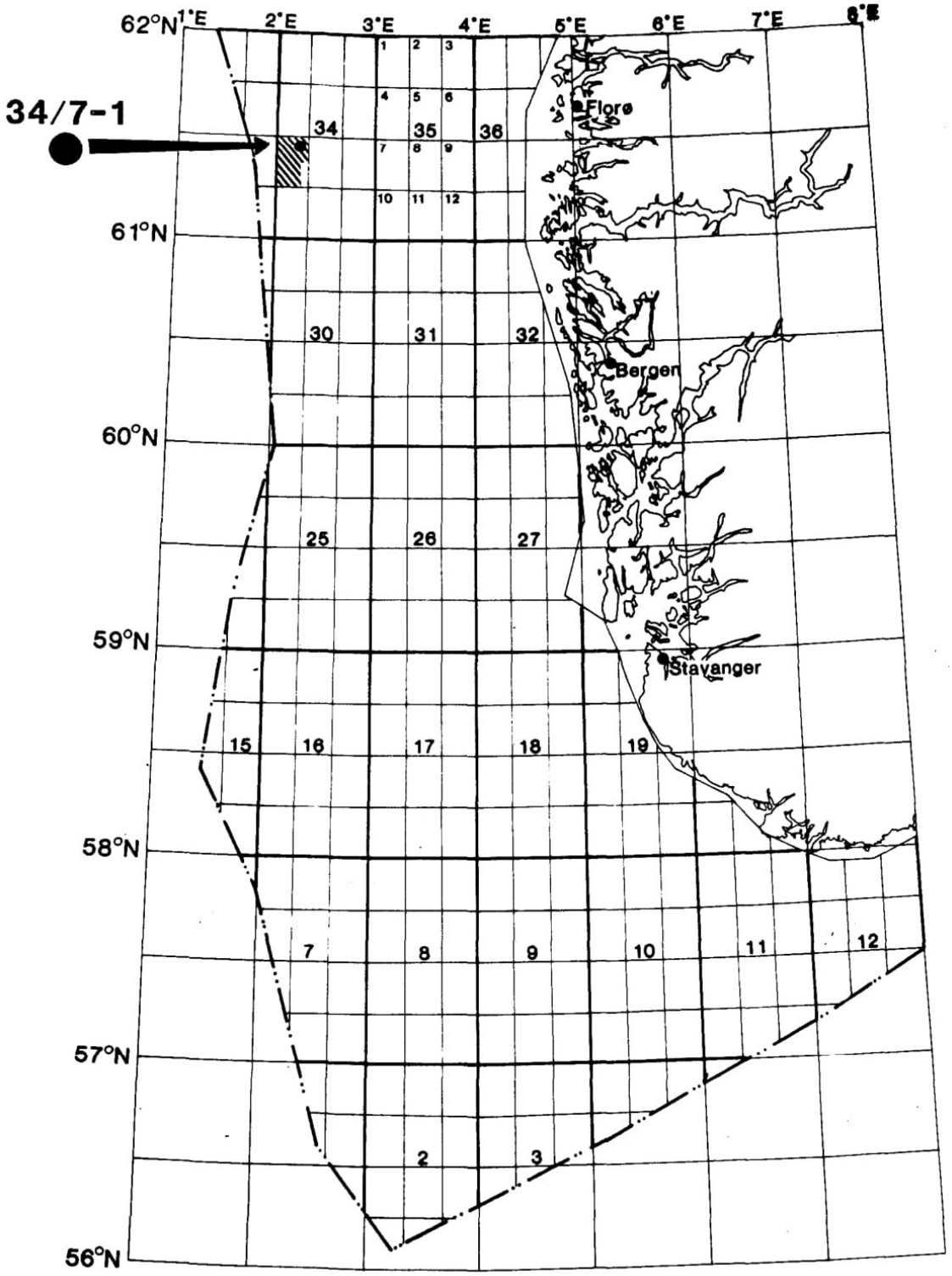

Figure 11: The location for Well 34/7-1.
(Taken from Saga Petroleum, 1985)

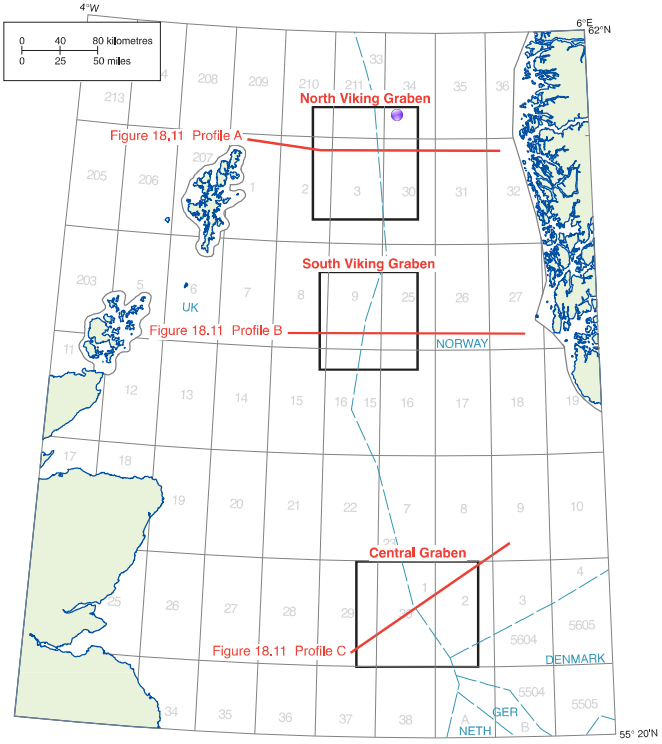

Figure 12: Several area of interest in the North Sea. Well 34/7-1 is located in the block number 34, marked by a purple dot. (Modified from Moss et al., 2003)

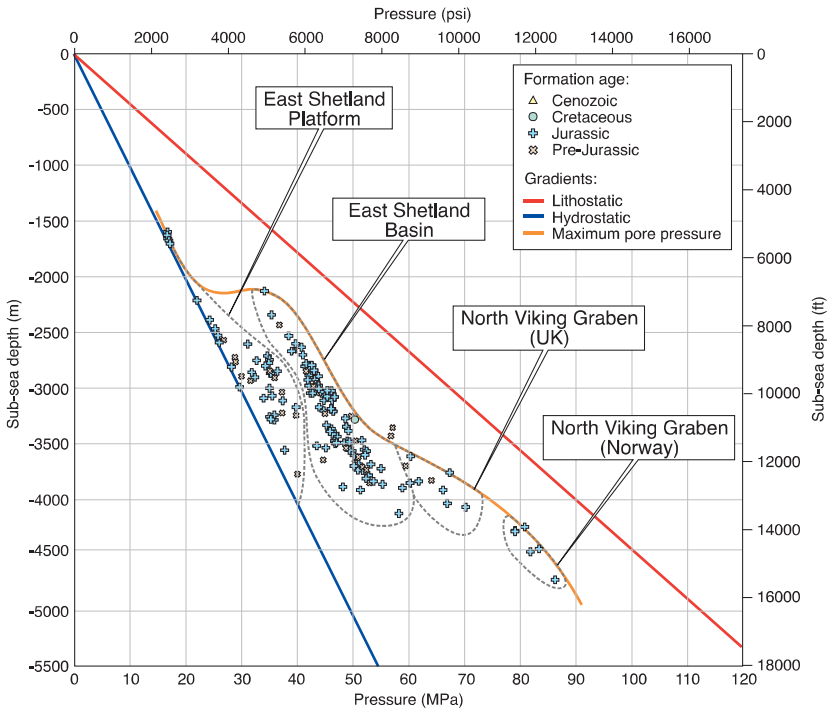

Figure 13: The pressure profile for Profile A, as seen in Figure 12. The Well 34/7-1 is located in the Northern Viking Graben of the Norwegian Territory. (Modified from Moss et al., 2003)

Align with Figure 13; the completion report suggests a pressure gradient build-up between 1350 m RKB and 1400 m RKB. The pressure gradient increases throughout the Hordaland Group and Rogaland Group, reaching a pressure/depth ratio of 1.40 g/cc at 1823 m RKB. Several tight spots between the interval of 1850 to 2150 m RKB were observed, and the pressure gradient is slightly above the value of the mud weight (1.47 g/cc). The Repeat Formation Test (RFT) measurement in the top reservoir gives a formation pressure/depth ratio of 1.62 g/cc, as this is the maximum value for this ratio in the well. The ratio then decreases until it reaches 1.48 g/cc in the total depth (TD). The formation pressure profile could be seen in **Appendix A**. The conventional core analysis data also available on the completion report, where values of the oil saturation (S_o) are given in several depth intervals (from 2398 to 2622 m RKB), as seen in **Appendix B**. The rest of depths outside this intervals are considered to be water-saturated ($S_o = 0$ and $S_w = 1$). Several temperature measurements on the well are also available from the report, as seen in **Appendix C**. Table 4 shows the lithological descriptions for Well 37/4-1.

Table 4: The lithological descriptions for each of Groups or Formations for Well 34/7-1. (Provided by Saga Petroleum, 1985)

Depth [m RKB]	Group	Formation	Lithological Descriptions
353	Nordland Gp.	Seabed	Claystone and Basal sand (1028-1052 m RKB)
1150		Utsira Fm.	Sandstone alternating with claystone. Very glauconitic sand (1152-1166 m RKB).
1170	Hordaland Gp.		Sandstone (8 meter) on top, mainly claystone. Unconformity of claystone (1360 m RKB).
1673	Rogaland Gp.	Balder Fm.	Tuffaceous claystone/siltstone
1696		Lista Fm.	Claystone, occasionally silty
1823	Shetland Gp.	Jorsalfare Fm.	Claystone, occasionally slightly silty
1933		Kyrre Fm.	Mudstone with occasional limestone
2387	Cromer Knoll Gp.	Mime Fm.	Claystone/Marl and limestone
2392	Hegre Gp.	Lunde Fm.	Middle member: Silty sandstone alternating with claystone and minor marl Upper member: Sandstone alternating with and interbedded with siltstones and claystone. Traces of marl and limestone

3.2 Well 6704/12-1

Well 6704/12-1 was an exploration well located in the Gjallar Ridge, Vøring Basin, Norwegian Sea, Norway (Figure 14). Since the seafloor of this well is quite deep (1352 m), well 6704/12-1 is called a deepwater well. The primary purpose of this well was to test the Upper Cretaceous section's petroleum potential below the top Cretaceous unconformity in the eastern part of the C-structure. The best reservoir was found in the uppermost part of the Springar Formation, with an average porosity of 26% and average permeability of 556 mD. However, no hydrocarbon log responses were observed in all depth intervals; hence, the well is considered as a dry well.

Aubert et al. (1999) provide several relevant information regarding this well: (1) the temperature of the water at the seafloor is $-2.4°C$, with the formation's temperature gradient of $5.3°C/100\ m$. (2) The pressure knowledge was limited. Several nearest wells could be the reference for comparison, namely Well 6707/10-1 and 6707/11-1. However, they suggest that this well has effective stress equal to or close to the hydrostatic pressure. (3) Since this well is a dry well, it is reasonable to set the hydrocarbon saturation

as 0 and water saturation as 1 for all depth intervals ($S_{HC} = 0$ and $S_w = 1$). The final report of this well provides the formation pressure and temperature values, which could be seen in **Appendix D**. Table 5 shows the lithological descriptions for Well 6704/12-1.

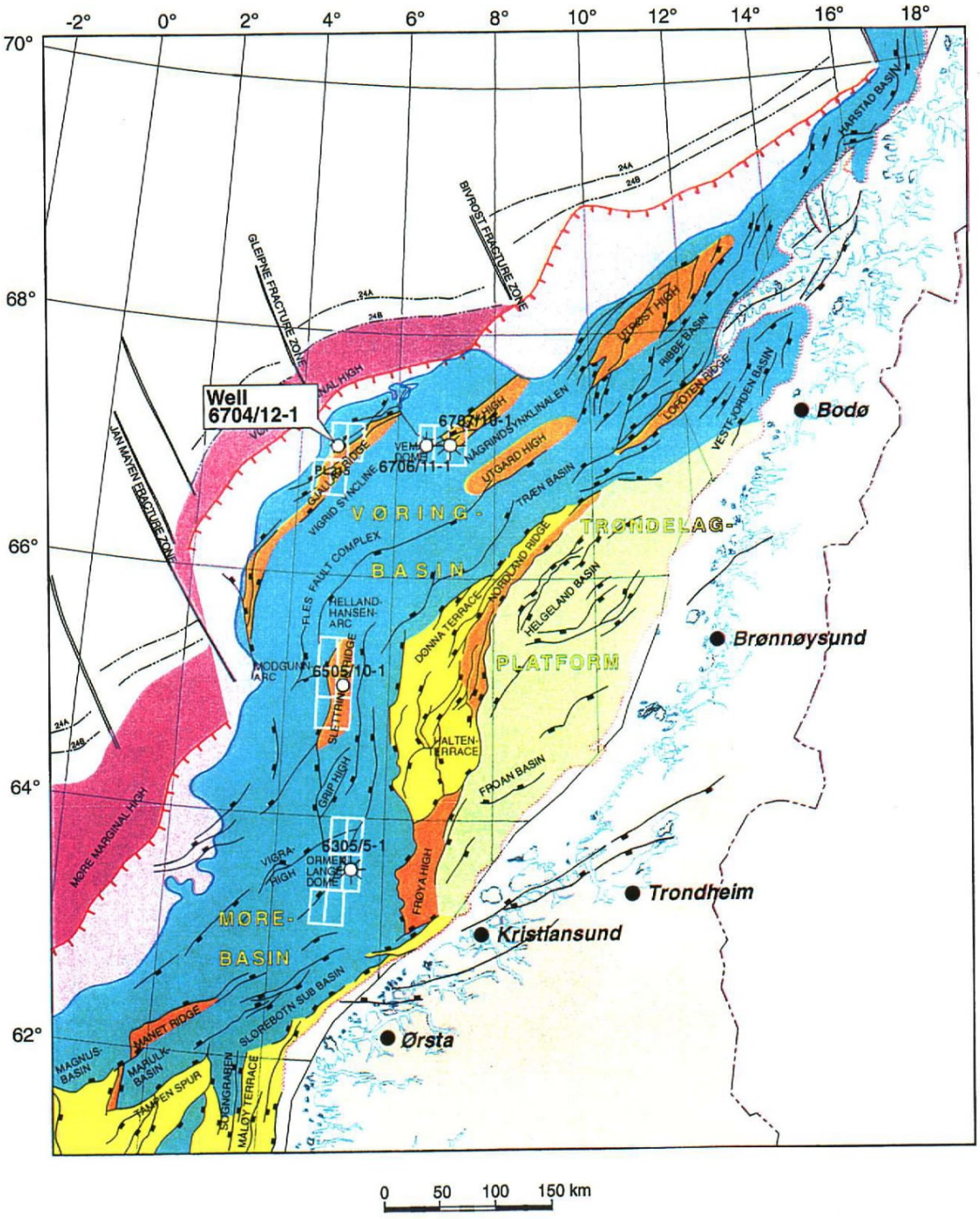

Figure 14: The location for Well 6704/12-1.
(Taken from Aubert et al., 1999)

Table 5: The lithological descriptions for each of Groups or Formations for Well 6704/12-1. (Provided by Aubert et al., 1999)

Depth [m RKB]	Groups	Formations	Lithological Descriptions
1377	Nordland Gp.	Naust Fm	Soft to very soft clay
1459		Kai Fm.	Silica ooze with minor clay content
1920	Hordaland Gp.	Brygge Fm.	Upper Brygge: Silica ooze with increasing clay Middle Brygge: Clay / Claystone with minor sand and limestone Lower Brygge: Clay / Claystone, minor sandstone, and limestone stringer
2548	Rogaland Gp.	Tang Fm.	Silty sandstone, minor claystone and trace of limestone and dolomite
2558	Shetland Gp.	Springar Fm.	Massive sandstone and clay with minor limestone
3244		Nise Fm.	Claystone with interbedded massive sandstone. Two thin basalt intrusions (3495 m RKB and 3512 m RKB)

According to Awadalkarim et al. (2013), the diatomaceous or siliceous ooze sediments are commonly present in the seafloor of the Norwegian Sea. These occurrences of ooze sediments are confirmed within the final well report of this well (Aubert et al., 1999). It is also important to notice that the ooze within the well is non-calcareous. Based on this *a priori* information, then we need to consider the ooze sediments in the shallower part of the well when we model the solid compartment of the rock. Breitzke (2000) provides the typical value of P-wave velocity (V_p), bulk modulus (K_{oz}), and shear modulus (G_{oz}) for diatomaceous or siliceous ooze, as seen in Figure 15. From subfigure (a), it is seen that the typical V_p for these sediments are in the range of 1500 m/s or 1.5 km/s. The typical K_{oz} for the same sediments is around 2700 MPa or 2.7 GPa, while the typical G_{oz} is between 6 to 16 MPa. Since we know that the ooze sediments are non-calcareous, then the G_{oz} value of the siliceous ooze must be higher, between 12 to 16 MPa; then we took the average between these two so that the G_{oz} is decided to be 14 MPa or 0.014 GPa. Aubert et al. (1999) mention that the Ooze sediments are found in the Kai and Upper Brygge Formations only. However, the depth interval of these two are relatively longer than the rest of the formations in the shallower part of the well (Naust, Upper Brygge, and Lower Brygge Formations), so we assume that the ooze sediments are the most dominant lithology in this particular part of the well.

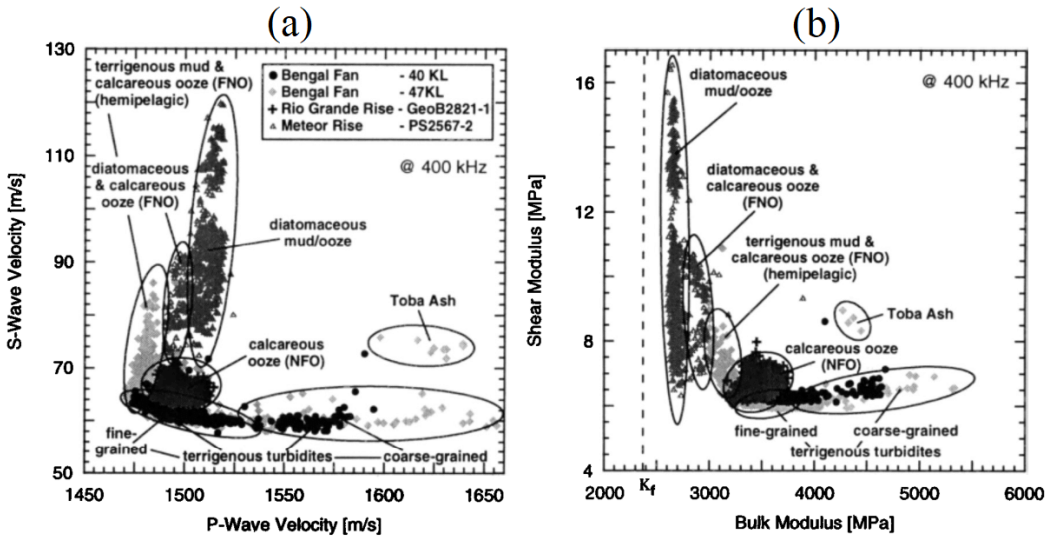

Figure 15: (a) The typical velocity for Ooze sediments; (b) the typical bulk and shear modulus for Ooze sediments. (Modified from Breitzke, 2000)

3.3 Well 7220/8-1

Well 7220/8-1 was an exploration well located west of the Polheim Sub-platform and Loppa High, Johan Castberg field, the Barents Sea, Norway (Figure 16). The primary purpose of this well was to assess the economic volume of the hydrocarbon and establish the hydrocarbon contact in the Skrugards Prospect (Stø and Nordmela formations). Both oil and gas were discovered in this well, with a thick gas column of 37 meters (Gas-oil-contact at 1312 meters) and a thick oil column of 83 meters (Oil-water-contact at 1395 meters).

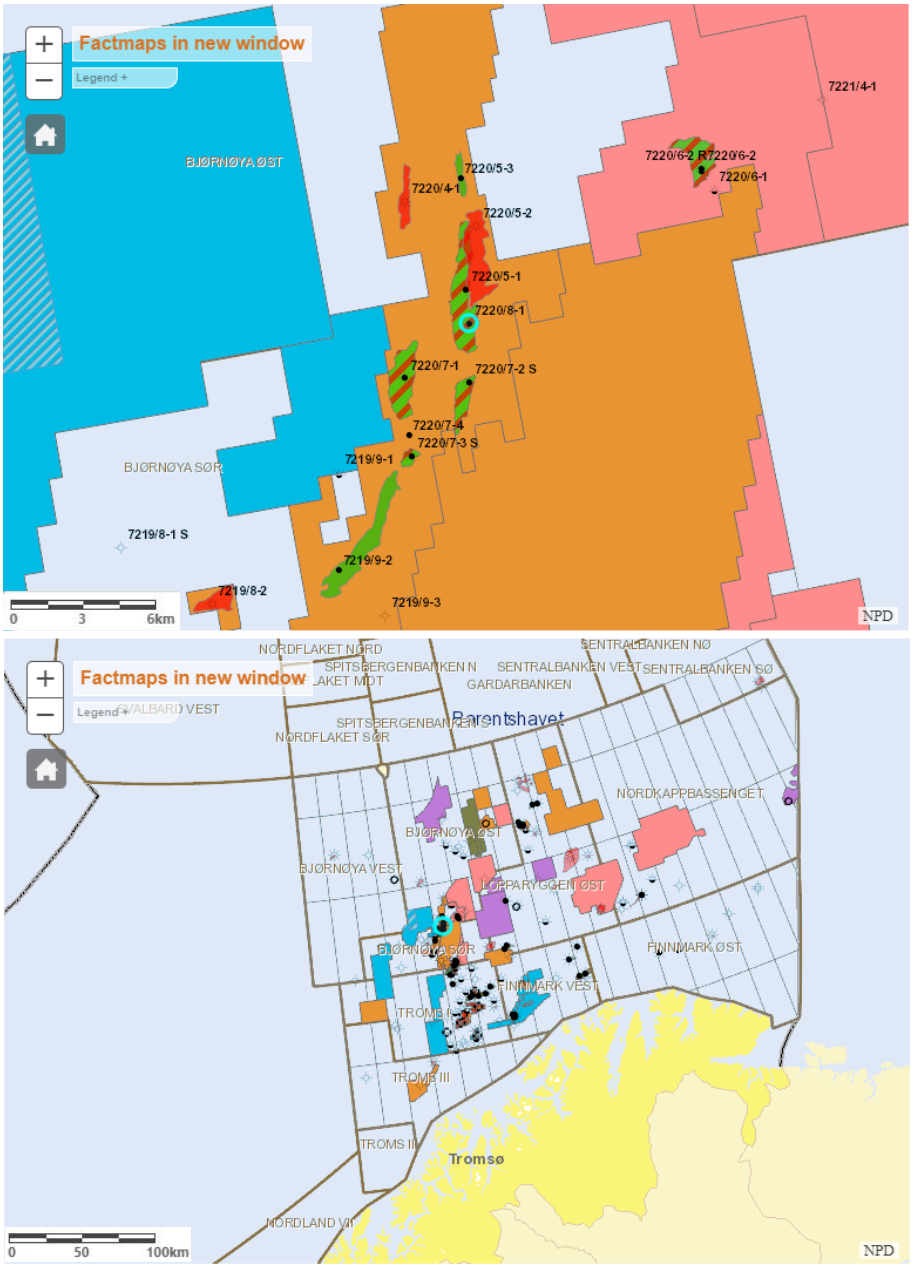

Figure 16: The location for Well 7220/8-1.
(Taken from NPD's factpage)

The full final report of this well is currently unavailable for the public since the abandonment of the well is not as old as the two previous wells. The stress profile of the well is available and could be seen in **Appendix E**. The temperature data of the well is available on the Modular formation Dynamics Tester (MDT) fluid samples, as seen in **Appendix F**. Since both oil and gas were present in this well, it is crucial to have information regarding the hydrocarbon's saturation. However, the saturation data is not available on the report nor the fact page. Hansen (2019) provides several saturation values from the Alta Discovery in the Barents Sea, as shown in Table 6. Since the average porosity and clay volume of the reservoir on well 7220/8-1 is respectively 25% and 5%, then it is quite similar to the values for Well 7220/11-3; hence, it is reasonable to assume that the saturation values for the two wells are the same. Table 7 shows the lithological descriptions for Well 7220/8-1.

Table 6: The saturation values of the Alta Discovery. ϕ_{avg} and $_{cl,avg}$ is respectively the average porosity and clay content of the reservoir. (Hansen, 2019)

Well Name	**Water Saturation** (S_w)	**Hydrocarbon Saturation** (S_{hc})
7220/11-1	34%	66%
$\phi_{avg} = 12\%$ and $V_{cl,avg} = 12\%$		
7220/11-3	19%	81%
$\phi_{avg} = 20\%$ and $V_{cl,avg} = 2\%$		
7220/11-2	11%	89%
$\phi_{avg} = 14\%$		

Table 7: The lithological descriptions for each of Groups or Formations for Well 7220/8-1. (Provided from NPD)

Depths [m RKB]	**Groups**	**Formations**	**Lithological Descriptions**
397	Nordland Gp	Seabed	[No detail information was available]
455	Sotbakken Gp.	Torsk Fm.	Non-calcareous claystones. Rarely with siltstone/limestone stringers
1014	Advendalen Gp.	Kolmule Fm.	Claystone and shale, silty in parts with minor thin siltstone interbeds and limestone and dolomite stringers
1227		Kolje Fm.	Shale and claystone dominate, with minor interbeds of pale limestone and dolomite.
1245		Knurr Fm.	Claystone with thin limestone and dolomite interbeds
1252		Fuglen Fm.	Pyritic mudstones with interbedded thin limestones
1276	Kapp Toscana Gp.	Stø Fm.	Mature sandstones
1354		Nordmela Fm.	Interbedded siltstones, sandstones, shales and claystones with minor coals.
1511		Tubåen Fm.	Sandstones with subordinate shales and minor coals
1628		Fruholmen Fm.	Shales pass gradually upwards into interbedded sandstones, shales and coals
2122		Snadd Fm.	Basal shales coarsen up into shales with interbeds of siltstones and sandstones

4 Methods

The proposed methodology for elastic velocity prediction consists of 5 major steps, as shown in Figure 17. The first step is called Set preset data, where the main idea is to provide the initial input data for further steps until the whole process is finished. Pre-conditioning is the second step where it acts as the quality control of the inputted data so that the values will be reasonable and supposedly error-free. The methodology proceeds to estimate several petrophysical parameters, such as the porosity values and lithological volume fractions. This particular step is called the Petrophysical Analysis. The normalization of these volume fractions for both implicit and explicit bound water models is performed in this step. The rock physics analysis and velocity prediction are the essential steps in the proposed methodology. The velocity prediction is performed based on the Voigt-Reuss bounding method and the Bounding Average Method. The last step is called Fitness Observation, where it provides the fitness of the velocity prediction by calculating both correlation coefficient and error percentage.

More complete and detailed substeps for the five mentioned major steps are provided in the following subchapters.

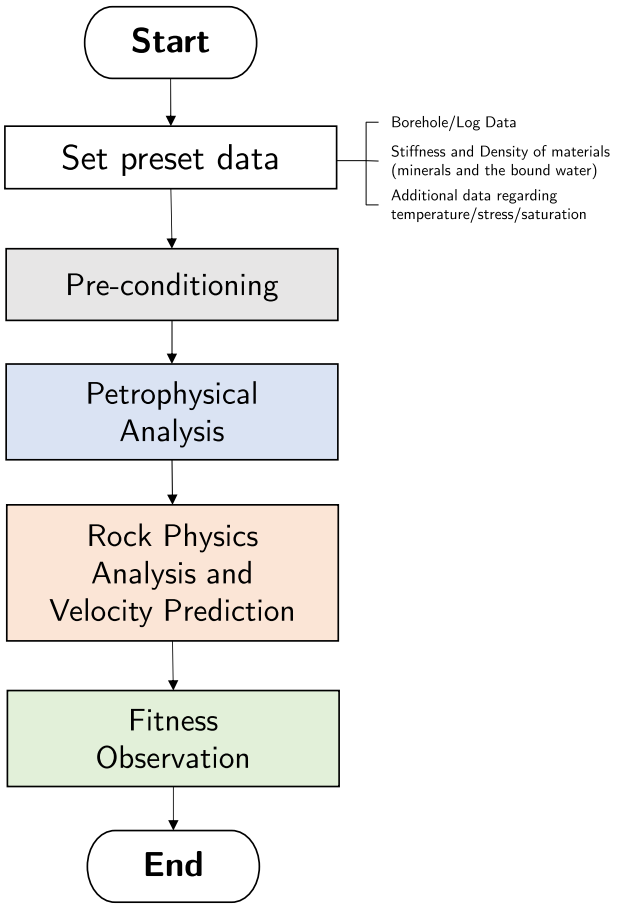

Figure 17: General flowchart of the proposed methodology for velocity prediction.

4.1 Set preset data

We need to provide several relevant initial input data for this velocity prediction process in this first step. The three input data are: (1) the borehole/well log data; (2) stiffness parameters and densities of the materials, such as the minerals and bound water; (3) some *a priori* data regarding the temperature, stress, or saturation. The borehole data are usually in the form of *.las files, where several available recorded data or logs are provided inside the files. Table 3 in the previous chapter shows the available logs of the three wells used in this thesis. Several essential logs for the proposed methodology are the bulk-density, gamma-ray, and neutron porosity.

We defined the minerals' stiffness parameters and density only for clay and sand (quartz) due to the reason that we limit our model prediction for the two most abundant sedimentary rocks in nature (Berg, 1986; McDonald and Schmidt, 1991; Tucker, 2003), where naturally the two are most likely discovered as a mixture. We assume that the sand only consists of quartz minerals; however, it might also contain other minerals such as feldspar, mica, et cetera. The reason for choosing this assumption is that the grain frameworks of sands typically consist of quartz (Folk, 1965).

The model prediction might miss other major lithologies (such as limestones, chalk, igneous rocks, metamorphic rocks, et cetera), so that the model could potentially be problematic. This problem could be rectified by including the other related mineralogical or lithological parameters into the solid compartment of the proposed methodology. Special treatment is performed for the shallower part of Well 6704/12-1 due to the siliceous ooze sediments presence; hence, the elastic moduli for these sediments also need to be considered.

As for the bound water, we define the stiffness parameters based on several values provided by Kolstø (2012). He provides the values based on three fluid systems with different salinity values: 3.8%, 5.0%, and 7.4%. According to Castro and Huber (2003), the typical salinity of seawater is 35 parts per thousand or 3.5 sodium weight per cent. Even though the exact salinity values of the bound water for the three wells are not available, we assume that the bound water has similar salinity as the seawater. As a result, we chose the bulk and shear moduli for bound water with a fluid system of 3.8% sodium weight. Table 8 shows the values for the stiffness and density of the materials in this proposed methodology.

Table 8: The stiffness and density for the minerals (Mavko et al., 2009; Breitzke, 2000) and bound water with a salinity of 3.8% sodium weight (Kolstø, 2012).

Clay and Quartz (Mavko et al., 2009); Siliceous Ooze Sediments (Breitzke, 2000).						**Bound Water (Kolstø, 2012)**	
$C_{33,cl}$	30 GPa	K_{qz}	37 GPa	K_{oz}	2.7 GPa	K_{bw}	4.3 GPa
$C_{44,cl}$	10 GPa	G_{qz}	44 GPa	G_{oz}	0.014 GPa	G_{bw}	0.5 GPa
ρ_{cl}	2.7 g/cc	ρ_{qz}	2.65 g/cc	ρ_{oz}	1.208 g/cc	ρ_{bw}	1.03 g/cc

The density of ooze sediments are estimated from the typical value of the V_p for these sediments (1.5 km/s) and using the given bulk modulus (K_{oz}) and shear modulus (G_{oz}) from Breitzke (2000). As shown in equation 24.

$$\rho_{oz}\ [g/cc] = \frac{K_{oz}[GPa] + \frac{4}{3}G_{oz}[GPa]}{(V_{p,oz}[km/s])^2} \tag{24}$$

For comparison, Table 9 shows the density and stiffness parameters for other minerals that potentially present either in the sand or clay but not yet included within the solid compartment of the proposed methodology. It is assumed that the isotropic P-wave modulus (M) is equivalent to the vertically-propagating anisotropic P-wave modulus (C_{33}).

Table 9: The density and stiffness parameters for other minerals that are potentially discovered within the sand or clay, but not yet implemented to the solid compartment of the proposed methodology. Compiled from Vyzhva et al. (2014) and Mavko et al. (2009).

Clay Minerals (Vyzhva et al., 2014)				**Silicates/Micas (Mavko et al., 2009)**				
Minerals	C_{33} **[GPa]**	C_{44} **[GPa]**	ρ	**Minerals**	K **[GPa]**	G **[GPa]**	M **[GPa]**	ρ
Kaolinite	32.1 - 52.6	12.1 - 16.7	2.52	Plagioclase feldspar	75.6	25.6	109.73	2.63
Montmorilonite/ Smectite	126.7	21.3	2.55	"Average" feldspar	37.5	15	57.5	2.62
Illite	55.0 - 87.4	11.7 - 14.1	2.79	Mica (Muscovite)	42.9	22.2	72.5	2.79
Chlorite	90 - 106.8	11.4 - 15.4	2.69	Mica (Biotite)	41.1	12.4	57.63	3.05

The additional data (regarding the temperature, stress, or saturation) are essential for some specific reasons for each of the wells. For example, since the Well 34/7-1 is an oil well, it is crucial to specify the oil saturation values inside the reservoir. For the same well, it is also given that overpressure occurs, so it is logical to use the given stress gradient for estimating the stress or pressure profile. All of this additional data are obtained from the final well reports on the Norwegian Petroleum Directorate (NPD) fact pages or some additional references outside the final well reports themselves.

4.2 Pre-conditioning

The second step is to ensure that the preset data is prepared well before goes to further analysis. This step is called the pre-conditioning, and some substeps are shown in Figure 18.

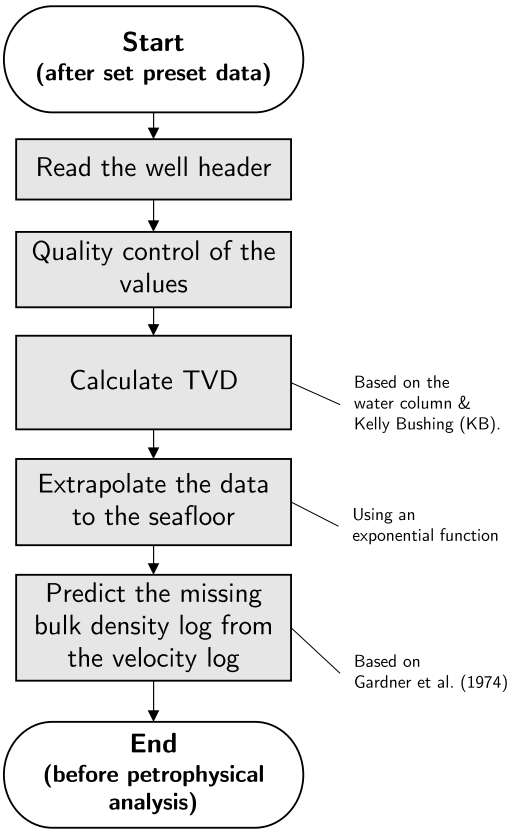

Figure 18: Flowchart for the substeps in the pre-conditioning step.

4.2.1 Read the Well Header

The first substep is to read the well header so that all of the available and relevant logs are included for the whole methodology steps. Several relevant logs are depth, bulk density, neutron density, sonic (both compressional and shear), gamma ray, caliper, and bit size. Since the sonic log is reciprocal to the slowness, then the P-wave and S-wave velocity (V_p and V_p) logs are obtained from the sonic logs by using the following equations:

$$V_p\ [km/s] = V_{p,Meas} = \frac{304800}{\Delta t_{comp}\ [\mu s/ft]} \tag{25}$$

$$V_s\ [km/s] = V_{s,Meas} = \frac{304800}{\Delta t_{shear}\ [\mu s/ft]} \tag{26}$$

Where Δt_{comp} is the compressional sonic transit time while Δt_{shear} is the shear sonic transit time. In contrast to the compressional log that almost always available, the shear sonic log might be absent from several wells; then, the V_s log cannot be obtained. In this study, Well 34/7-1 does not provide any shear sonic log, while Well 6704/12-1 has several depth intervals that do not have any shear sonic log measurement. To overcome this condition, then the V_s could be predicted based on the obtained V_p. A further explanation for this procedure could be seen later on in one of the substeps in the Rock Physics Analysis and Velocity Prediction steps.

4.2.2 Quality Control of The Values

Afterward, it is essential to perform quality control (QC) of the well so that the values of the data are correct and reasonable. In most of the well data, a value of "999" or something similar usually means that the log instruments do not record any data from that specific depth; hence, we should exclude this value from that specific depth.

The QC for elastic velocities are based on the understanding that they should not exceed the values for quartz aggregate (6050 m/s for V_p and 4090 m/s for V_s, according to Mavko et al., 2009) but not less than the most minimum possible values for water (1402 m/s for V_p, according to Chen and Millero, 1977; 0 m/s since V_s are not able to cannot propagate through liquids or gasses, according to Bent, 2013). As for the bulk density, it is designed not to exceed the highest possible value for sedimentary rocks (dolomites) and not less than for the water (respectively 2.88 g/cc and 1 g/cc, according to Mavko et al., 2009). Schön (2015) and Schlumberger (2009) provide several mean API values for gamma activity for various minerals. The minimum mean API values are 0 for clean quartz, calcite, and dolomite; the maximum value goes to one of the clay minerals (illites) with a value of 300. The QC for gamma-ray follows these values accordingly. Rider (1999) provides several neutron porosity values for various minerals. The minimum possible value is for quartz with a value of -2 neutron porosity units or -0.02 in fraction, and obviously, the maximum possible value for a porosity fraction is 100% or 1. The QC for neutron porosity follows these values as well.

Several quality control adjustments could be seen in Table 10. The quality control of S-wave velocity values for Well 34/7-1 is not performed since the well does not have a measured V_s log.

Table 10: Several procedures for quality control (QC) for each of the logs for each of the wells. The values outside the given interval are excluded by changing them into NaN (Not a Number) values.

Log	Well 34/7-1	Well 6704/12-1	Well 7220/8-1
P-wave Velocity or V_p [m/s]	$1402 < V_p < 6050$	$1402 < V_p < 6050$	$1402 < V_p < 6050$
S-wave Velocity or V_s [m/s]	-	$0 < V_s < 4090$	$0 < V_s < 4090$
Bulk Density or ρ_b [g/cc]	$1.0 < \rho_b < 2.88$	$1.0 < \rho_b < 2.88$	$1.0 < \rho_b < 2.88$
Gamma Ray or GR [gAPI]	$0 < GR < 300$	$0 < GR < 300$	$0 < GR < 300$
Neutron Porosity [frac]	$-0.02 < \phi_N < 1$	$-0.02 < \phi_N < 1$	$-0.02 < \phi_N < 1$

4.2.3 True Vertical Depth (TVD) Calculation

The next substep is to make some corrections to the given Depth log, where the goal is to convert the measured depth (MD) from the log to be the True Vertical Depth (TVD). In order to do so, then it is important to know the information of the water column (Z_w) and the kelly bushing's elevation (Z_{kb}). Two TVD types will be calculated, namely the True Vertical Depth in respect to the mean sea level (TVDMSL) and the below of seafloor (TVDBSF). Equations 27 and 28 shows the relation to respectively obtain TVDMSL and TVDBSF, while Table 11 shows the water column and kelly bushing's elevation of the three wells.

$$TVDMSL = MD - Z_{kb} \tag{27}$$

$$TVDBSF = MD - (Z_w + Z_{kb}) \tag{28}$$

Table 11: Several values of the water column and Kelly Bushing's elevation for the three wells.

Depth Parameter	Well 34/7-1	Well 6704/12-1	Well 7220/8-1
Water Column [meter] (Z_w)	328	1352	374
Kelly Bushing's Elevation [meter] (Z_{kb})	25	25	23

4.2.4 Extrapolation to The Seafloor

The next step is to extrapolate all relevant logs into the seafloor to have the same array length. This extrapolation would be beneficial for further steps since the same array length means that the logs are tied into the same depth interval, ranging from the seafloor until the Total Depth (TD). The extrapolation uses a MATLAB function named 'log_2_sea_level_new_2.m' and 'merge_log_seabed.m', which could be seen in **Appendix G**. The extrapolation acts as a non-linear connector, which is based on an exponential function. We need to specify the depth of a log when it starts to have a value and the estimated value of the log in the seafloor. Afterward, the code will predict an exponential curve that connects the seafloor until that previously specified depth.

4.2.5 Predict The Missing Density log

After all relevant logs are extrapolated to the seafloor, some values in the bulk density log may not be available in a specific interval, particularly on the shallower or near-seafloor depth intervals. A procedure to tackle this problem is to predict the missing intervals by an empirical equation that relates P-wave velocity to bulk density, proposed by Gardner et al. (1974). It is important to know the lithology of the missing intervals to perform Gardner's empirical approach. Equation 20 is used if the missing intervals consist of clay, while Equation 21 if the missing intervals consist of sand.

$$\rho_b\ [g/cc] = 1.75 \cdot (V_p\ [km/s])^{0.265} \tag{29}$$

$$\rho_b\ [g/cc] = 1.66 \cdot (V_p\ [km/s])^{0.261} \tag{30}$$

It is essential to know the lithology of the given interval before this procedure. The information about the lithology for Well 34/7-1, Well 6704/12-1, and Well 7220/8-1 could respectively be seen in Tables 4, 5, and 7. However, some wells have sufficient values of bulk density log for all of the depth intervals; in this case, then the procedure of using Gardner's approach could be skipped. The only well that does not need to run this procedure is Well 7220/8-1.

4.3 Petrophysical Analysis

The third step's main objective is to obtain several petrophysical parameters based on the pre-conditioned log data on the previous step. Several parameters are defined from this step, such as the porosity and the lithological volume fractions (shale, clay, silt, and sand). These petrophysical parameters are needed for further rock physics analysis and velocity prediction afterward. The substeps of the petrophysical analysis could be seen in Figure 19.

4.3.1 Density Porosity Calculation

After the bulk density log for the whole well is obtained, the density porosity could be calculated. As previously discussed in the second chapter, the density porosity is considered equal to the effective porosity. It could be obtained by using other parameters such as the density of the minerals and the fluid (water), as shown in Equation 8.

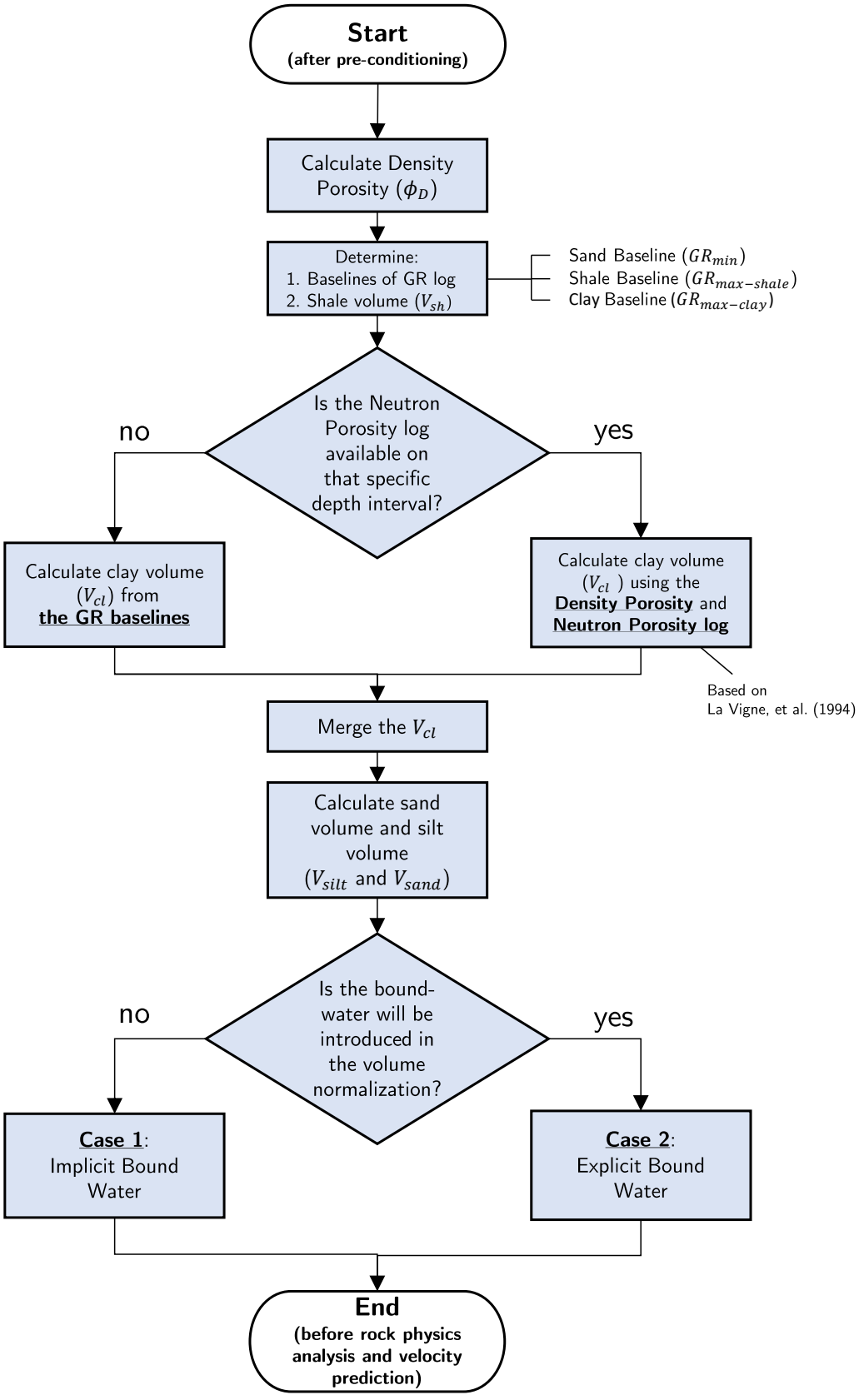

Figure 19: Flowchart for the substeps in the petrophysical analysis step.

4.3.2 Determine the Baselines from Gamma Ray Log

Gamma Ray (GR) is a useful tool for lithological discrimination. Generally, shaly formations have higher Gamma-Ray values, while less shaly formations (such as sands) have lower Gamma-Ray values. It is essential to determine the minimum and maximum values to differentiate the two. The line that represents the minimum Gamma-Ray values is called the sand baseline (GR_{min}), while the line for the maximum Gamma-Ray values is called the shale baseline ($GR_{max,sh}$). Additionally, there is another baseline for clay ($GR_{max,cl}$), which typically higher than the shale baseline since it excludes the silt fraction. In most cases, GR_{min} typically describes the sand volume along the well. However, the GR_{min} in the shallower part of Well 6704/12-1 describes the combination of sand and ooze sediments.

Glover (2005) mentions that wells can have more than one baseline value, either for sand, clay, or shale. Glover also states that baseline determination is usually based on a petrophysicist's experiences; hence, this method is subjective. Nevertheless, we will use several justifications for the chosen values of the baselines.

Both sand and shale baselines are determined based on the lithological information for each of the wells. The sand baseline will naturally be determined from the minimum GR log deflection of a sand formation. In contrast, the shale baseline is based on the maximum GR log deflection of a shaly (mix of clay and silt) formation. As for the clay baseline, it would be determined from the curve fitting between two clay volume fraction calculations; based on the chosen clay baseline value (Equation 32) and the neutron porosity log (Equation 33) for a specific depth interval. If the value for the clay baseline is correct, then the two clay volume curves are expected to be fit or similar for that depth interval. The following paragraphs describe the procedure for each of the wells.

Well 34/7-1

Based on the lithological descriptions for the well (Table 4), two formations could be considered as the representatives for the sand; the basal sand in the Seabed formation (Nordland Group) and sandstone in Lunde Formation. It is essential to realize that the minimum deflections for these two representatives are different, where the basal sand has a lower minimum deflection. If we only use one sand baseline, then naturally, we will choose the basal sand. However, if we do this, then the sand volume on the Lunde Formation would be underpredicted; hence, we decided to use two different sand baselines. The silty claystone in the Jorsalfare Formation (Shetland Group) represents the shale baseline. The Jorsalfare Formation roughly represents many peaks or maximum deflections along the well. Figure 20 shows the curve fitting between the clay volume fraction from $GR_{max,cl}$ and neutron porosity log. Particularly between the well markers of Shetland Group to TD, it is seen that we need to use two different clay baselines in order to get a proper fit between the two clay volume fractions. As the two clay volumes fit, the crossplot between the two clay volumes on the subfigure (d) will be closer to the 45° red line. Table 12 shows the values and references for each of the baselines for Well 34/7-1.

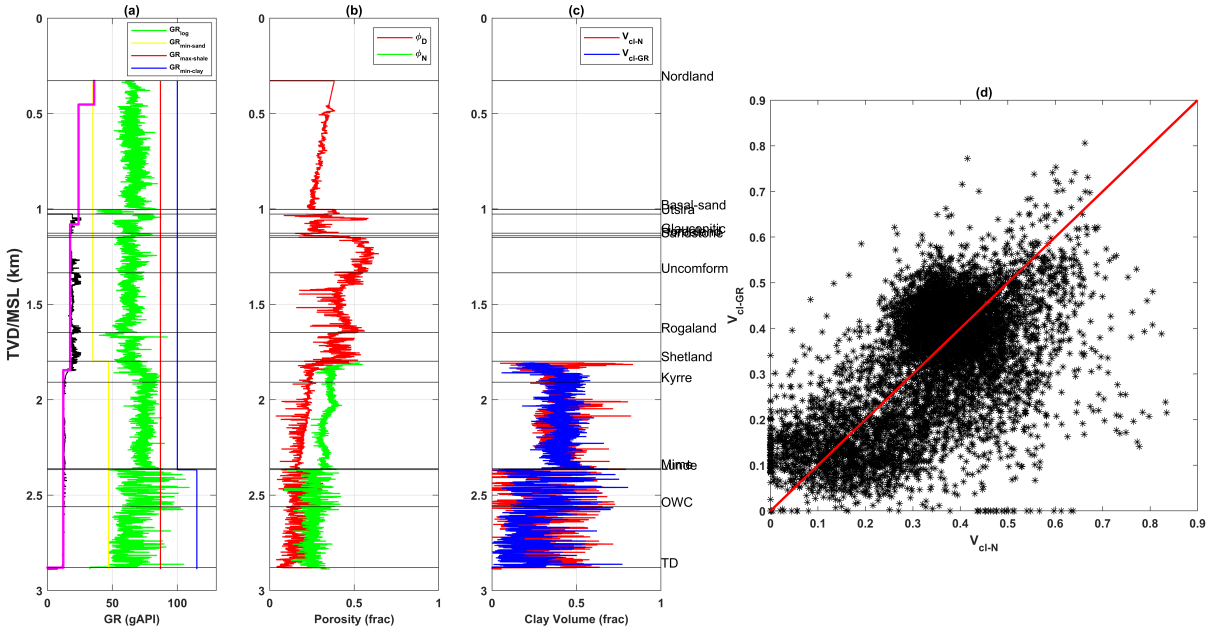

Figure 20: Curve fitting between the clay volume fraction from $GR_{max,cl}$ (V_{cl-GR}) and neutron log (V_{cl-N}) for Well 34/7-1. The magenta and black curves on the GR well window (subfigure a) respectively represent the bit size and caliper log. The red and green curves on the porosity well window (subfigure b) respectively represent the density porosity (ϕ_D) and neutron porosity (ϕ_N). The curve fitting between the clay volume fractions is seen on both subfigures c and d.

Table 12: The determined values of GR baselines for Well 34/7-1.

GR Baselines	Values	References
GR_{min}	35 (Seabed Fm.- Shetland Gp.)	> Basal Sand: Seabed Fm. / Nordland Gp. (Saga Petroleum, 1985)
	47 (Shetland Gp. - TD)	> Sandstone: Lunde Fm. (Saga Petroleum, 1985)
$GR_{max,sh}$	87	> Silty claystone: Jorsalfare Fm. / Shetland Gp. (Saga Petroleum, 1985)
$GR_{max,cl}$	100 (Seafloor - Lunde Fm.)	> Curve fitting between clay volume from baseline and neutron porosity
	115 (Lunde Fm. - TD)	

Well 6704/12-1

Based on the lithological descriptions for the well (Table 5), it is known that the first appearance of sand is in the Middle Brygge Formation, then followed by minor sand in the Lower Brygge Formation and massive sandstone in the Springar Formation. Since the minimum deflections for these three formations are different, we use three different GR_{min} values, which act as the sand baselines. However, the final well report (Aubert et al., 1999) does not indicate any sand presence in the shallower formations before Middle Brygge Formation. Instead, the final well report states that there are siliceous ooze sediments within the shallower part of the well, particularly in Kai and Upper Brygge Formations. It is assumed that these ooze sediments are the primary lithology for this shallower depth interval. A challenge to properly model this shallower interval is that both sand and ooze have low GR values (Awadalkarim et al., 2013). Since sand and ooze sediments have the same low GR values, it is impossible to differentiate the two within this interval. Based on the available information from the final well report, we divide the shallower

interval into an additional three GR_{min} values, which act as the ooze-and-sand baselines. Between the well marker of Naust to Kai Formations, ooze is not yet present, and the only available lithology is clay, so we set the baseline to 0 $gAPI$ to minimize the ooze-and-sand volume. We set the ooze-and-sand baselines between the well marker of Kai - Upper Brygge Formations and the well marker of Upper - Middle Brygge Formations following their minimum deflections, respectively 8 and 15 $gAPI$.

Additionally, we also adjust the ooze-and-sand volume of the Hordaland Group (the whole Brygge Formations) so that the volume is similar to the average sand volume from XRD data from Peltonen et al. (2008). According to the XRD data, the Hordaland Group has a sand volume of around 33.45%, while based on our ooze-and-sand volume within the same Group, we get 34.96% of ooze-and-sand volume, which the values are reasonably close. In total, we use 6 GR_{min} values in this well, consist of three ooze-and-sand baselines in the shallower part and three sand baselines in the deeper part.

The final well report states that the first silt occurrence within the well is in the Middle Brygge Formation; hence, we set both shale and clay baselines to be equal before that specific interval. Both shale and clay baselines are adjusted to follow the maximum and representative formations. Between the well marker of Naust to Upper Brygge Formations, we set the Ooze sediment in Kai Formation as the representative because the siliceous ooze sediments in the Norwegian Sea are usually clay-rich (Awadalkarim et al., 2013). The shale and clay baseline starts to be different in Middle Brygge Formation due to the silt presence in the form of silty clay. Then the baselines between the well marker of Upper Brygge and Tang Formations are determined from the curve fitting and previously mentioned XRD's mineralogical average for clay. The claystone in the Nise Formation is a clear representative for determining the shale baseline on the deeper part of the well. Many peaks on Nise Formation align with the chosen baseline value. Both shale and clay baselines in the Hordaland Group are adjusted to follow the XRD data in a similar way as for the sand volume. The XRD states that the clay volume should be around 49.1%, while our baselines obtain 57.64% of clay volume.

Figure 21 shows the curve fitting between the clay volume fraction from $GR_{max,cl}$ and neutron porosity log. Particularly between in the middle of Mid. Brygge Formation to TD, it is seen that we need to use three clay and four shale baselines in order to get a proper fit between the two clay volume fractions. As the two clay volumes fit, the crossplot between the two clay volumes on the subfigure (d) will be closer to the 45° red line. Since the neutron log is not available on the shallower formations, we need to consider the lithological information. It is known that the well has ooze sediments in Kai and Upper Brygge Formations. Awadalkarim et al. (2013) describe the siliceous ooze sediments in the Norwegian Sea as sediment with abundant amounts of clay; hence, it is justifiable to draw the clay baseline from one of those ooze formations. Table 13 shows the values and references for each of the baselines for Well 6704/12-1.

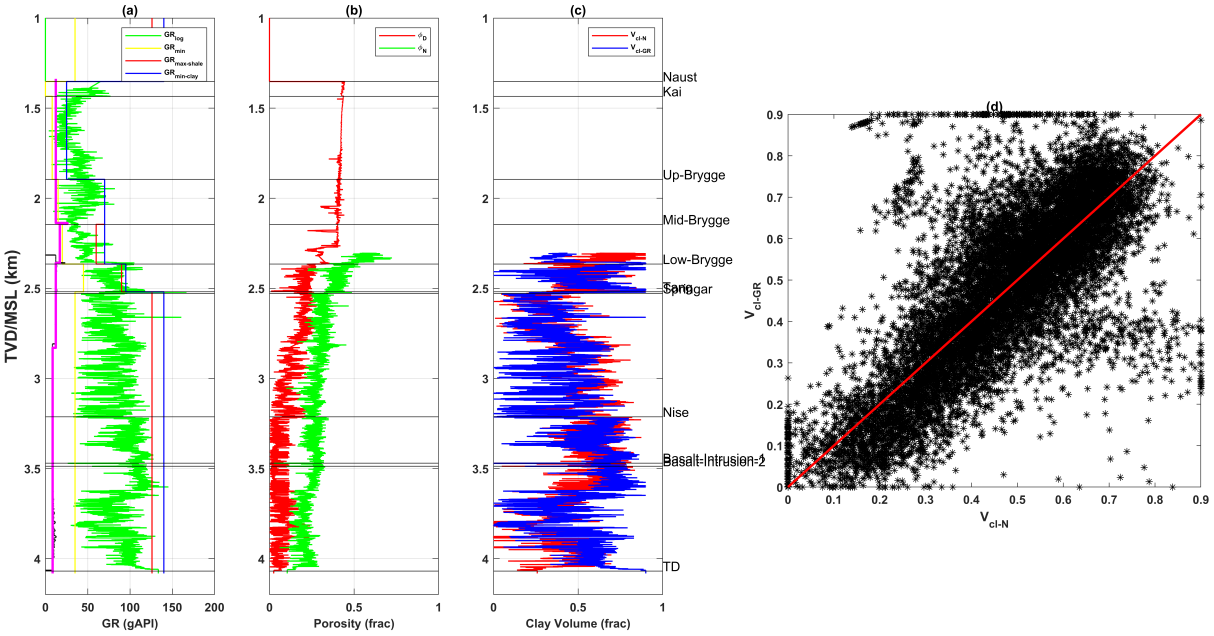

Figure 21: Curve fitting between the clay volume fraction from $GR_{max,cl}$ (V_{cl-GR}) and neutron log (V_{cl-N}) for Well 6704/12-1. The magenta and black curves on the GR well window (subfigure a) respectively represent the bit size and caliper log. The red and green curves on the porosity well window (subfigure b) respectively represent the density porosity (ϕ_D) and neutron porosity (ϕ_N). The curve fitting between the clay volume fractions is seen on both subfigure c and d.

Table 13: The determined values of GR baseline for Well 6704/12-1.

GR Baselines	Values	References
GR_{min}	0 (Seabed/Naust Fm. - Kai Fm.)	> No sand and ooze sediments presence in this interval. Only clay (Aubert et al., 1999)
	8 (Kai Fm. - U. Brygge Fm.)	> Ooze sediments is present in this interval (Aubert et al., 1999)
	15 (U. Brygge Fm. - M. Brygge Fm.)	> Adjustment to quartz average of XRD data for Hordaland Gp. (Peltonen et al., 2008)
	20 (M. Brygge Fm. - L. Brygge Fm.)	> Minor sand: M. Brygge Fm. (Aubert et al., 1999). > Adjustment to quartz average of XRD data for Hordaland Gp. (Peltonen et al., 2008)
	45 (L. Brygge Fm. - Tang Fm.)	> Minor sandstone: L. Brygge Fm. (Aubert et al., 1999) > Adjustment to quartz average of XRD data for Hordaland Gp. (Peltonen et al., 2008)
	35 (Tang Fm. - TD)	> Massive Sandstone: Springar Fm. (Aubert et al., 1999)
$GR_{max,sh}$	25 (Seabed/Naust Fm. - U. Brygge Fm.)	> No silt presence in this interval (Aubert et al., 1999); $GR_{max,sh} = GR_{max,cl}$
	70 (U. Brygge Fm. - M. Brygge Fm.)	> Curve fitting between clay volume from baseline and neutron porosity > Adjustment to clay average of XRD data for Hordaland Gp. (Peltonen et al., 2008) > No silt presence in this interval (Aubert et al., 1999); $GR_{max,sh} = GR_{max,cl}$
	60 (M. Brygge Fm. - L. Brygge Fm.)	> Silt is presence in the silty clay (Aubert et al., 1999)
	90 (L. Brygge Fm. - Tang Fm.)	> Adjustment to clay average of XRD data for Hordaland Gp. (Peltonen et al., 2008). > Curve fitting between clay volume from baseline and neutron porosity
	126 (Tang Fm. - TD)	> Claystone: Nise Fm. (Aubert et al., 1999)
$GR_{max,cl}$	25 (Seabed/Naust Fm. - U. Brygge Fm.)	> Clay-rich ooze sediments in Kai Fm. and U. Brygge Fm. (Aubert et al., 1999; Awadalkarim et al., 2013) > No silt presence in this interval (Aubert et al., 1999); $GR_{max,sh} = GR_{max,cl}$
	70 (U. Brygge Fm. - M. Brygge Fm.)	> Curve fitting between clay volume from baseline and neutron porosity > Adjustment to clay average of XRD data for Hordaland Gp. (Peltonen et al., 2008). > No silt presence in this interval (Aubert et al., 1999); $GR_{max,sh} = GR_{max,cl}$
	70 (M. Brygge Fm. - L. Brygge Fm.)	> Curve fitting between clay volume from baseline and neutron porosity > Adjustment to clay average of XRD data for Hordaland Gp. (Peltonen et al., 2008). > Silt is presence in the silty clay (Aubert et al., 1999)
	95 (L. Brygge Fm. - Tang Fm.)	> Curve fitting between clay volume from baseline and neutron porosity
	140 (Tang Fm. - TD)	> Curve fitting between clay volume from baseline and neutron porosity

Well 7220/8-1

Based on the lithological descriptions for the well (Table 7), two formations could be considered as the representatives for the sand, mainly the mature sandstone in the Stø Formation and shaly sandstone in Tubåen Formation. Fortunately, the minimum deflections between the two representatives are pretty close, so we will only use one sand representative with a smaller value of minimum deflection; the sandstone in Stø Formation. It is given that the Fruholmen Formation is a shale formation; hence, this formation is considered as the representative for the shale baseline.

Figure 22 shows the curve fitting between the clay volume fraction from $GR_{max,cl}$ and neutron porosity log. Particularly between in the middle of the Sotbakken Group to TD, it is seen that we need to use two different clay baselines in order to get a proper fit between the two clay volume fractions. As the two clay volumes fit, the crossplot between the two clay volumes on the subfigure (d) will be closer to the 45° red line. Table 14 shows the values and references for each of the baselines for Well 7220/8-1.

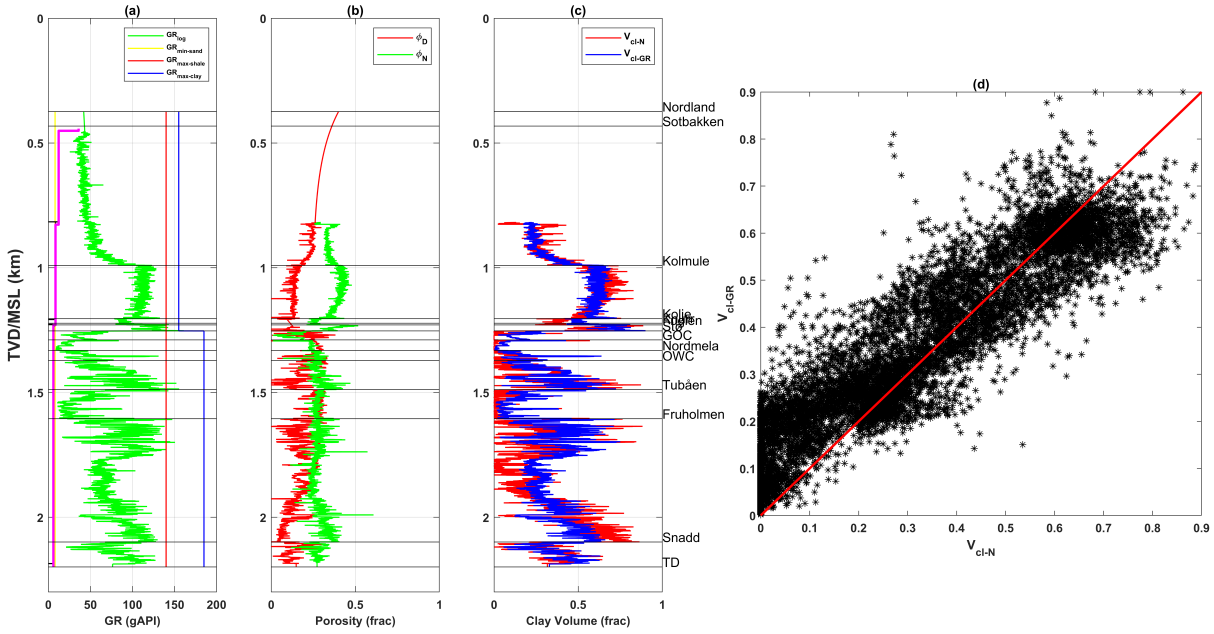

Figure 22: Curve fitting between the clay volume fraction from $GR_{max,cl}$ (V_{cl-GR}) and neutron log (V_{cl-N}) for Well 7220/8-1. The magenta and black curves on the GR well window (subfigure a) respectively represent the bit size and caliper log. The red and green curves on the porosity well window (subfigure b) respectively represent the density porosity (ϕ_D) and neutron porosity (ϕ_N). The curve fitting between the clay volume fractions is seen on both subfigure c and d.

Table 14: The determined values of GR baseline for Well 7220/8-1.

GR Baselines	Values	References
GR_{min}	8	> Mature sandstone: Stø Fm. (NPD Factpage)
$GR_{max,sh}$	140	> Shale: Fruholmen Fm. (NPD Factpage)
$GR_{max,cl}$	155 (Seabed Fm. - Stø Fm.)	> Curve fitting between clay volume from baseline and neutron porosity
	185 (Stø Fm. - TD)	

4.3.3 Determine the Lithological Volume Fraction

After the baselines are determined, then we can proceed to calculate the lithological volume fraction. Equation 31 shows the equation to calculate the shale volume (V_{shale}) based on its baseline.

$$V_{shale}\ [Frac.] = \frac{GR_{log} - GR_{min}}{GR_{max,sh} - GR_{min}} \cdot (1 - \phi_D) \tag{31}$$

Where GR_{log} is the extrapolated Gamma Ray log to the seafloor, GR_{min} is the sand baseline, $GR_{max,sh}$ is the shale baseline, and ϕ_D is the density porosity. The clay volume (V_{clay}) estimation depends on the availability of the neutron porosity logs on the specific depth interval. If the neutron porosity log is not present, then the clay volume estimation depends on the clay baseline ($GR_{max,cl}$), as shown in Equation 32.

$$V_{clay}\ [Frac.] = \frac{GR_{log} - GR_{min}}{GR_{max,cl} - GR_{min}} \cdot (1 - \phi_D) \tag{32}$$

If the neutron porosity is present, then we estimate the clay volume based on the relation between density porosity and neutron porosity (ϕ_N), as proposed by La Vigne et al. (1994), in Equation 33.

$$V_{clay}\ [Frac.] = \frac{\phi_N - \phi_D - (-0.025)}{\phi_{N,dry-cl}} \tag{33}$$

Where $\phi_{N,dry-cl}$ is the average dry-clay neutron porosity, obtained from Equation 15. Assuming the four clay minerals present in a balance proportion, then the value of this parameter is around 0.4075 or 40.75%. The clay volume estimation from Equation 32 and Equation 33 then merged.

It is decided that we use the clay volume determination either from the baseline or neutron porosity log. Glover (2005) explains that the baseline determination is based on the petrophysicist's experience; hence, it is prone to be subjective. Even though that we use a consistent procedure, it might not guarantee reliable results. Furthermore, this clay volume determination from the baselines is based on the index gamma-ray (IGR) approach. According to Sharma and Chopra (2019), the IGR method tends to overestimate the clay volume due to its linearity, compared to the improved non-linear IGR correction by other studies (Larionov, 1969; Clavier et al., 1971; Thomas and Stieber, 1975) as shown in Figure 23.

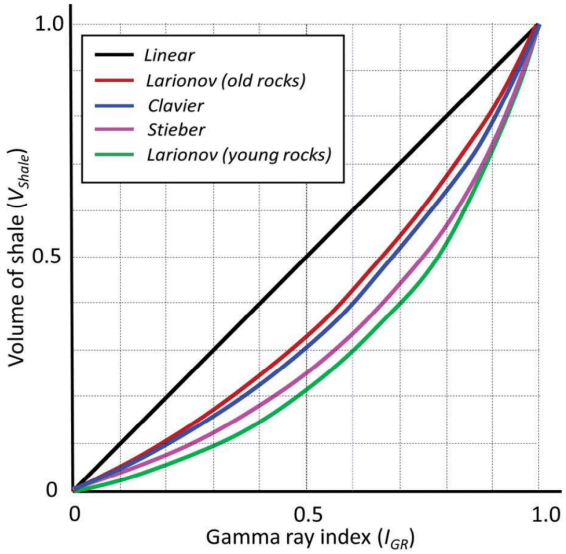

Figure 23: The comparison of clay or shale volume by using the linear IGR and some other improved non-linear corrections for IGR. (Taken from Sharma and Chopra, 2019)

On the other hand, La Vigne et al. (1994) propose a clay volume determination based on the theoretical endpoint for the sandstone's neutron porosity; hence, the procedure is more data-driven and objective. Nevertheless, several issues might occur, such as: (1) The neutron porosity might not be available for all depth intervals, so we cannot use La Vigne's approach. (2) Currently, we assume that the volume percentage of each 4 common clay minerals are equal (Table 1), so that we obtain the average dry-clay neutron porosity ($\phi_{N,dry-cl}$) as shown in Equation 15. However, it is most likely that the percentages of the four clay minerals are different, so that the value of $\phi_{N,dry-cl}$ should be adjusted. An option to estimate each of the clay volumes is by using the spectral gamma-ray.

After obtaining the shale and clay volumes fractions, we estimate the silt volume by subtracting the two volumes fractions, as shown in Equation 34.

$$V_{silt}\ [Frac.] = V_{shale} - V_{clay} \tag{34}$$

As for the sand volume fraction, then we should refer to the schematic shaly sand reservoir (Figure 3), proposed by Peeters and Holmes (2014). Then the Equation 9 could be rewritten as shown in Equation 35, where the total volume is 100% or 1. Then the sand volume fraction could be calculated by using Equation 36.

$$1 = V_{sand} + V_{shale} + \phi_D \tag{35}$$

$$V_{sand}\ [Frac.] = 1 - (V_{shale} + \phi_D) \tag{36}$$

4.3.4 Normalization of Lithological Volume Fraction: Implicit and Explicit Clay-Bound Water Model

The purpose of the lithological volume normalization is to exclude the porosity effect from the total volume of the rock; hence, the volume fraction would only describe the solid part of the rock. We proposed two models, namely the implicit and explicit clay-bound water models. The main difference between the two is that for the implicit model, it assumes that the volume of clay-bound water is implicitly present inside the shale volume, specifically inside the clay volume. Implicit means that the clay-bound water is there, but we cannot define its volume. As for the explicit model, clay volume will be separated into dry-clay volume and clay-bound water volume. In this particular case, we could explicitly define the clay-bound water volume. The implicit bound water model could be seen as a rewritten version of Equation 35, with an additional procedure to normalized the density porosity from the equation, as shown in the following equations.

$$\begin{aligned} V_{sand} + V_{shale} &= 1 - \phi_D \\ V_{sand} + (V_{clay} + V_{silt}) &= 1 - \phi_D \end{aligned} \tag{37}$$

$$\begin{aligned} \frac{V_{sand}}{1-\phi_D} + \frac{V_{clay}}{1-\phi_D} + \frac{V_{silt}}{1-\phi_D} &= 1 \\ V_{sand,norm-1} + V_{clay,norm-1} + V_{silt,norm-1} &= 1 \end{aligned} \tag{38}$$

Where the $V_{sand,norm-1}$, $V_{clay,norm-1}$, and $V_{silt,norm-1}$ are respectively the normalized volume fractions of sand, clay, and silt for the implicit bound water model (Model 1). As for the explicit bound water model (Model 2), then Equation 37 is rewritten as:

$$V_{sand} + [(V_{dry-clay} + V_{cbw}) + V_{silt}] = 1 - \phi_D \tag{39}$$

Where $V_{dry-clay}$ and V_{cbw} are respectively the volume fractions of dry clay and bound water, as already discussed in the second chapter, the bound water could be defined the same way as in the total porosity (Equation 14). So that the normalization for model 2 is shown in Equation 40.

$$\begin{aligned} \frac{V_{sand}}{1-\phi_D} + \frac{V_{dry-clay}}{1-\phi_D} + \frac{V_{dry-clay} \cdot \phi_{N,dry-cl}}{1-\phi_D} + \frac{V_{silt}}{1-\phi_D} + &= 1 \\ V_{sand,norm-2} + V_{clay,norm-2} + V_{cbw,norm-2} + V_{silt,norm-2} &= 1 \end{aligned} \tag{40}$$

Notice that the normalized non-clay (sand and silt) volumes for the two models are equal.

However, the normalized clay for model 1 should be slightly higher than for model 2 since the clay volume in model 1 represents the bulk or total clay volume. In contrast, the explicit model represents the clay volume as the dry-clay volume, where the bound-water is explicitly separated. We also need to specify the normalized shale volume for both of the models, as shown in Equations 41 and 42.

$$V_{shale,norm-1} = V_{clay,norm-1} + V_{silt,norm-1} \tag{41}$$

$$V_{shale,norm-2} = V_{clay,norm-2} + V_{cbw,norm-2} + V_{silt,norm-2} \tag{42}$$

Even though the normalized shale-volume equations for both models are slightly different, these two normalized volumes have the same values, similar to their normalized non-clay volumes.

All in all, these two normalization models follow precisely the same typical shaly sand model as provided by Peeters and Holmes (2014), in Figure 3. These normalized volume fractions are needed for several calculations in the next substeps of the Rock physics analysis and Velocity prediction.

4.4 Rock Physics Analysis and Velocity Prediction

After all of the needed petrophysical parameters are obtained, we proceed to the most important steps in this proposed methodology: the rock physics analysis and velocity prediction. The main ideas of these steps are to model the Voigt and Reuss bounds of several rock-physics parameters and define the weight parameter by some physical explanations. Afterward, the Bounding Average Method (BAM) could predict the P- and S- wave velocities. Figure 24 shows the substeps, and the following subchapters explain the details of each substep.

4.4.1 Temperature Profile Determination

The temperature profile describes the temperature changes from the seafloor until the total depth (TD). This temperature profile is later used for the fluid's effective density and bulk modulus calculation. In most cases, the temperature shows a positive rate of change with depth; hence, an increase in depth follows an increase in temperature. The following procedures for the temperature profile determination are based on Duffaut et al. (2018). Equation 43 shows how the temperature profile along the well is predicted, where T_0 is the temperature at the seafloor, Q_0 is the surface heat flow, k is the thermal conductivity, and z is the depth.

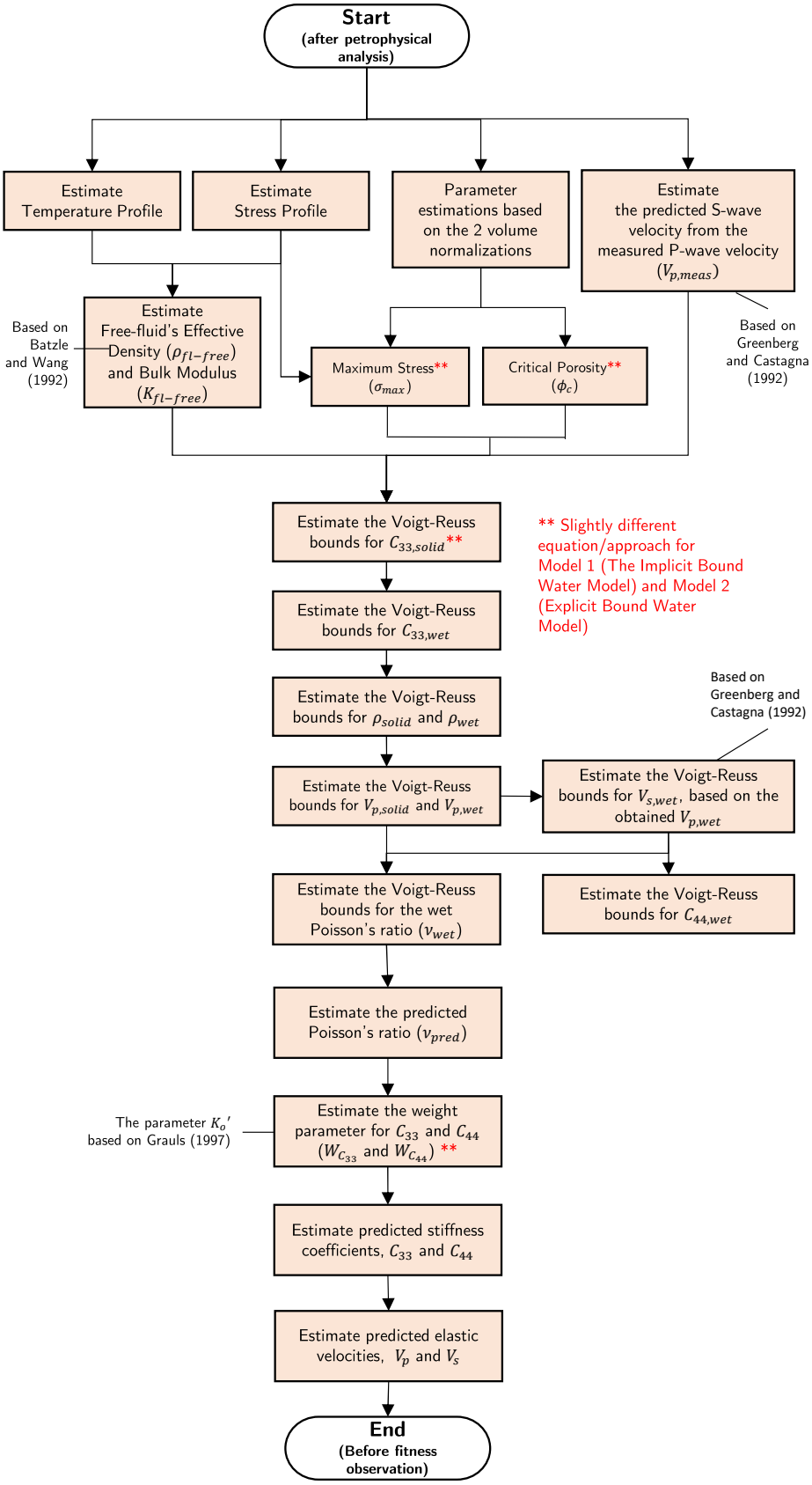

Figure 24: Flowchart for the substeps in the rock physics analysis and velocity prediction steps.

$$T(z) = T_0 + \frac{Q_0}{k} z \tag{43}$$

We assumed that the temperature of the water column is constant with the same value as T_0. Then the thermal conductivity is calculated (Equation 44); where a_0 is the initial thermal conductivity at the seafloor, V_p is the P-wave velocity log, and $V_{cl-bulk}$ is the non-normalized bulk clay volume fraction (which equal to V_{cl} in model 1) for both models.

$$k = a_0 + (1 - V_{cl-bulk})V_p \tag{44}$$

The thermal conductivity of the water column is equal to the typical thermal conductivity of seawater ($k_{sea\ water}$). Table 15 shows several values for the mentioned parameters.

Table 15: Several parameters value for the temperature profile determination. (Taken from Hantschel and Kauerauf, 2009; Allen and Allen, 2006; and the NPD's final well report for each of the well)

Well	T_0 [°C] (NPD's Report)	Q_0 [W/m^2] (Hantschel and Kauerauf, 2009)	a_0 [$W/m\ °C$] (Allen and Allen, 2006)	$k_{seawater}$ [$W/m\ °C$] (Allen and Allen, 2006)
34/7-1	3.3	0.0655	1	0.6
6704/12-1	-2.4			
7220/8-1	1.4			

4.4.2 Stress Profile Determination

Similarly, with the temperature profile, the stress profile describes the changes of the stress from the seafloor until the total depth (TD). Three types of stress would be considered, namely the lithostatic stress (σ), pore pressure (P_p), and effective stress (σ'). Equation 45 shows the relation between the three stress types, where α is the Biot's coefficient. In most of the cases, the Biot's coefficient is assumed to be 1 (Bodaghabadi and Moosavi, 2008).

$$\sigma' = \sigma + \alpha P_p \tag{45}$$

The lithostatic stress describes the stress due to the overburdened materials, while in most cases, pore pressure usually close or equivalent to the hydrostatic stress. This hydrostatic stress describes the stress in a scenario where a water column replaces all the overburdening materials. The effective or differential stress represents the difference between lithostatic stress and pore pressure. Both lithostatic and hydrostatic stress could be calculated by respectively using Equations 46 and 47.

$$\sigma = g \int_a^b \rho_b(z)\, dz + \rho_w g Z_w \tag{46}$$

$$P_p = g \int_a^b \rho_w(z)\, dz + \rho_w g Z_w \tag{47}$$

Where ρ_b is the measured bulk density log, ρ_w is the water density (around 1 g/cc), z is the depth, Z_w is the depth of the water column (depends for each of the well, as seen in Table 11), and g is the gravity acceleration constant (around 9.8 m/s^2). There are two conditions where the hydrostatic pressure does not represent the well's pore pressure; if the pore pressure is higher than the hydrostatic pressure, then this might be the case for an overpressure well, while the opposite of this condition is called underpressure well. Based on the final well report, it is known that overpressure is occurred on Well 34/7-1, while the rest of the wells show the pore pressure quite close or the same as the hydrostatic stress.

4.4.3 Critical Porosity Determination

As previously discussed in the second chapter, critical porosity (ϕ_c) is a limit of porosity that differentiates the frame-supported rock and fluid-supported suspension (Figure 4). Fawad et al. (2010) provide some porosity values for a mixture of silt-clay, while Nur et al. (1998) describe several critical porosity values for several lithologies as seen in Table 2. Hence, the critical porosity of solid sand, silt, and clay could be defined from these two references, as shown in Table 16.

Table 16: Critical porosity for sand, silt, and clay (Nur et al., 1998; Fawad et al., 2010)

Lithology	**Critical Porosity (ϕ_c)**
Sand	40%
Silt	55%
Clay	71%

Fawad et al. show a linear increase in porosity for a clay-silt mixture as the clay fraction increases; hence, it is reasonable to assume that the critical porosity would act the same. Then we proposed a procedure to estimate the critical porosity by considering the normalized volume fractions for both models (Equations 38 and 40 respectively for Models 1 and 2) and the values from Table 16. However, since the critical porosity only describes the solid parts, we need to normalize the clay-bound water volume from Model 2. Equations 48 and 49 respectively show the critical porosity estimation for Models 1 and 2.

$$\phi_{c-1} = V_{sand,norm-1} \cdot \phi_{c,sand} + V_{silt,norm-1} \cdot \phi_{c,silt} + V_{clay,norm-1} \cdot \phi_{c,clay} \tag{48}$$

$$\phi_{c-2} = \frac{V_{sand,norm-2}}{(1 - V_{cbw,norm-2})} \cdot \phi_{c,sand} + \frac{V_{silt,norm-2}}{(1 - V_{cbw,norm-2})} \cdot \phi_{c,silt} + \frac{V_{clay,norm-2}}{(1 - V_{cbw,norm-2})} \cdot \phi_{c,clay} \tag{49}$$

Using one of these equations, we could predict the critical porosity log for the whole depth intervals of the well. These critical porosity logs are essential for Poisson's ratio determination.

4.4.4 Maximum Stress Determination

The maximum stress defined as a specific lithostatic or overburden stress value that makes all of the pores inside a rock vanished due to compaction; in other words, the rock would have no porosity left. When a rock reaches this condition, then the P-wave velocity that passes through would describe the solid aggregate of the rock. This P-wave velocity is then called the terminal velocity. Therefore, when the terminal velocity is reached, then the current affecting stress is the maximum stress. The first procedure for this maximum stress determination is to calculate the ratio of sand and clay for the whole depth intervals of the well. The sand ratio could be calculated as seen in Equation 50.

$$rat_{sand-x} = \frac{1}{n} \cdot \sum_{i=1}^{n} \left(\frac{V_{sand,norm-x,i}}{V_{sand,norm-x,i} + V_{clay,norm-x,i}} \right) \tag{50}$$

Where n is the number of all depth points in a well, while index x could be replaced by 1 or 2, depends on what normalization model is used. The clay ratio could be calculated by using Equation 51.

$$rat_{clay-x} = 1 - rat_{sand-x} \tag{51}$$

Afterward, we proceed to calculate the terminal velocity by using Equation 52.

$$V_{p,terminal-x} = \sqrt{\frac{rat_{sand-x} \cdot M_{qz} + rat_{clay-x} \cdot C_{33,clay}}{rat_{sand-x} \cdot \rho_{qz} + rat_{clay-x} \cdot \rho_{clay}}} \tag{52}$$

Then we need to plot two parameters, namely the lithostatic stress (calculated by using Equation 46) against the P-wave velocity. Figure 25 shows the plots for the three wells for both models. The red line is obtained from a linear regression between the two parameters, where all of the linear regression equations could be seen in Table 17. The linear regression is based on the linear inversion solution as discussed by Grandis (2009). The maximum stress values could be obtained by including each terminal velocity value, as seen in the same table.

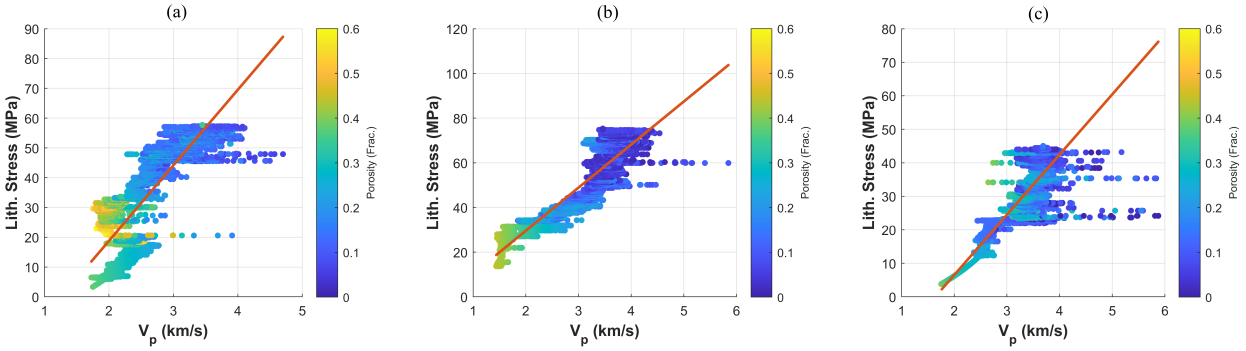

Figure 25: The plots for lithostatic stress in respect to the P-wave velocity for the (a) Well 34/7-1, (b) Well 6704/12-1, and (c) Well 7220/8-1. The red lines are the linear regression between the two parameters.

Table 17: The linear regression equations, terminal velocities, and maximum stresses for the three wells. For each of the proposed normalization models.

Well	**Model**	**Linear Regression Equation for σ (Lith. Stress)**	**Terminal Velocity ($V_{p,term}$) [km/s]**	**Maximum Stress (σ_{max}) [MPa]**
34/7-1	1	$25.3806V_p - 31.9824$	4.9423	93.4561
	2		4.5698	84.0019
6704/12-1	1	$19.2881V_p - 9.0064$	5.0084	87.5961
	2		4.5784	79.3022
7220/8-1	1	$17.9738V_p - 29.4382$	5.1410	62.9651
	2		4.3596	48.9204

4.4.5 Predicted S-wave Velocity Determination from the Measured P-wave Velocity

As previously discussed in the pre-conditioning step, some wells either do not have a shear sonic log or only partially available for selected depth intervals. For one of these cases, then it is technically impossible to use Equation 26 to obtain the S-wave velocity log for the whole depth intervals of the well. In order to sort this problem, we can use an empirical relation for estimating the S-wave velocity (V_s) from P-wave velocity (V_p). One empirical approach is based on the polynomial relations within the pure monomineralic lithologies, as proposed by Greenberg and Castagna (1992). The first procedure to perform this empirical relation is to estimate the V_s for pure sandstone and shale, as respectively seen in Equations 53 and 54. Note that Greenberg and Castagna also provide the equations for pure dolomite and limestone.

$$V_{s-GC,sand} = 0.80416V_p - 0.85588 \tag{53}$$

$$V_{s-GC,shale} = 0.76969V_p - 0.86735 \tag{54}$$

After both monomineralic S-wave velocities for sandstone and shale are obtained, then we proceed to calculate the arithmetic and harmonic means based on the two of them, as seen in Equations 55 and 56, respectively.

$$V_{s-GC,arith} = V_{sand,norm-x}V_{s-GC,sand} + V_{shale,norm-x}V_{s-GC,shale} \tag{55}$$

$$V_{s-GC,harm} = \left(\frac{V_{sand,norm-x}}{V_{s-GC,sand}} + \frac{V_{shale,norm-x}}{V_{s-GC,shale}}\right)^{-1} \tag{56}$$

The index x could be changed into 1 or 2, depending on the chosen model. Noted that the normalized shale volume fraction between the two models are having the same value despite of slightly different equation (Equation 41 for model 1 and Equation 42 for model 2). The normalized sand volume fractions for both models 1 and 2 also have the same value. Then the predicted V_s from measured V_p could be estimated from the average between the arithmetic and harmonic means, as seen in Equation 57.

$$V_{s-GC} = \frac{V_{s-GC,arith} + V_{s-GC,harm}}{2} \tag{57}$$

As previously shown in Table 3, the Well 34/7-1 is the only well that does not have the shear sonic log; hence, this well does not have any actual measured S-wave velocity. It is important to emphasize that the S-wave velocity estimated from the measured P-wave velocity by the Greenberg-Castagna (GC) approach is not an actual measured S-wave velocity. On the contrary, the Well 6704/12-1 has a shear sonic log, but it does not cover all the depth intervals within the well, particularly on the shallower depth; hence, the measured S-wave velocity for the shallower interval is estimated by the GC approach. Fortunately for the Well 7220/8-1, the shear sonic log covers all of the depth intervals so that the GC approach is not performed on this well.

4.4.6 Free-fluid's Effective Density and Bulk Modulus Determination

The proposed methodology (particularly for Model 2) introduces both bound water and free fluid. As previously explained in Figure 3, the bound water is identified as the immovable water within the pure clay. In contrast, free fluid is identified as the movable fluid (could be water, hydrocarbon, or both) within the rock. A combination between bound water and free water describes the total porosity (Equation 14), while only the free water describes the effective porosity (Equation 10). Since these two water volumes are introduced into the model, it is important to specify the relevant parameters, such as the density and bulk modulus. Kolstø (2012) mentions several values of the two parameters for bound water (Table 8), while Batzle and Wang (1992) provides comprehensive procedures to calculate the two parameters for the free fluid.

With a focus on performing the Batzle and Wang's procedure, then we need to specify several needed parameters: the salinity, oil gravity, gas gravity, gas-oil-ratio (GOR), gas index in brine, gas index in oil, temperature profile, pore pressure profile, oil saturation, and gas saturation. The only parameters that previously obtained are the temperature profile (Equation 43) and the pore pressure profile (Equation 47). For the hydrocarbon saturation, each well has its own condition, as already stated in the third chapter. Well 34/7-1 is an oil well, where the data of oil saturation from the conventional core analysis is present in the final well report (**Appendix B**). Well 6704/12-1 is a dry well; hence, the hydrocarbon saturation for all depth intervals is zero. Well 7220/8-1 is a gas-oil well, where the hydrocarbon saturation is assumed to be the same as the hydrocarbon saturation in Well 7220/11-3, provided by Hansen (2019).

Teng (1997) from the RPHtools website provided a MATLAB function code (flprop.m, as seen in **Appendix H**) that is used to perform the Batzle and Wang's procedure. He also provides several default values for the rest of the needed parameters, as seen in Table 18. The MATLAB function provides two different bulk modulus for the free-fluid; for non-patchy saturation and patchy saturation. The non-patchy saturation means that the water and hydrocarbon are mixed at a length scale such that the wave-induce pore pressure is equilibrated homogeneously (Dvorkin et al., 2003). On the other hand, the patchy saturation means that both water and hydrocarbon are not well mixed; hence, the two fluid-phases have their compartment within the pore space. The non-patchy saturation yields the lower limit (Reuss) value for the bulk modulus, while the patchy saturation yields the higher limit (Voigt) value. If the pore space of a specific depth interval only has water, then the bulk modulus values in both non-patchy and patchy conditions are the same. This study assumes that the fluid mixing between the two fluid phases is in a non-patchy condition. The function also estimates the effective density of the fluid mixing, where the values are the same for both patchy and non-patchy conditions.

Table 18: Several needed parameters value to perform the Batzle and Wang (1992) procedure, provided by Teng (1997).

Parameters	Values	Parameters	Values
Salinity of NaCl [ppm]	34000	GOR (L/L)	100
Oil Gravity [API number]	30	Gas Index in brine [Frac.]	0
Gas Gravity [Specific Gravity]	0.6	Gas index in oil [Frac.]	0

4.4.7 The Voigt - Reuss Bounds Determination for the Stiffness Coefficients and Wet Velocities

After all of the previous substeps are performed, we estimate the Voigt-Reuss bounds for several rock-physics parameters: the solid C_{33}, the wet C_{33}, wet P-wave velocity, wet S-wave velocity, wet C_{44}, and wet Poisson's ratio. For the first parameter, the Voigt and Reuss bounds of the solid C_{33} could respectively obtained from Equations 58 and 59 for model 1.

$$C_{33,solid,V-1} = V_{clay,norm-1} \cdot C_{33,Clay} + (1 - V_{clay,norm-1}) \cdot M_{qz} \tag{58}$$

$$C_{33,solid.R-1} = \left(\frac{V_{clay,norm-1}}{C_{33,Clay}} + \frac{1 - V_{clay,norm-1}}{M_{qz}} \right)^{-1} \tag{59}$$

or Equations 60 and 61 for model 2

$$C_{33,solid,V-2} = V_{clay,norm-2} \cdot C_{33,Clay} + V_{non-cl,norm-2} \cdot M_{qz} + V_{cbw,norm-2} \cdot K_{cbw} \tag{60}$$

$$C_{33,solid.R-2} = \left(\frac{V_{clay,norm-2}}{C_{33,Clay}} + \frac{V_{non-cl,norm-2}}{M_{qz}} + \frac{V_{cbw,norm-2}}{K_{cbw}} \right)^{-1} \tag{61}$$

Where the normalized non-clay volume of model 2 ($V_{non-cl,norm-2}$) is obtained from Equation 62, and the P-wave modulus of quartz (M_{qz}) for both models is obtained from Equation 63.

$$V_{non-cl,norm-2} = V_{sand,norm-2} + V_{silt,norm-2} \tag{62}$$

$$M_{qz} = K_{qz} + \frac{4}{3} G_{qz} \tag{63}$$

A special treatment for estimating the solid bounds of C_{33} is implemented in the shallower part of Well 6704/12-1 due to the presence of ooze sediments. The M_{qz} in the previous equations (Equations 58 to 61) are replace by the P-wave modulus of Ooze sediments (M_{oz}), obtained in a similar way as Equation 63, as shown in Equation 64.

$$M_{oz} = K_{oz} + \frac{4}{3}G_{oz} \tag{64}$$

The bulk and shear moduli of ooze sediments (K_{oz} and G_{oz}) are estimated from Breitzke (2000), as seen in Subchapters 3.2 and 4.1. Then proceed to calculate the Voigt and Reuss bound for wet C_{33}, as shown in Equations 65 and 66.

$$C_{33,wet,V-x} = (1 - \phi_D) \cdot C_{33,solid,V-x} + \phi_D \cdot K_{free-fluid} \tag{65}$$

$$C_{33,wet,R-x} = \left(\frac{1 - \phi_D}{C_{33,solid,R-x}} + \frac{\phi_D}{K_{free-fluid}} \right)^{-1} \tag{66}$$

The $K_{free-fluid}$ is the bulk modulus of the free fluid, obtained from the previously discussed Batzle and Wang (1992) approach, assuming the fluid mixing is in a non-patchy saturation. ϕ_D is the density porosity or the effective porosity, while the index x could be replaced by the chosen normalization model, 1 or 2. For the next step, we need to estimate the solid and wet density as respectively seen in Equations 67 and 68.

$$\rho_{solid-x} = (1 - V_{clay,norm-x}) \cdot \rho_{qz} + V_{clay,norm-x} \cdot \rho_{cl} \tag{67}$$

$$\rho_{wet-x} = (1 - \phi_D) \cdot \rho_{solid-x} + \phi_D \cdot \rho_{free-fluid} \tag{68}$$

The $\rho_{free-fluid}$ is the density of the free-fluid, obtained in a similar procedure with the $K_{free-fluid}$. Then the Voigt and Reuss bounds for the wet P-wave velocity could be obtained as seen in Equations 69 and 70.

$$V_{p,wet,V-x} = \sqrt{\frac{C_{33,wet,V-x}}{\rho_{wet-x}}} \tag{69}$$

$$V_{p,wet,R-x} = \sqrt{\frac{C_{33,wet,R-x}}{\rho_{wet-x}}} \tag{70}$$

Since the Voigt-Reuss bounds calculations for C_{33} are completed, we also need to do the same for C_{44}. To do this, then we need to estimate the wet S-wave velocity based on the estimated wet P-wave velocity (Equations 69 and 70) by performing the Greenberg and Castagna (1992) empirical approach. The first procedure for this S-wave velocity (V_s) estimation is by calculating the monomineralic constituent of the V_s for both sandstone (SS) and shale (SH) of the Voigt bound (Equations 71 and 72) and the Reuss bound (Equations 73 and 74).

$$V_{s,wet,V,SS-x}\ [km/s] = 0.80416\ V_{p,wet,V-x} - 0.85588 \tag{71}$$

$$V_{s,wet,V,SH-x}\ [km/s] = 0.76969\ V_{p,wet,V-x} - 0.86735 \tag{72}$$

$$V_{s,wet,R,SS-x}\ [km/s] = 0.80416\ V_{p,wet,R-x} - 0.85588 \tag{73}$$

$$V_{s,wet,R,SH-x}\ [km/s] = 0.76969\ V_{p,wet,R-x} - 0.86735 \tag{74}$$

Then, the arithmetic and harmonic means of the sand-shale mixture could be obtained from Equations 75 and 76, respectively.

$$V_{s,wet,V-x}\ [km/s] = (1 - V_{shale,norm-x}) \cdot V_{s,wet,V,SS-x} + V_{shale,norm-x} \cdot V_{s,wet,V,SH-x} \tag{75}$$

$$V_{s,wet,R-x}\ [km/s] = \left(\frac{(1 - V_{shale,norm-x})}{V_{s,wet,R,SS-x}} + \frac{V_{shale,norm-x}}{V_{s,wet,R,SH-x}} \right)^{-1} \tag{76}$$

So that the Voigt and Reuss bounds for wet C_{44} could be calculated as shown in Equation 77 and 78, respectively.

$$C_{44,wet,V-x} = \rho_{wet-x} \cdot V^2_{s,wet,V-x} \tag{77}$$

$$C_{44,wet,R-x} = \rho_{wet-x} \cdot V^2_{s,wet,R-x} \tag{78}$$

4.4.8 The Poisson's Ratio and Weight Parameters Determination

We already obtained the Voigt and Reuss bounds for both wet V_p (Equations 69 and 70) and wet V_s (Equations 75 and 76). Similarly as shown in Equation 20, the Voigt and Reuss bounds for the wet Poisson's ratio (ν_{wet}) then can be calculated by using Equations 79 and 80, respectively.

$$\nu_{wet,V-x} = \frac{1}{2}\left(\frac{\left(\frac{V_{p,wet,V-x}}{V_{s,wet,V-x}}\right)^2 - 2}{\left(\frac{V_{p,wet,V-x}}{V_{s,wet,V-x}}\right)^2 - 1}\right) \tag{79}$$

$$\nu_{wet,R-x} = \frac{1}{2}\left(\frac{\left(\frac{V_{p,wet,R-x}}{V_{s,wet,R-x}}\right)^2 - 2}{\left(\frac{V_{p,wet,R-x}}{V_{s,wet,R-x}}\right)^2 - 1}\right) \tag{80}$$

To predict the wet Poisson's ratio model between the previously obtained Voigt-Reuss bounds values, we need to include the total porosity and critical porosity, as shown in Equation 81.

$$\nu_{pred-x} = \left(\frac{\phi_{total-x}}{\phi_{c-x}}\right)^{1-\phi_{total-x}} \nu_{wet,R-x} + \left(1 - \frac{\phi_{total-x}}{\phi_{c-x}}\right)^{1-\phi_{total-x}} \nu_{wet,V-x} \tag{81}$$

Where the ϕ_{c-x} is the critical porosity for either model 1 (Equation 48) or model 2 (Equation 49); $\phi_{total-x}$ is slightly adjusted total porosity equation as previously discussed in Equation 14, so that the model 1 uses Equation 82 while the model 2 uses Equation 83.

$$\phi_{total-1} = \phi_D + V_{cl-1} \cdot \phi_{N.dry-cl} \tag{82}$$

$$\phi_{total-2} = \phi_D + V_{cl-2} \cdot \phi_{N.dry-cl} \tag{83}$$

Where the non-normalized clay volume fraction for model 1 is the bulk clay volume ($V_{cl-1} = V_{clay}$), while for model 2 is the dry clay volume ($V_{cl-2} = V_{dry-clay}$).

The predicted Poisson's ratio simulates the stress sensitivity within the proposed methodology since the stress sensitivity affects the porosity and elastic modulus (Han, 1986; Dong et al., 2010; MacBeth, 2004), where these parameters are related to one of the parameters from the Poisson's ratio itself; elastic velocities. Equation 81 shows that we need to use the ratio between total porosity and the critical porosity. For consolidated rock, the total porosity would be smaller (closer to 0), making the ratio closer to 0; hence,

the predicted Poisson's ratio is represented by its Voigt bound. For unconsolidated rock, the total porosity would close to the critical porosity so that the porosity ratio will be 1; hence, the Poisson's ratio represents by its Reuss bound.

By including the obtained predicted wet Poisson's ratio (Equation 81) and the Reuss wet Poisson's ratio (80), then the weight parameter (W) for the bounding average method could be calculated. The weight parameters for estimating C_{33} and C_{44} are respectively shown in Equations 84 and 85.

$$W_{C_{33}-x} = 1 - \frac{\nu_{pred-x}}{\nu_{wet,R-x}} \exp\left[-(1-(V_{cl-x}+\phi_{input-x}))\left(\frac{\sigma'}{\sigma_{max-x}}\right)^{\frac{1}{3}}\right] \tag{84}$$

$$W_{C_{44}-x} = 1 - \frac{\nu_{pred-x}}{\nu_{wet,R-x}} \exp\left[-(1-(V_{cl-x}+\phi_{input-x}))\left[\left(\frac{1+2\,K'_o}{3}\right)\left(\frac{\sigma'}{\sigma_{max-x}}\right)\right]^{\frac{1}{3}}\right] \tag{85}$$

Where σ' is the effective stress (Equation 45); σ_{max} is the maximum overburden stress (Table 25); K'_o is the horizontal-to-vertical effective stress, with value of 0.85 for depth less than 4 km, or 0.95 for more than 4 km (Grauls, 1997); and ϕ_{input} is the effective porosity (Equation 10) for model 1, or total porosity (Equation 83) for model 2.

4.4.9 The Bounding Average Method

After the weight parameters are obtained, we could perform the bounding average method (BAM) to predict the two stiffness coefficients. As previously mentioned in the theory chapter (Equation 3), then the BAM mechanism for predicting C_{33} and C_{44} are respectively shown in Equations 86 and 87.

$$C_{33,Pred-x} = C_{33,wet,R-x} + W_{C_{33-x}} \cdot [C_{33,wet,V-x} - C_{33,wet,R-x}] \tag{86}$$

$$C_{44,Pred-x} = C_{44,wet,R-x} + W_{C_{44-x}} \cdot [C_{44,wet,V-x} - C_{44,wet,R-x}] \tag{87}$$

For comparison of the predicted values, then the measured stiffness coefficients could be calculated by using Equations 88 and 89, in that order.

$$C_{33,Meas} = (V_{p,Meas})^2 \cdot \rho_b \tag{88}$$

$$C_{44,Meas} = (V_{s,Meas})^2 \cdot \rho_b \tag{89}$$

Where $V_{p,Meas}$ and $V_{s,Meas}$ are the measured P-wave and S-wave velocities from the sonic logs (Equations 25 and 26); ρ_b is the bulk density log. Finally, the vertically-propagating elastic velocity prediction for both P-wave and S-wave could be executed by respectively using Equations 90 and 91.

$$V_{p,Pred-x} = \sqrt{\frac{C_{33,Pred-x}}{\rho_{wet-x}}} \tag{90}$$

$$V_{s,Pred-x} = \sqrt{\frac{C_{44,Pred-x}}{\rho_{wet-x}}} \tag{91}$$

4.5 Fitness Observation

The primary purpose of this last step is to assess the fitness or quality of our velocity prediction to the measured velocity (Figure 26). We use two different quantification parameters, namely the coefficient correlation (R) and error percentage. The coefficient correlation describes the trend similarity between the measured and predicted velocity, while the error percentage describes the value discrepancy between the two. Ideally, the best prediction would have the coefficient correlation close to 1 and the error percentage close to 0%.

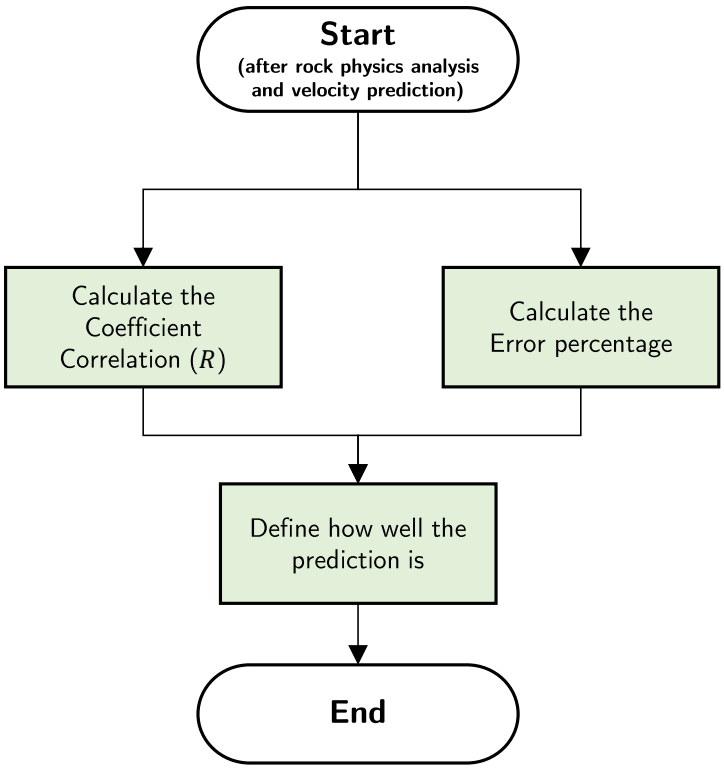

Figure 26: Flowchart for the substeps in the fitness observation step.

4.5.1 Correlation Coefficient

The Pearson's correlation coefficient (R) is a statistical quantification parameter that measures the trend resemblance between two different sets of data, or in our case, the measured and predicted velocities. The coefficient correlation could be obtained from the following equation.

$$R = \frac{\Sigma(X_i - \bar{X})(Y_i - \bar{Y})}{\sqrt{\Sigma(X_i - \bar{X})^2 \Sigma(Y_i - \bar{Y})^2}} \tag{92}$$

Where X and Y are respetively the measured and predicted velocity values, each having n values $X_1, X_2, X_3, ..., X_n$ and $Y_1, Y_2, Y_3, ..., Y_n$, respectively; $\bar{X}$ and $\bar{Y}$ are respetively the mean of X and Y. The summation continues across all n possible values of X and Y, or in our case, from the depth of seafloor until the total depth (TD) point, depth intervals that has no neutron porosity log, or depth intervals that has neutron porosity log. Schober and Schwarte (2018) provide several interpretations for the obtained R as shown in Table 19, ranging from negligible to very strong correlation.

Table 19: Several interpretations based on the range of correlation coefficient values. (Provided by Schober and Schwarte, 2018).

Correlation Coefficient (R)	**Interpretation**
0.00 - 0.10	Negligible correlation
0.10 - 0.39	Weak correlation
0.40 - 0.69	Moderate correlation
0.70 - 0.89	Strong correlation
0.90 - 1.00	Very strong correlation

Based on that table, then practically, our velocity prediction is justifiable if the correlation coefficient value is at least 0.70 (strong correlation). In the MATLAB environment, this R calculation is done using a built-in function called *corrcoef*, in which this procedure is applied for the study.

4.5.2 Error Percentage

The error percentage is a quantification parameter based on the relative value deviation between the measured and predicted velocity. This parameter is inspired by Han (1986), in which he uses this relative deviation for his shaly sand velocity prediction (Equations 93 and 94). If the relative deviation value is less than 1, then the prediction is underestimating the measured velocity. Conversely, if the value is more than 1, then the prediction is overestimating the measured velocity. Ideally, the best prediction would make the relative deviation into a value that closes to 1.

$$s_{V_p} = \frac{V_{p,Pred-x}}{V_{p,Meas}} \tag{93}$$

$$s_{V_s} = \frac{V_{s,Pred-x}}{V_{s,Meas}} \tag{94}$$

Afterward, the error percentages for V_p and V_s predictions could be respectively calculated by using Equations 95 and 96.

$$Error_{V_p}[\%] = \frac{\left|1 - s_{V_p}\right|}{1} \cdot 100 \tag{95}$$

$$Error_{V_s}[\%] = \frac{\left|1 - s_{V_s}\right|}{1} \cdot 100 \tag{96}$$

Where the absolute difference calculation between 1 and the relative deviation is there to equalize both overestimating and underestimating conditions. Since the expected best relative deviation is 1, then the best error percentage should be 0%.

5 Results

5.1 The Logs Before and After Extrapolation

The following figures in this subchapter show the logs before and after extrapolation to the seafloor for the three wells in the study. The pre and post extrapolated logs for Well 34/7-1 could be respectively observed in Figures 27 and 28. Only one log is available in all depth intervals: The Gamma-ray (GR) log. The bit size log is not an actual log; it is estimated from the information provided by the final well report. It appears that the shallower part of the pre-extrapolated GR log (from the seafloor until approximately 450 meters) is having a different trend than the deeper part. However, it is noticed that there was a change of bit size on that shallower part; hence, we correct this interval by shifting it to the right, as seen on the post-extrapolated GR log. The measured V_p log could be estimated from the only available compressional sonic log, then extrapolated to the seafloor from approximately 450 meters depth. The predicted V_s log is obtained from the extrapolated V_p log by using Greenberg-Castagna's approach (Equations 53 to 56). This predicted V_s log is not an actual log since the shear sonic log is not available for this well. The missing bulk density (ρ_b) log in the shallower interval is estimated from the extrapolated V_p log using Gardner's approach (Equations 29 and 30), then the density porosity (ϕ_D) is obtained from the extrapolated ρ_b log, using Equation 8. The neutron porosity (ϕ_N) log is available between Shetland Group to TD.

The pre and post extrapolated logs for Well 6704/12-1 could be respectively observed in Figures 29 and 30. Several logs are available in all depth intervals: The Gamma-ray (GR) log, bit size, and V_p log (reciprocal to the compressional sonic log). Initially, the measured V_s log (driven from the shear sonic log) is only available for the deeper part. The shallower part of the V_s log is estimated from the available V_p log using Greenberg-Castagna's approach. The missing ρ_b logs in the shallower part are estimated from the V_p log by using Gardner's approach, knowing that the shallower interval consists of clay-rich siliceous ooze sediments (Table 5). The ϕ_D is obtained from the extrapolated ρ_b log, while the (ϕ_N) log is available between Middle Brygge Formation to TD. It is seen that the measured P-wave velocity (V_p) in the shallower part of this well has constant values around 1.5 km/s. These constant values might confirm the presence of siliceous ooze sediments, where Breitzke (2000) shows the typical V_p values of diatomaceous or siliceous ooze sediments to have similar values (Figure 15).

The pre and post extrapolated logs for Well 7220/8-1 could be respectively observed in Figures 31 and 32. There is not a single log that fully covers all of the depth intervals. The rest of the procedures are similar to the previous two wells. However, both Greenberg-Castagna's and Gardner's approaches are not implemented since the V_p log is not available in the shallower part. As a result, the missing V_s log and ρ_B log in the shallower part could not be estimated as well. Instead, the extrapolation is performed for these two logs. The ϕ_N log is available between the middle of the Sotbakken group to TD.

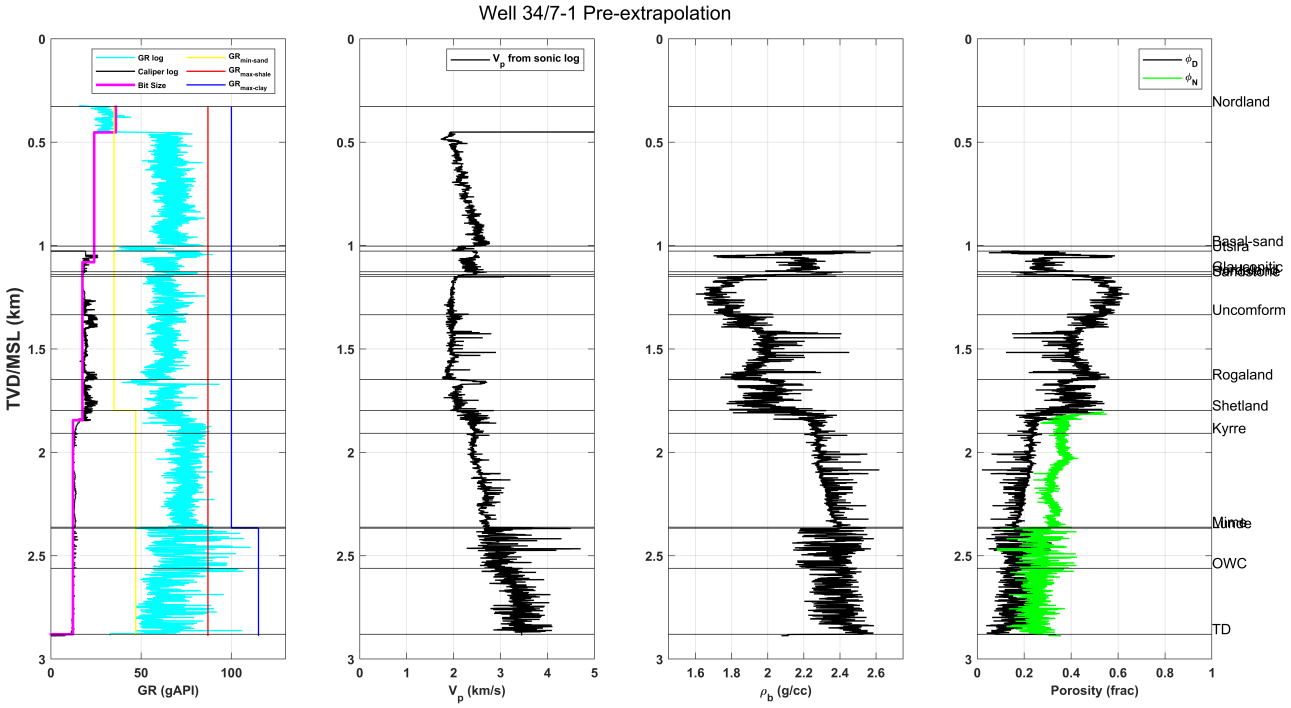

Figure 27: The pre-extrapolated logs of Well 34/7-1. From left to the right subfigures: Gamma Ray (GR) well panel, measured-velocity panel, bulk-density panel, and porosity panel.

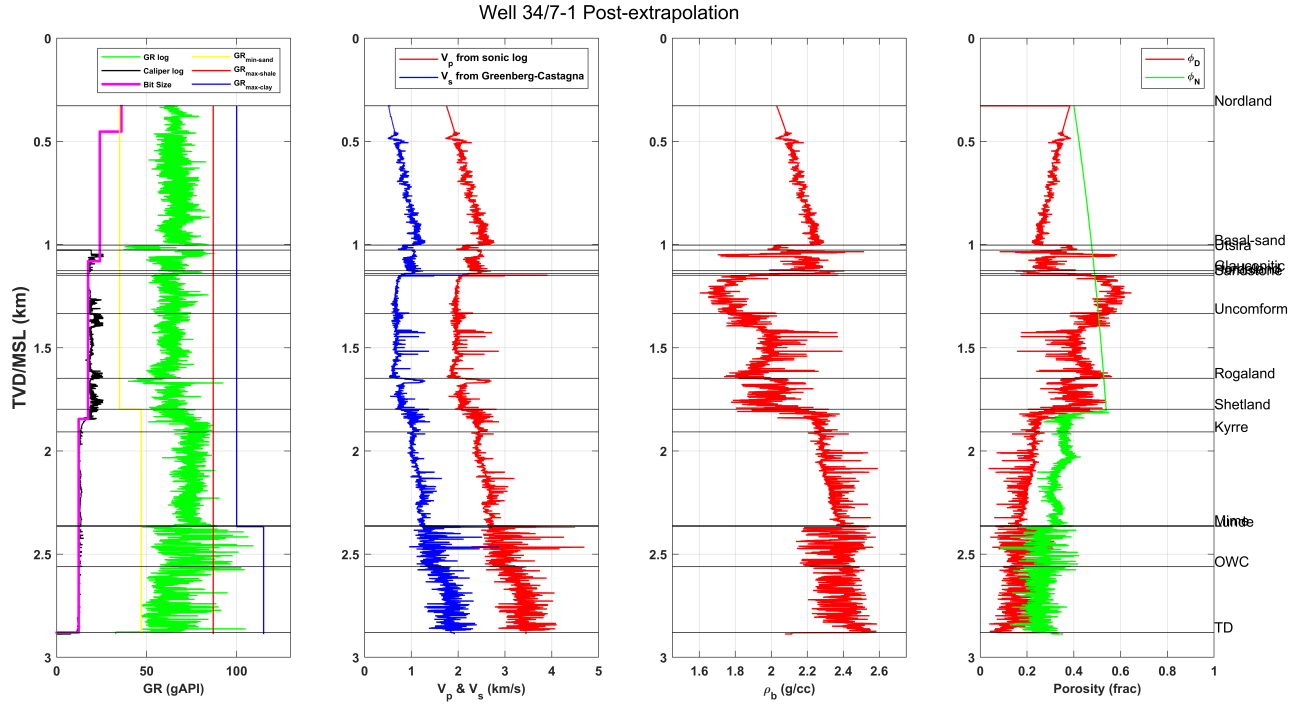

Figure 28: The post-extrapolated logs of Well 34/7-1. From left to the right subfigures: Gamma Ray (GR) well panel, measured-velocity panel, bulk-density panel, and porosity panel.

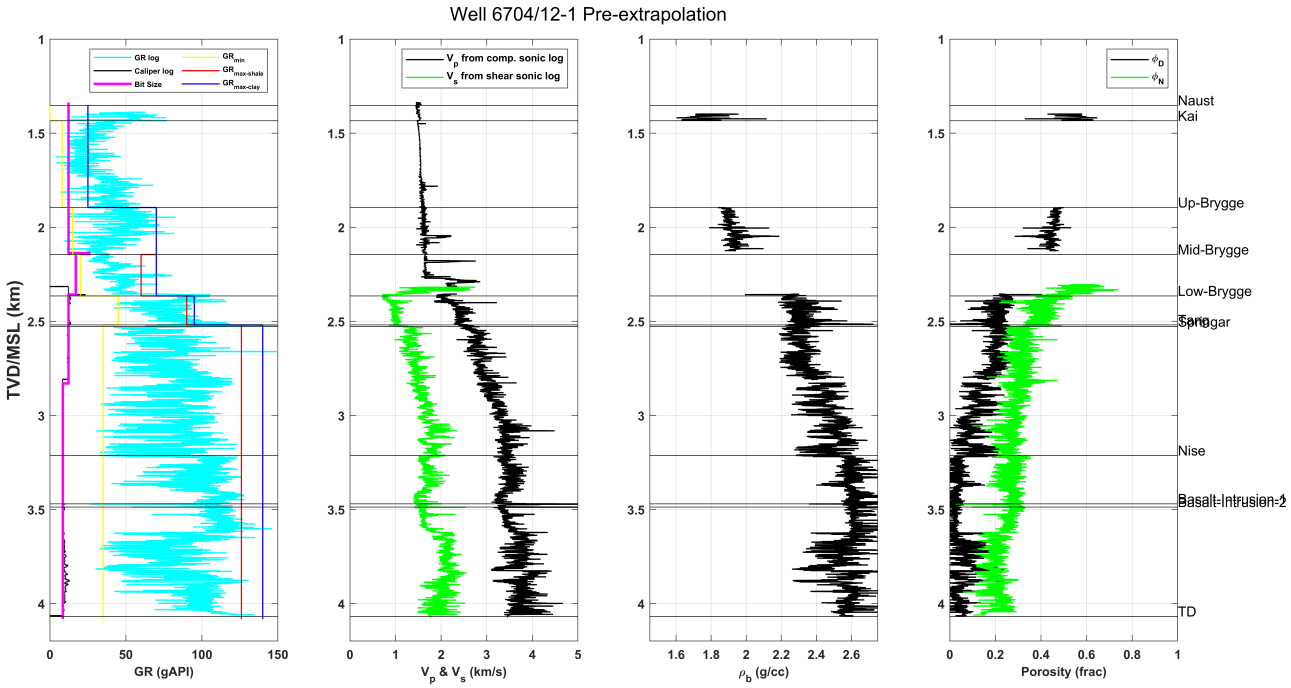

Figure 29: The pre-extrapolated logs of Well 6704/12-1. From left to the right subfigures: Gamma Ray (GR) well panel, measured-velocity panel, bulk-density panel, and porosity panel.

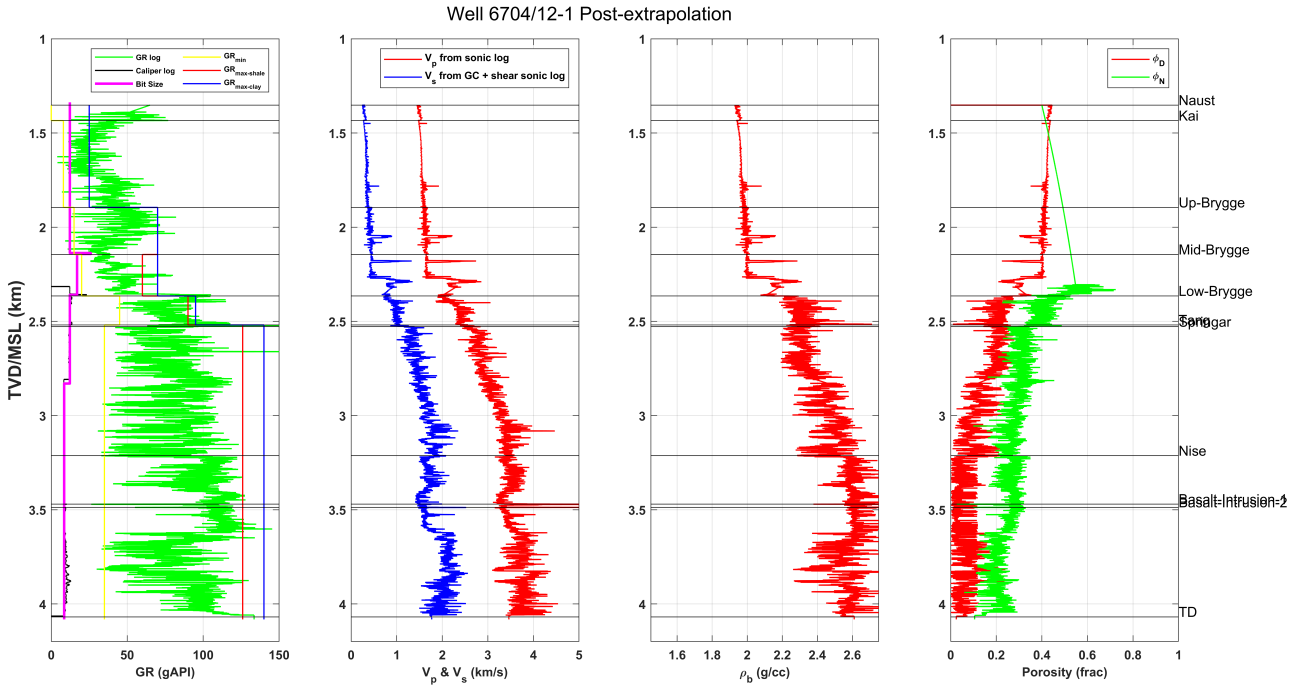

Figure 30: The post-extrapolated logs of Well 6704/12-1. From left to the right subfigures: Gamma Ray (GR) well panel, measured-velocity panel, bulk-density panel, and porosity panel.

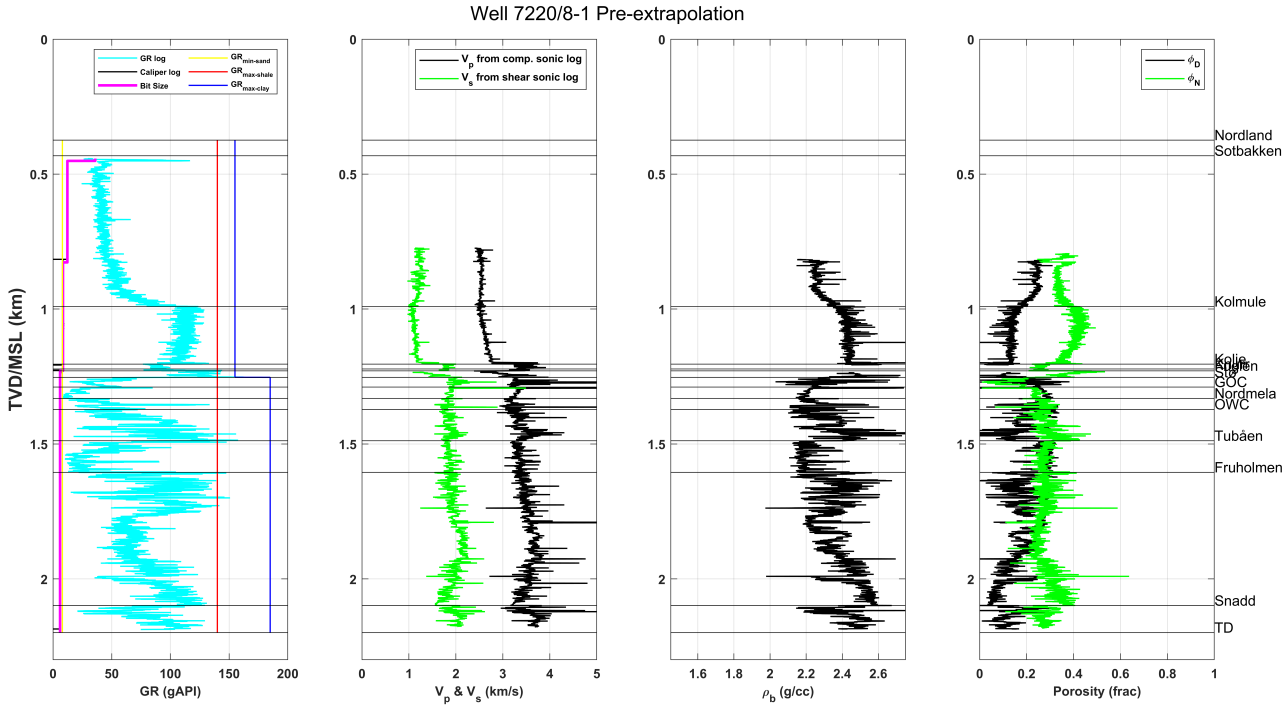

Figure 31: The pre-extrapolated logs of Well 7220/8-1. From left to the right subfigures: Gamma Ray (GR) well panel, measured-velocity panel, bulk-density panel, and porosity panel.

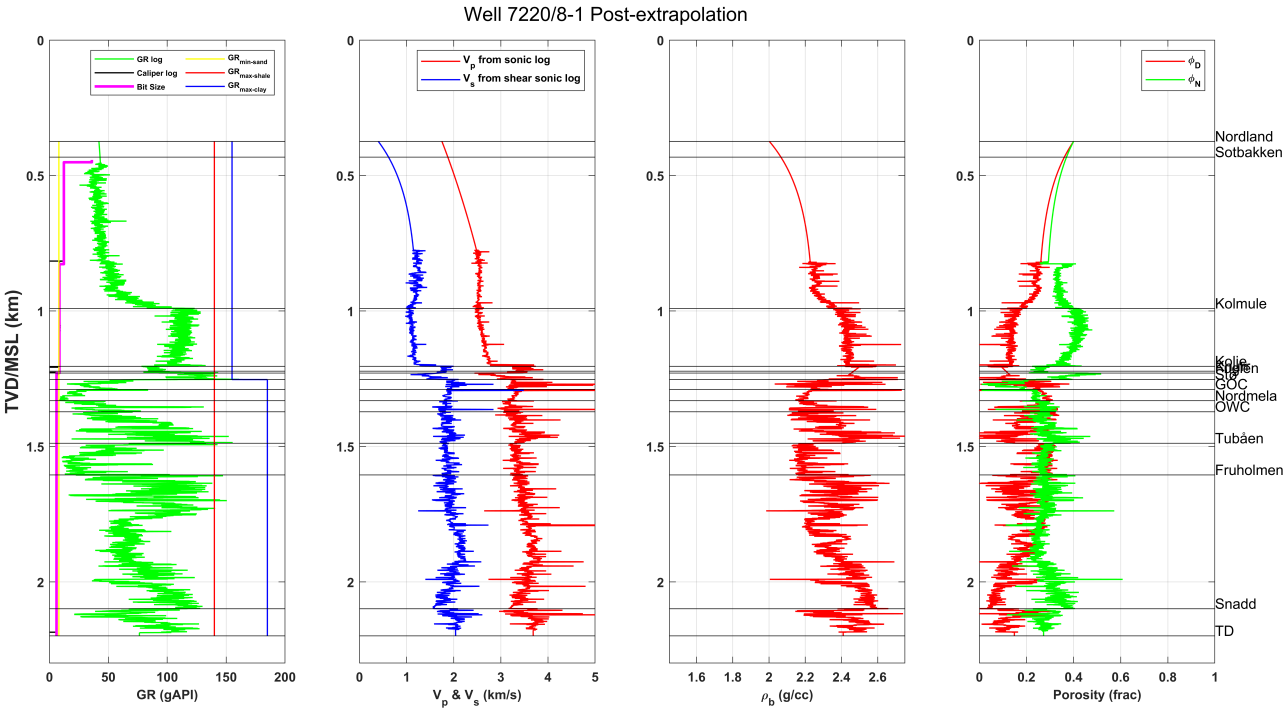

Figure 32: The post-extrapolated logs of Well 7220/8-1. From left to the right subfigures: Gamma Ray (GR) well panel, measured-velocity panel, bulk-density panel, and porosity panel.

5.2 The Temperature, Stress, and Saturation Profiles

The following figures in this subchapter are the temperature profiles (Figure 33, subfigures a to c), stress profiles (Figure 33, subfigures d to f), saturation profiles (Figure 34, subfigures a to c), and the estimated free-fluid's bulk modulus and density (Figure 34, subfigures d to f). These figures are respectively for Well 34/7-1, Well 6704/12-1, and Well 7220/8-1. The temperature and stress profiles are estimated based on the previously explained procedure in the Method Chapter (Respectively subchapters 4.4.1 and 4.4.2). The saturation profiles are based on several data or information as previously discussed in the Database Chapter (Chapter 3), while the free-fluid's bulk modulus and density estimation are based on the Batzle and Wang (1992) approach, as previously discussed in the Method Chapter (subchapter 4.4.6).

The temperature profiles consist of the estimated temperature trend along the depth (red curves), the bottom hole temperature or BHT (yellow dot), and the temperature data (black dots. **Appendix C** for Well 34/7-1, **Appendix D** for Well 6704/12-1, and **Appendix F** for Well 7220/8-1). Generally, The temperature profile seems to be overestimating the temperature data; however, the trends are quite acceptable since the maximum endpoint is relatively close to the BHT. The temperature profile for Well 6704/12-1 has the highest end value while Well 7220/8-1 has the lowest end value.

The stress profiles consist of the lithostatic stress (red curves), hydrostatic pressure (blue curves), differential or net stress (green curves), pore pressure (cyan curves), and the pore-pressure data (Black circles. **Appendix A** for Well 34/7-1, **Appendix D** for Well 6704/12-1, and **Appendix E** for Well 7220/8-1). As previously mentioned in the database chapter, a build-up pore pressure occurs in Well 34/7-1, so that the pore pressure is significantly higher than the hydrostatic pressure. Contrary to both Well 6704/12-1 and Well 7220/8-1, the pore pressure seems to be the same or slightly higher than the hydrostatic pressure. Based on Equation 45, when overpressure occurs, the pore pressure increases, making the differential stress decrease. Therefore, Well 34/7-1 has the least differential stress values than for the rest of the wells.

The saturation profiles consist of the gas saturation or S_g (green curves), oil saturation of S_o (red curves), and water saturation or S_w (blue curves). They are followed by the free fluids' profile, consisting of the bulk moduli profile on the left panel and the density profile on the right panel. The bulk moduli profiles are available for the non-patchy condition (K_{Reuss}) and patchy condition (K_{Voigt}). The saturation profile outside the reservoir is assumed to be fully water-saturated, while inside the reservoir could either be saturated by water, hydrocarbon, or both. If the hydrocarbon is present, then the mixing between water and hydrocarbon is assumed to be non-patchy.

Well 34/7-1 is an oil well, in which the oil saturation data are provided from the Conventional Core Analysis worksheet in its final well report (**Appendix B**). Well 6704/12-1 is a dry well; hence, the profile saturation along the well is fully water-saturated. Well 7220/8-1 is an oil-gas well, in which the hydrocarbon saturation values for both oil and gas are 81%, based on Hansen (2019).

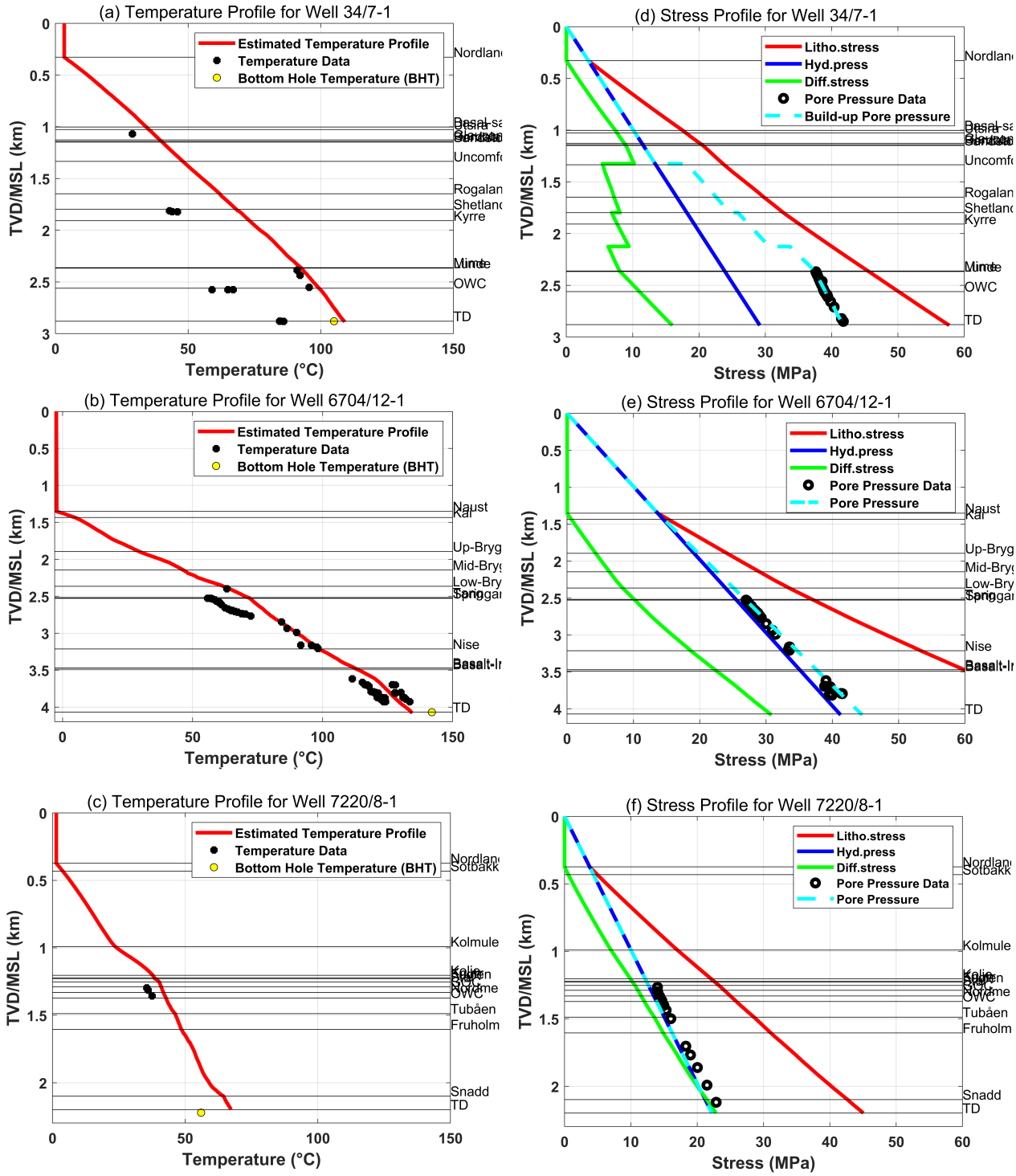

Figure 33: The temperature and stress profiles for Well 34/7-1 (respectively, subfigures a and d), Well 6704/12-1 (respectively, subfigures b and e), and Well 7220/8-1 (respectively, subfigures c and f).

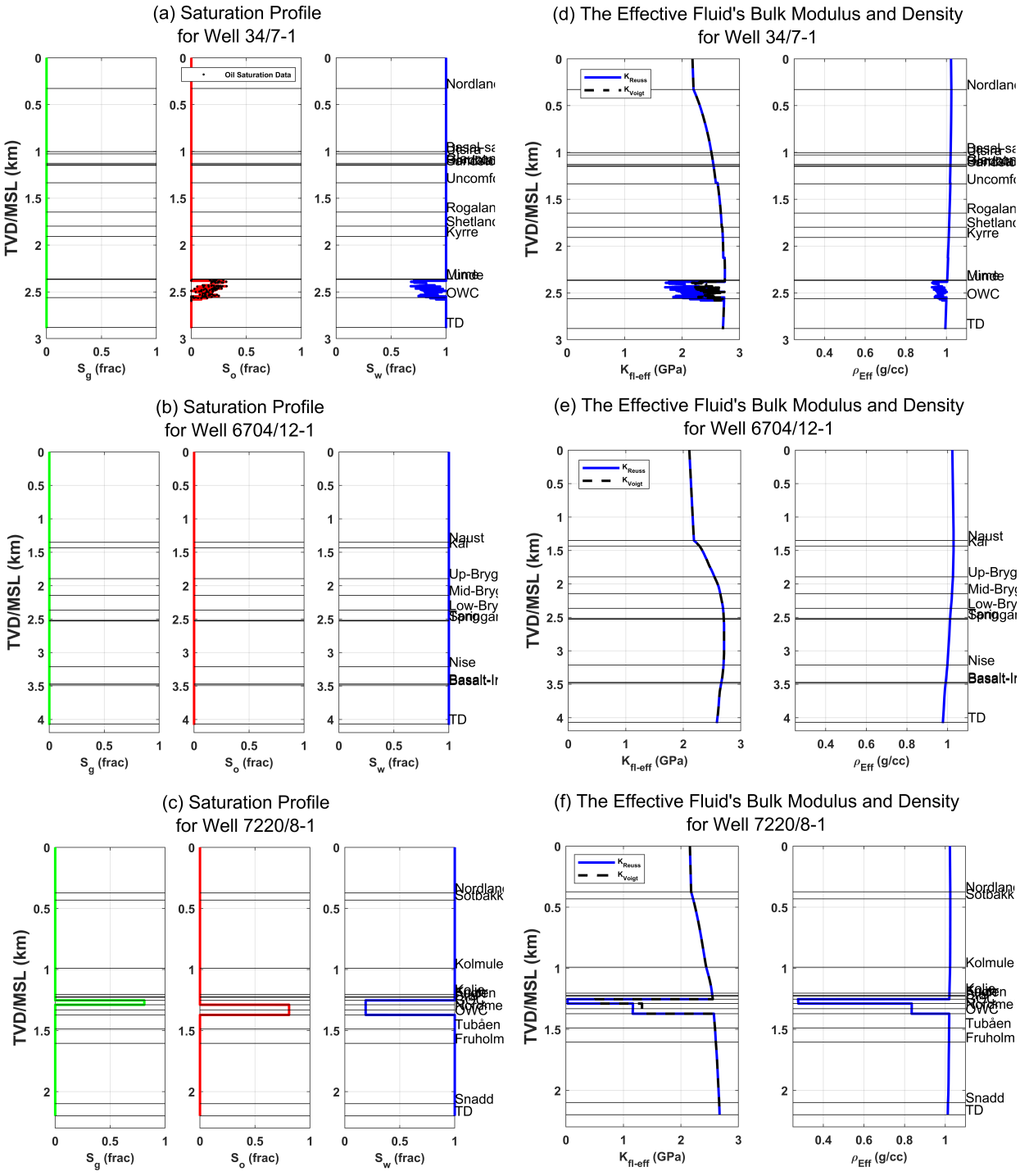

Figure 34: The saturation profiles for Well 34/7-1, Well 6704/12-1, and Well 7220/8-1 (respectively, subfigures a, b, and c). The bulk modulus and density of effective fluid from the Batzle and Wang approach, for Well 34/7-1, Well 6704/12-1, and Well 7220/8-1 (respectively, subfigures d, e, and f). The fluid mixing is assumed to be in a non-patchy condition; hence, we use the K_{Reuss} for the effective or free fluid's bulk modulus.

5.3 The Lithological Volume Fractions

The following figures in this subchapter are the lithological volume fractions for both Model 1 (Implicit Clay-Bound Water) and Model 2 (Explicit Clay-Bound Water), for Well 34/7-1 (respectively Figures 35 and 36), Well 6704/12-1 (respectively Figures 37 and 38), and Well 7220/8-1 (respectively Figures 39 and 40). The lithological volume fractions of Model 1 consist of normalized shale volumes (green curves), normalized bulk-clay volumes (blue curves), normalized silt volumes (black curves), and normalized sand volumes (yellow curves). There are some slight differences for Model 2; the blue curves represent the normalized dry-clay volumes, and the cyan curves represent the clay-bound water volumes. The normalization process of the lithological volume is already discussed in the substeps of the Petrophysical Analysis Step (Subchapters 4.3.3 and 4.3.4). It is seen from the figures that the summation between the dry-clay volume and clay-bound water volume in Model 2 is equal to the bulk-clay volume in Model 1.

For Well 34/7-1, it is seen that there are two distinct trends in the well, particularly in the shallower depth interval (Between the well markers of Nordland Group and Lunde Formation) and deeper depth interval (Between the well markers of Lunde Formation to TD). The sand and bulk-clay mixing in the shallower and deeper depth interval are respectively in the range of 20 - 60% and 0 - 80%; hence, the mixing in the deeper interval is more varying. The clay-bound water volume follows the same trend as the sand-clay mixing, with a range of 10 - 30% in the shallower interval and 0 - 20% in the deeper interval. The silt volume shows two trends in the shallower interval (Between the well markers of Nordland Group to Shetland Group) and deeper interval (Between the well markers of Nordland Group to TD). The silt volumes in the shallower and deeper depth interval range from 10 - 20% and 0 - 60%, respectively.

For Well 6704/12-1, the two distinct trends are seen in the shallower interval (Between the well markers of Naust to Lower Brygge Formations) and deeper interval (Between the well markers of Lower Brygge Formation to TD). As previously discussed in subchapter 4.3.2, the normalized sand volume for this well consists of the combination of ooze and sand volume (or ooze-sand volume) in the shallower part of the well (brown curves) and sand volume in the deeper part of the well (yellow curves). The mixing between ooze-sand and bulk-clay in the shallower part of the well range from 0 - 100%. On the contrary, sand and bulk-clay mixing in the deeper part of the well ranges from 10 - 85%. The clay-bound water volume has a similar trend as the previously mentioned mixing volumes, with a percentage range of 0 - 30% and 0 - 20% for the shallower and deeper interval, respectively. The silt volume shows three distinct trends: in the shallower part (Between the well markers of Naust Formation to Middle Brygge Formations), the silt is not present, so that the value is 0%; in the middle part (in the Middle Brygge Formation), the silt is present in the form of silty clay, in range of 5 - 20%; in the deeper part (Between the well markers of Lower Brygge Formation to TD), the silt volume significantly increases to be in the range of 0 - 60%.

Similarly, for well 7220/8-1, the two trends are seen in the shallower interval (Between the well markers of Nordland Group to Kolje Formation) and deeper interval (Between the well markers of Kolje Formation to TD). The sand-clay mixing for the shallower and deeper intervals are respectively 20 - 80% and 0 - 80%. The clay-bound water volumes also follow the same trend, with a range of volume between 10 - 25% and 0 - 25% for the shallower interval and deeper interval, correspondingly. The silt volume consists of three trends, namely in the upper shallower interval (from the Nordland Group to approximately 800 meters depth), lower shallower interval (from the 800 meters depth to well marker of Kolje Formation), and deeper interval (Between the well markers of Kolje Formation to TD). The silt volume fractions for these three intervals are respectively around 5%, 0 - 20%, and 0 - 45%.

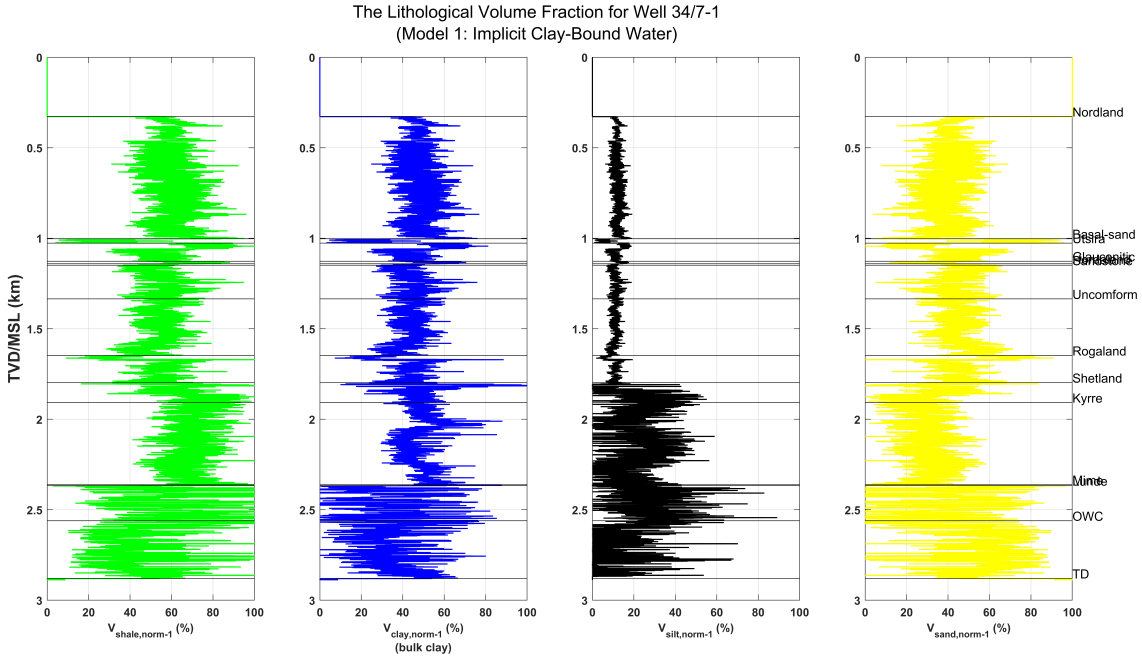

Figure 35: The lithological volume fraction for Model 1 (Implicit Clay-Bound Water Model) for Well 34/7-1. Green curves for the normalized shale volume, blue curves for the normalized bulk-clay volume, black curves for the normalized silt volume, and yellow curves for the normalized sand volume. The normalization is in respect to the density porosity (ϕ_D).

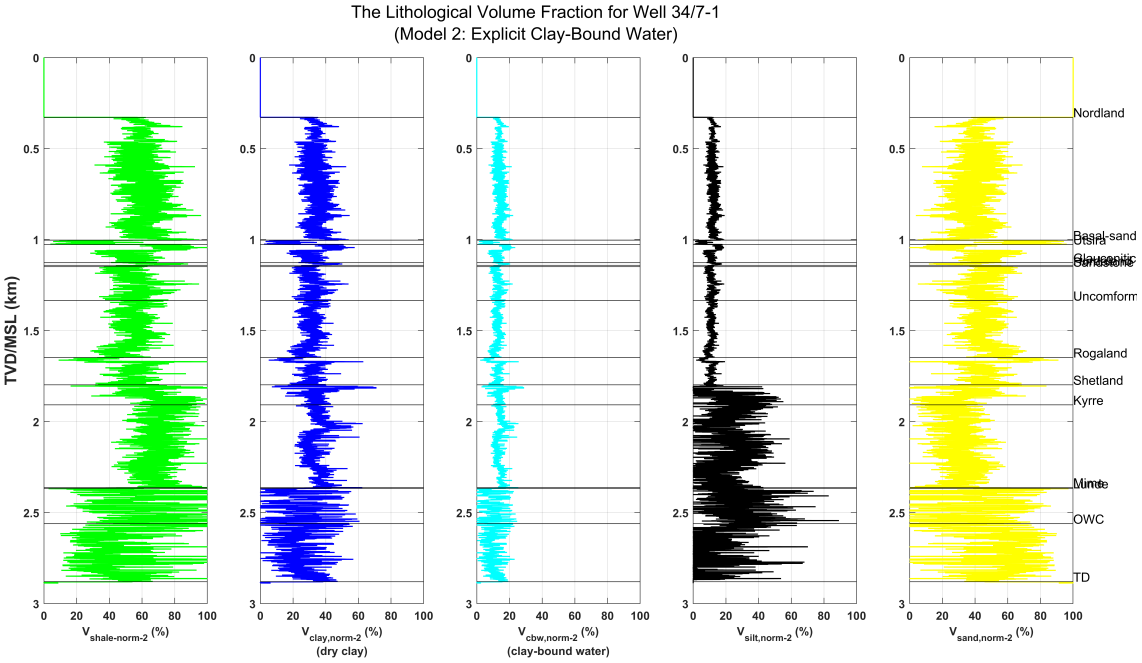

Figure 36: The lithological volume fraction for Model 2 (Explicit Clay-Bound Water Model) for Well 34/7-1. Green curves for the normalized shale volume, blue curves for the normalized dry-clay volume, cyan curves for the normalized clay-bound water volume, black curves for the normalized silt volume, and yellow curves for the normalized sand volume. The normalization is in respect to the density porosity (ϕ_D).

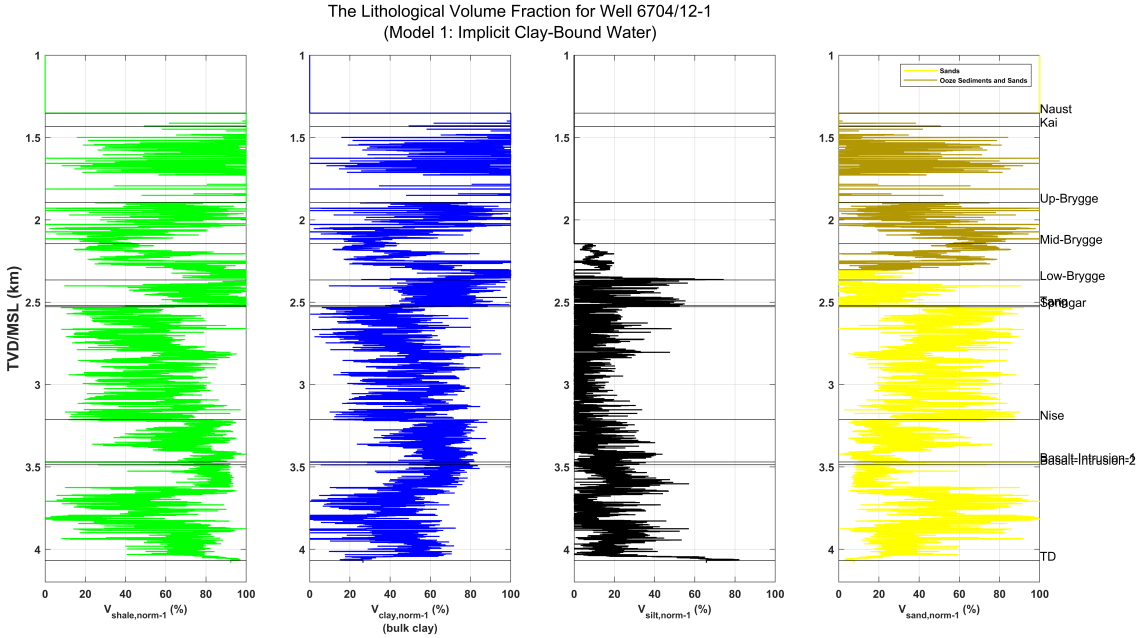

Figure 37: The lithological volume fraction for Model 1 (Implicit Clay-Bound Water Model) for Well 6704/12-1. Green curves for the normalized shale volume, blue curves for the normalized bulk-clay volume, black curves for the normalized silt volume, yellow curves for the normalized sand volume, and the brown curves for the normalized ooze-sand volume. The normalization is in respect to the density porosity (ϕ_D).

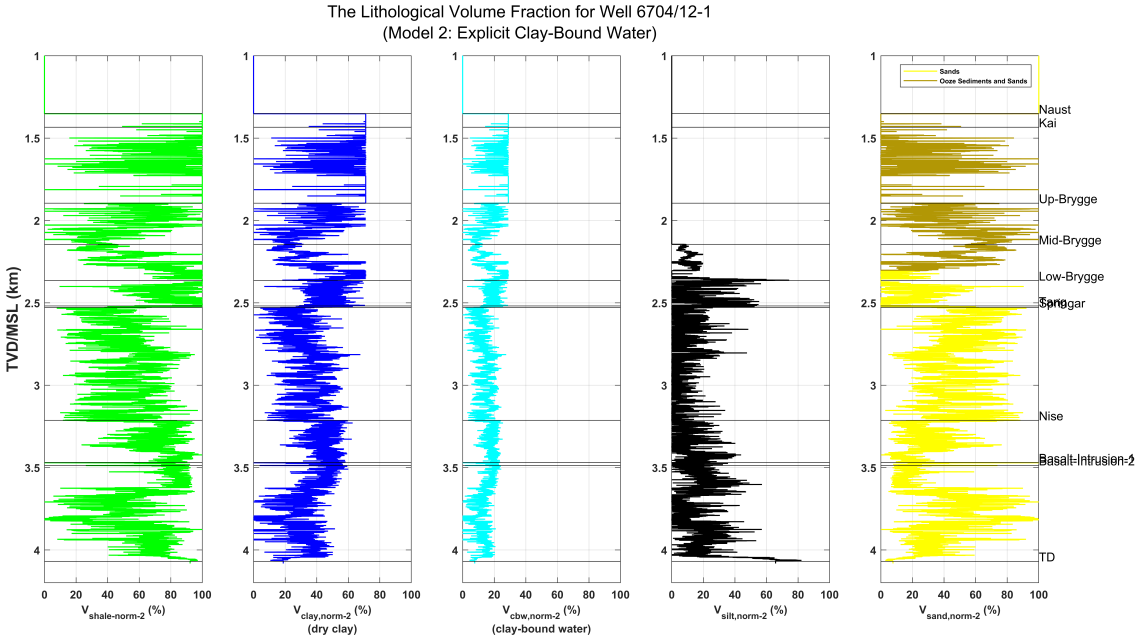

Figure 38: The lithological volume fraction for Model 2 (Explicit Clay-Bound Water Model) for Well 6704/12-1. Green curves for the normalized shale volume, blue curves for the normalized dry-clay volume, cyan curves for the normalized clay-bound water volume, black curves for the normalized silt volume, and yellow curves for the normalized sand volume, and the brown curves for the normalized ooze-sand volume. The normalization is in respect to the density porosity (ϕ_D).

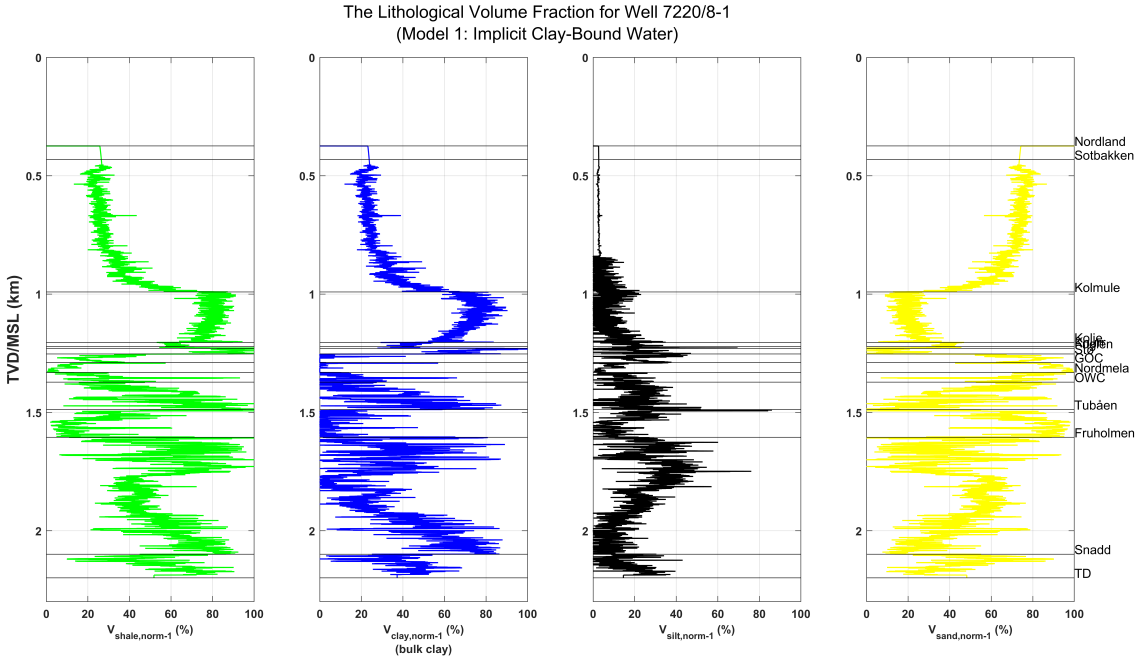

Figure 39: The lithological volume fraction for Model 1 (Implicit Clay-Bound Water Model) for Well 7220/8-1. Green curves for the normalized shale volume, blue curves for the normalized bulk-clay volume, black curves for the normalized silt volume, and yellow curves for the normalized sand volume. The normalization is in respect to the density porosity (ϕ_D).

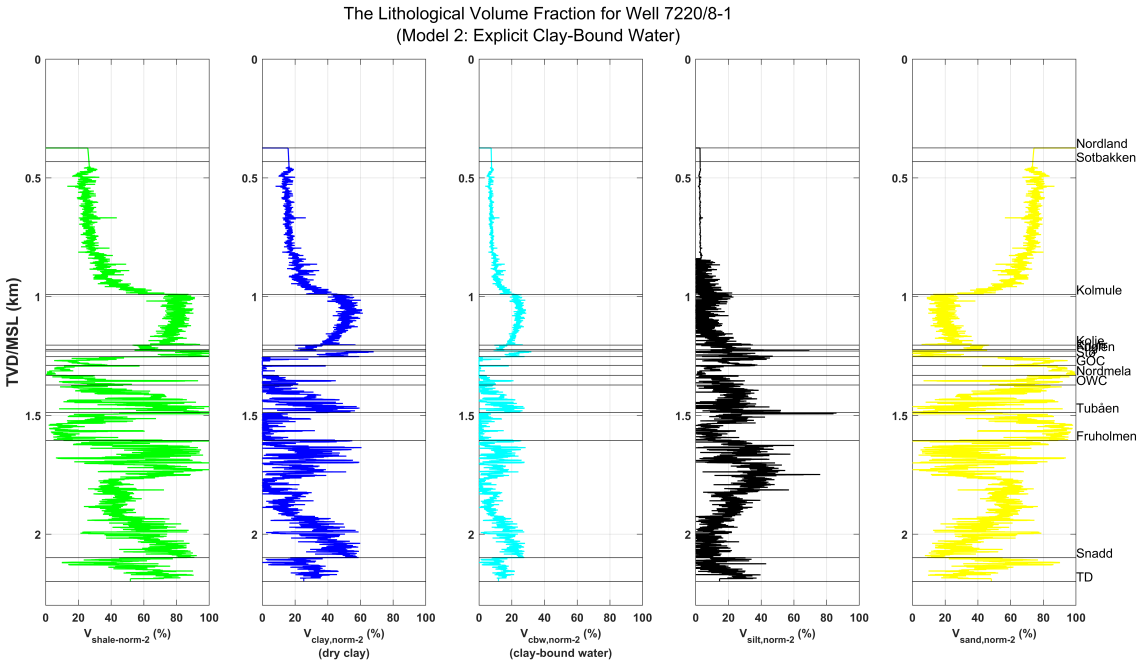

Figure 40: The lithological volume fraction for Model 2 (Explicit Clay-Bound Water Model) for Well 7220/8-1. Green curves for the normalized shale volume, blue curves for the normalized dry-clay volume, cyan curves for the normalized clay-bound water volume, black curves for the normalized silt volume, and yellow curves for the normalized sand volume. The normalization is in respect to the density porosity (ϕ_D).

5.4 The Critical Porosity (ϕ_c) and Horizontal-to-vertical Net Stress Ratio (K'_o)

The two figures in this subchapter are the estimated critical porosity trends (Figure 41) and the horizontal-to-vertical net stress ratio (K'_o) trends (Figure 42). The figure of the critical porosity consists of the trends respectively for models 1 and 2 for Well 34/7-1 (subfigures a and b), Well 6704/12-1 (subfigures c and d), and Well 7220/8-1 (subfigures e and f). The figure for K'_o consists of the trends for Well 34/7-1 (subfigure a), Well 6704/12-1 (subfigure b), and Well 7220/8-1 (subfigure c). The procedure of determining the critical porosity and K'_o is already discussed in the previous Chapters (Respectively subchapters 4.4.3 and 2.5).

Since the procedures are based on the lithological volume fractions from the previous subchapter, then the critical porosity trends for the three wells also consist of two trends in the shallower and deeper interval. The critical porosity in the shallower and deeper formation are respectively in the range of 0.5 to 0.7 and 0.4 to 0.7 for Well 34/7-1; 0.4 to 0.7 and 0.4 to 0.6 for Well 6704/12-1; and 0.5 to 0.7 and 0.4 to 0.7 for Well 7220/8-1. Even though the critical porosity trends for both models are visually similar, the critical porosity values for Model 2 are slightly smaller than for Model 1.

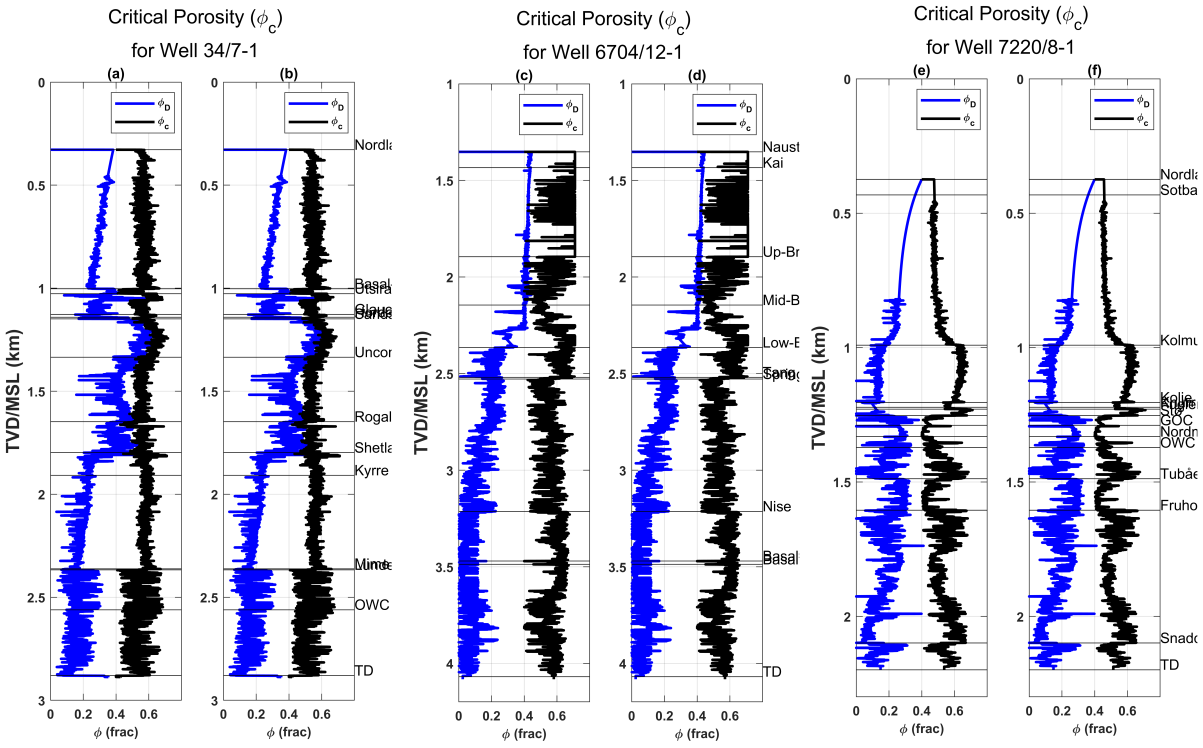

Figure 41: The critical porosity (ϕ_c) for the Implicit and Explicit Clay-Bound Water Model for Well 34/7-1 (Respectively, subfigures a and b), Well 6704/12-1 (Respectively, subfigures c and d), and Well 7220/8-1 (Respectively, subfigures e and f). The blue curves represent density porosity (ϕ_D), while the black curves represent ϕ_c.

The K'_o determination is based on Grauls (1997), where it is 0.85 before 4 km depth and 0.95 after 4 km. Since Well 7220/8-1 is the only well that reaches 4 km, it is the only well with two different trends of K'_o. The rest of the wells has a constant value of 0.85 for their respective K'_o trends.

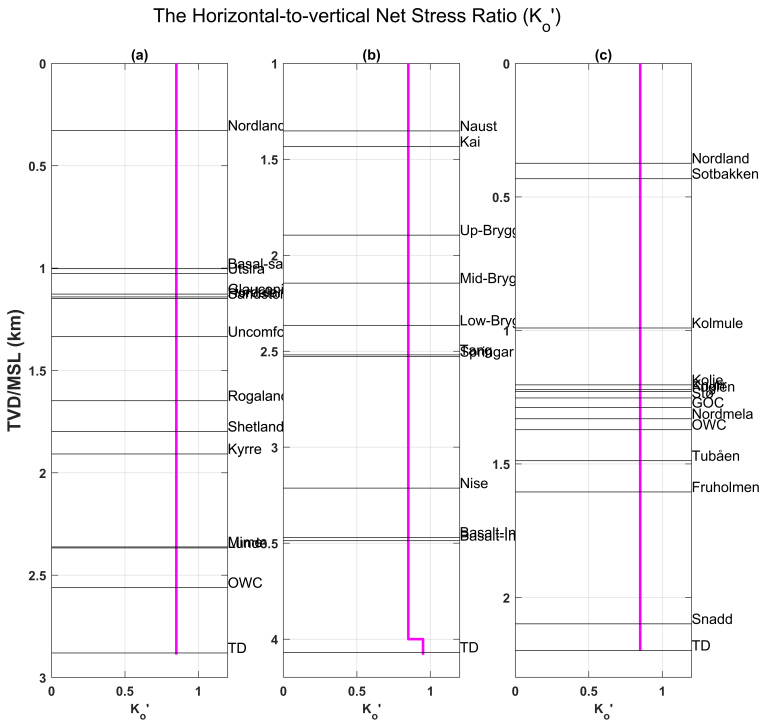

Figure 42: The horizontal-to-vertical Net Stress Ratio (K'_o) for (a) Well 34/7-1, (b) Well 6704/12-1, (c) and Well 7220/8-1.

5.5 The Voigt-Reuss Bounds for C_{33}, C_{44}, and Poisson's Ratio

The following figures in this subchapter are for the Voigt-Reuss Bounds for several rock-physics parameters for both Models 1 and 2, for Well 34/7-1 (Figures 43 and 44, respectively), Well 6704/12-1 (Figures 45 and 46, respectively), and Well 7220/8-1 (Figures 47 and 48, respectively).

Each of the figures consist of several subfigures from (a) to (h) for the Voigt-Reuss Bound of a specific rock-physics parameter: (a) Solid C_{33}, calculated by using Equations 58-59 for Model 1 or Equations 60-61 for Model 2; (b) Wet C_{33}, calculated by using Equations 65-66; (c) Solid density or ρ_{solid}, calculated by using Equation 67; (d) Wet density or ρ_{wet} compared to the bulk density or ρ_b; the Wet density is calculated by using Equation 68; (e) Wet P-wave velocity or $V_{p,wet}$, calculated by using Equations 69-70; (f) Wet S-wave velocity or $V_{s,wet}$, calculated by using Equations 75-76; (g) Wet C_{44}, calculated by using Equations 77-78; and (h) Poisson's ratio or ν, calculated by using Equations 79-80.

Some general observations for all the wells are: (1) the estimated Voigt-Reuss bounds for the solid C_{33} show a greater separation between the two bounds for Model 2; (2) the Reuss bound for the wet C_{33} of Model 2 is slightly smaller and has less variability than for the Model 1. The Voigt bounds for both models are pretty similar; (3) The estimated solid density for Model 2 is slightly smaller than the estimated solid density for Model 1. The estimated wet density trends for both models show an excellent fit to the bulk-density log. However, the wet density underpredicts the bulk density in the hydrocarbon-bearing interval. (4) The Voigt bounds for the wet velocities are quite alike for Models 1 and 2. However, the Reuss bounds for Model 2 are significantly smaller and have less value variation; (5) The Reuss bound for the Poisson's ratio is smaller and has less value variation for Model 2. From these observations, it is clear that the significant difference between both models is observed from their respective Reuss Bounds.

In terms of the values, most Voigt bounds represent the maximum values of a specific parameter, while the Reuss bounds represent the minimum values. However, it is the other way around for the Poisson's ratio, where the Voigt and Reuss bounds represent the minimum and maximum values, respectively.

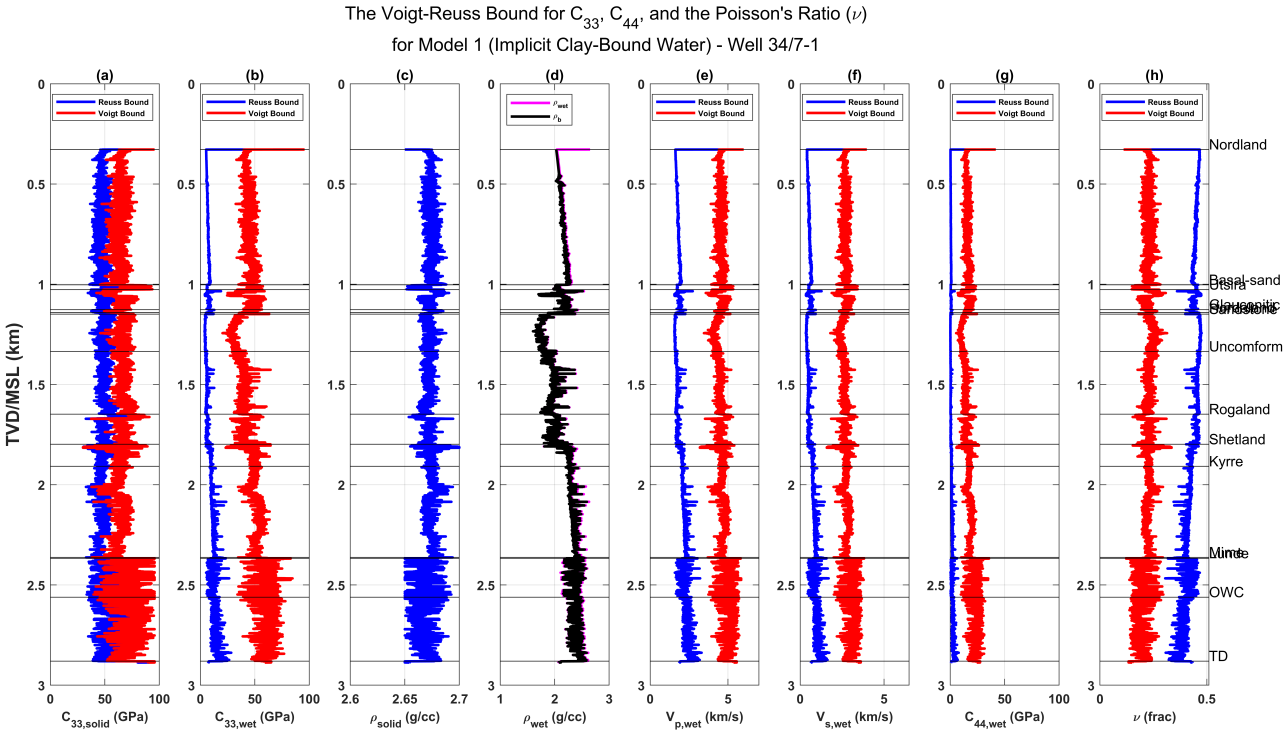

Figure 43: The Voigt-Reuss Bound for several rock-physics parameters for Model 1 (Implicit Clay-Bound Water), Well 34/7-1.

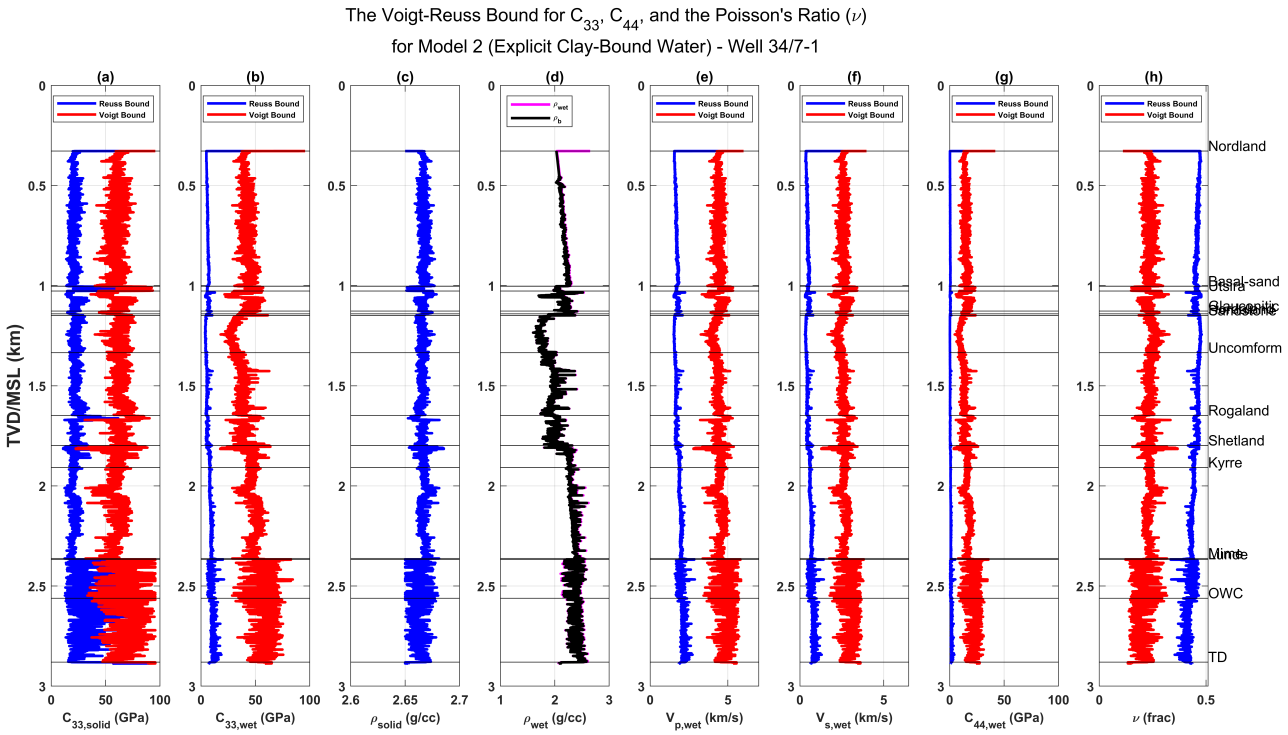

Figure 44: The Voigt-Reuss Bound for several rock-physics parameters for Model 2 (Explicit Clay-Bound Water), Well 34/7-1.

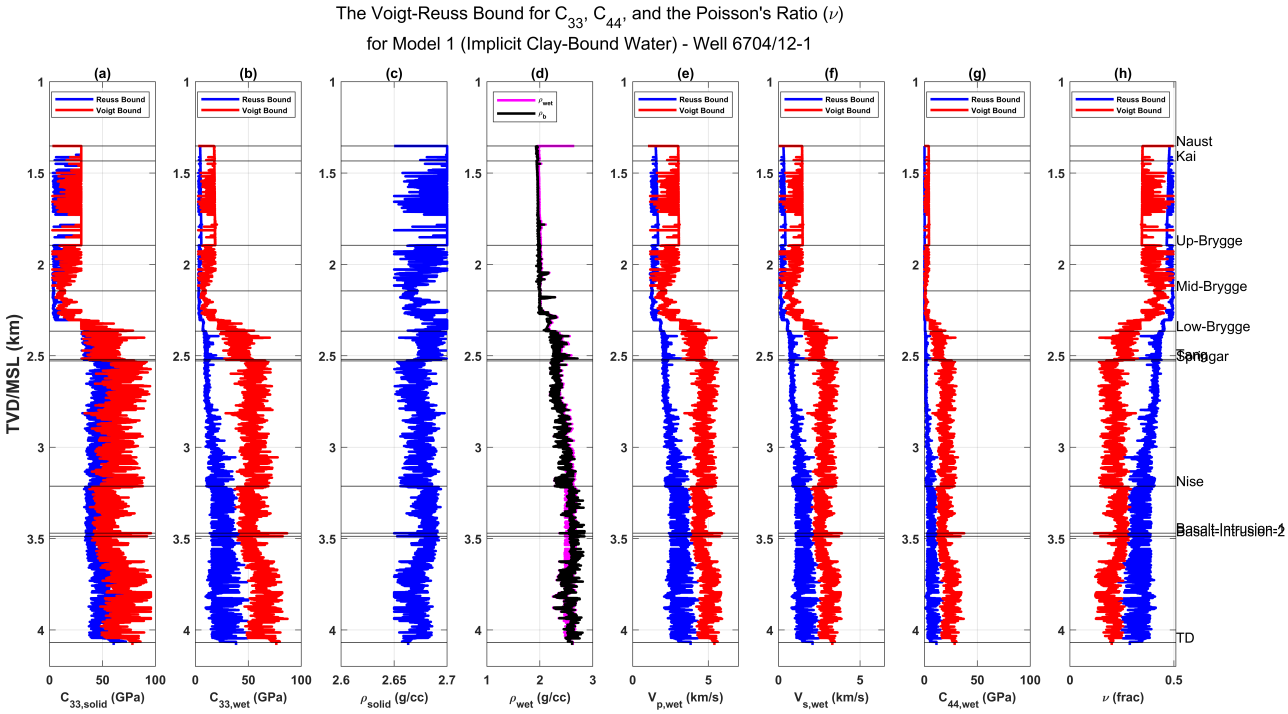

Figure 45: The Voigt-Reuss Bound for several rock-physics parameters for Model 1 (Implicit Clay-Bound Water), Well 6704/12-1.

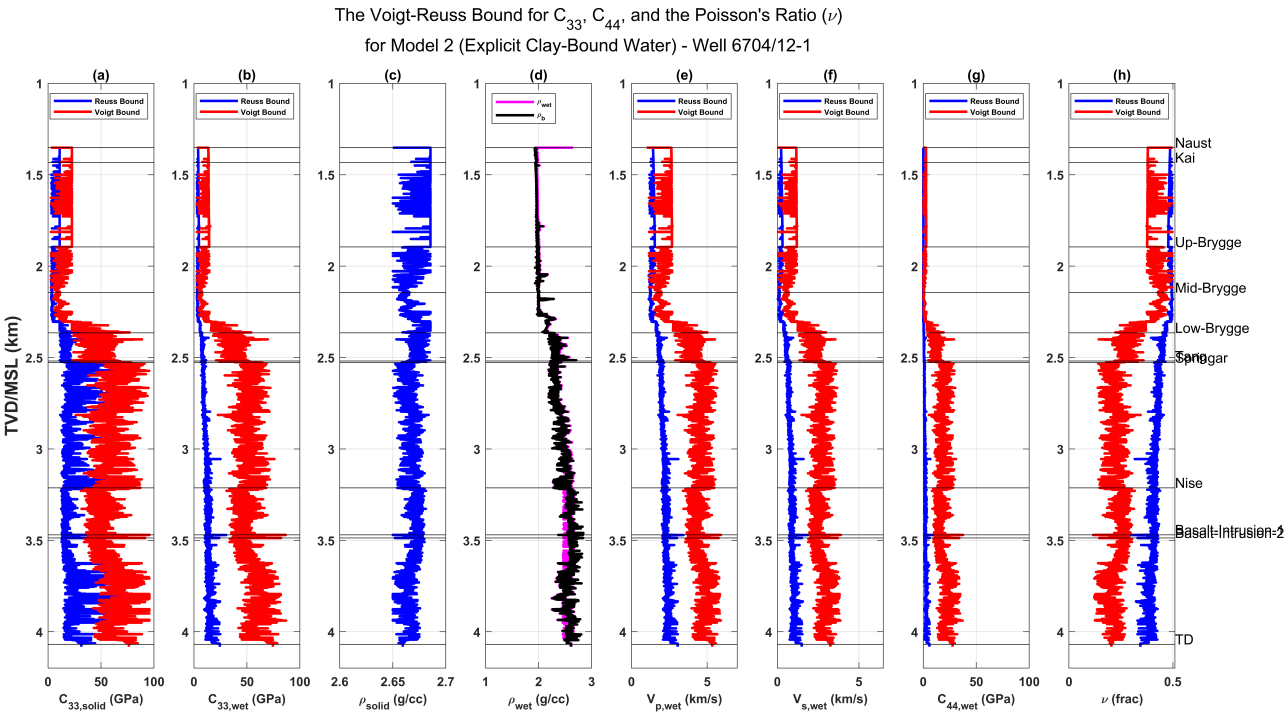

Figure 46: The Voigt-Reuss Bound for several rock-physics parameters for Model 2 (Explicit Clay-Bound Water), Well 6704/12-1.

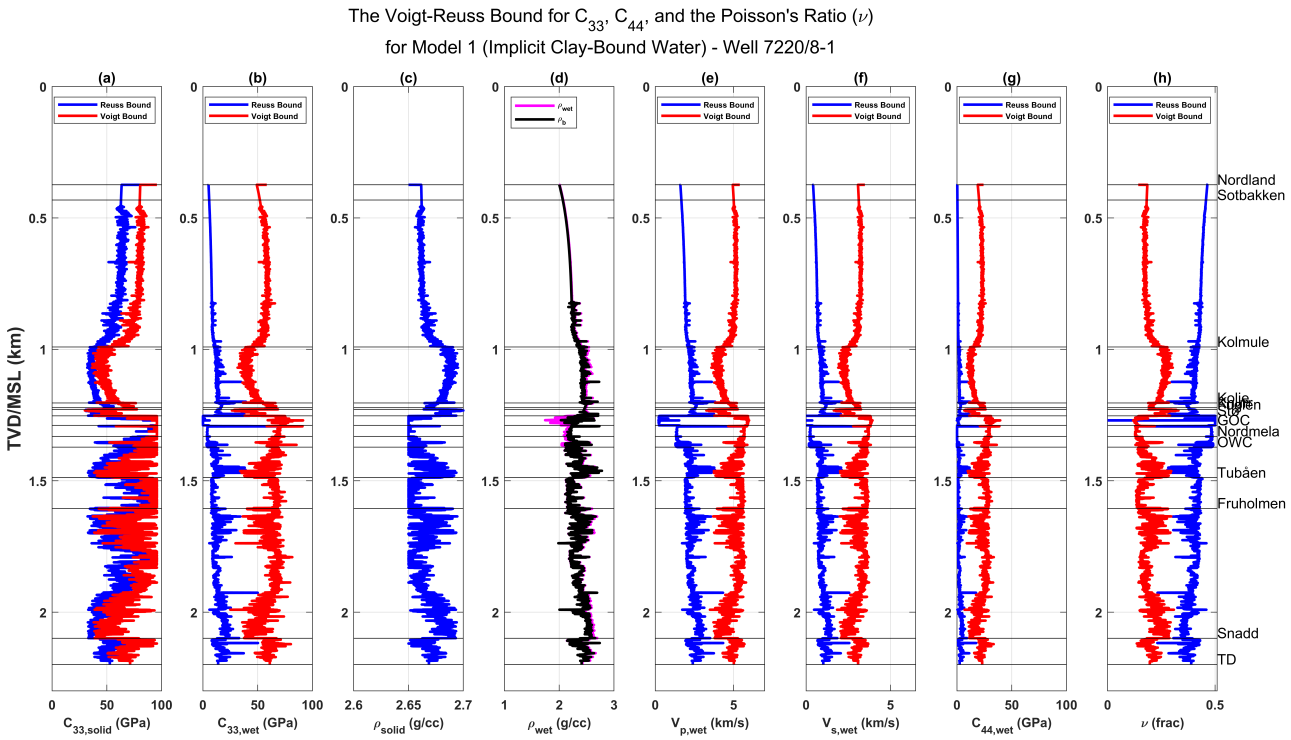

Figure 47: The Voigt-Reuss Bound for several rock-physics parameters for Model 1 (Implicit Clay-Bound Water), Well 7220/8-1.

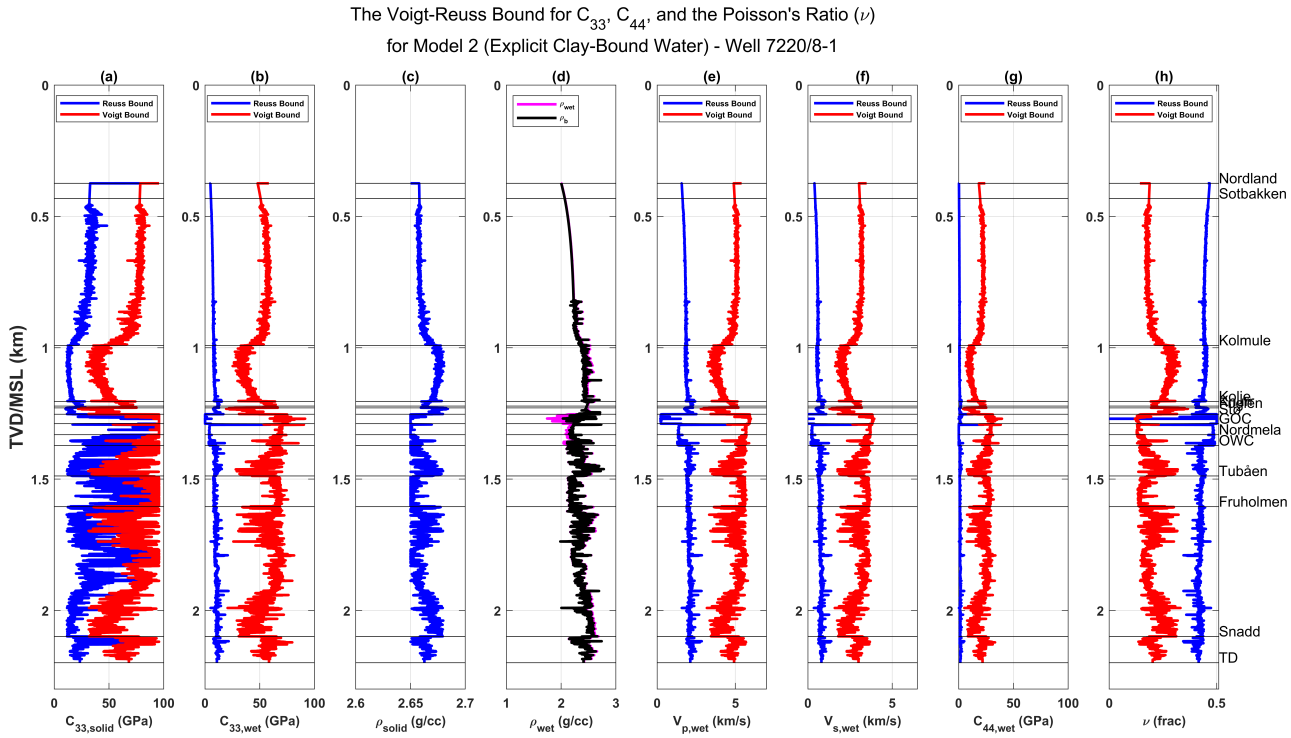

Figure 48: The Voigt-Reuss Bound for several rock-physics parameters for Model 2 (Explicit Clay-Bound Water), Well 7220/8-1.

5.6 The Predicted Poisson's Ratio and Weight Parameters

The following figures in this subchapter are for the predicted Poisson's ratio (ν_{pred}) and Weight Parameters, respectively for Models 1 and 2 of Well 34/7-1 (Figure 49), Well 6704/12-1 (Figure 50), and Well 7220/8-1 (Figure 51). In all of the figures, the subfigures (a) and (b) are for Model 1, while (c) and (d) for Model 2. The predicted Poisson's ratio are obtained from the Voigt-Reuss Bounds of the same parameter (Equation 81), while the weight parameters for the two stiffness coefficients (C_{33} and C_{44}) are respectively obtained by using Equations 84 and 85.

In general, the predicted Poisson's ratio trends for Model 1 tend to follow the Reuss Bound, while for Model 2 are slightly shifted to the Voigt Bound than that for Model 1, especially in the deeper depth intervals. The weight parameters for Model 2 are somewhat slightly higher than for Model 1. Since the value for K'_o is generally 0.85, then the weight parameters for the two stiffness coefficients are almost the same, with the range of weight parameters for Models 1 and 2, respectively: 0 to 0.5 and 0 to 0.55 for Well 34/7-1; 0 to 0.55 and 0 to 0.65 for Well 6704/12-1; and 0 to 0.75 and 0 to 1 for Well 7220/8-1.

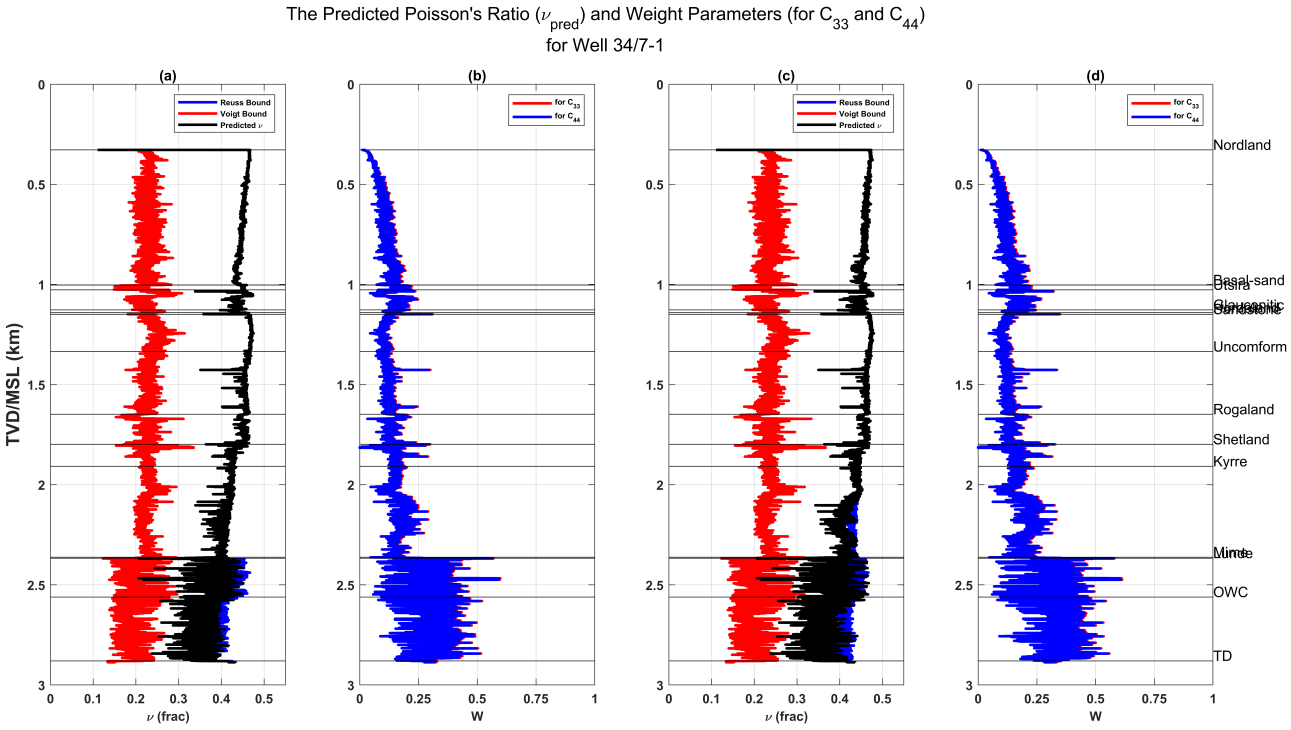

Figure 49: The predicted Poisson's ratio and weight parameters for Well 34/7-1. subfigures a and b for Model 1 (Implicit Clay-Bound Water), while subfigures c and d for Model 2 (Explicit Clay-Bound Water).

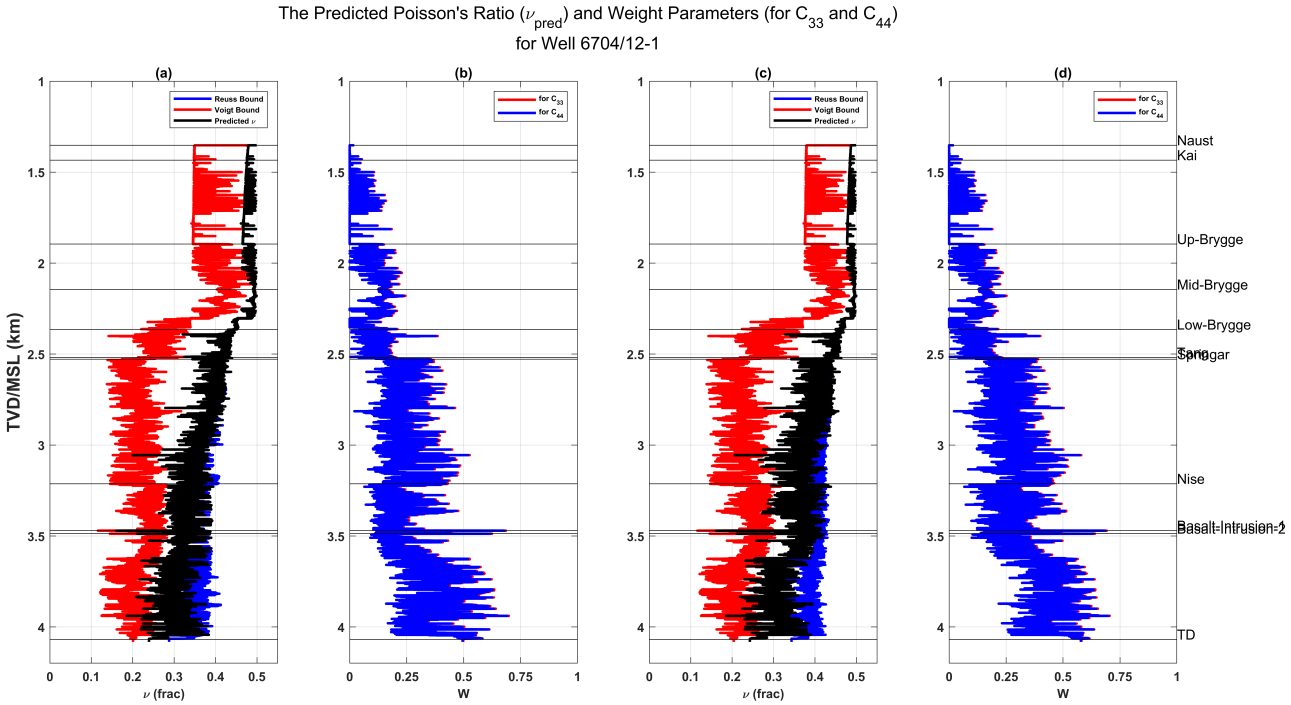

Figure 50: The predicted Poisson's ratio and weight parameters for Well 6704/12-1. subfigures a and b for Model 1 (Implicit Clay-Bound Water), while subfigures c and d for Model 2 (Explicit Clay-Bound Water).

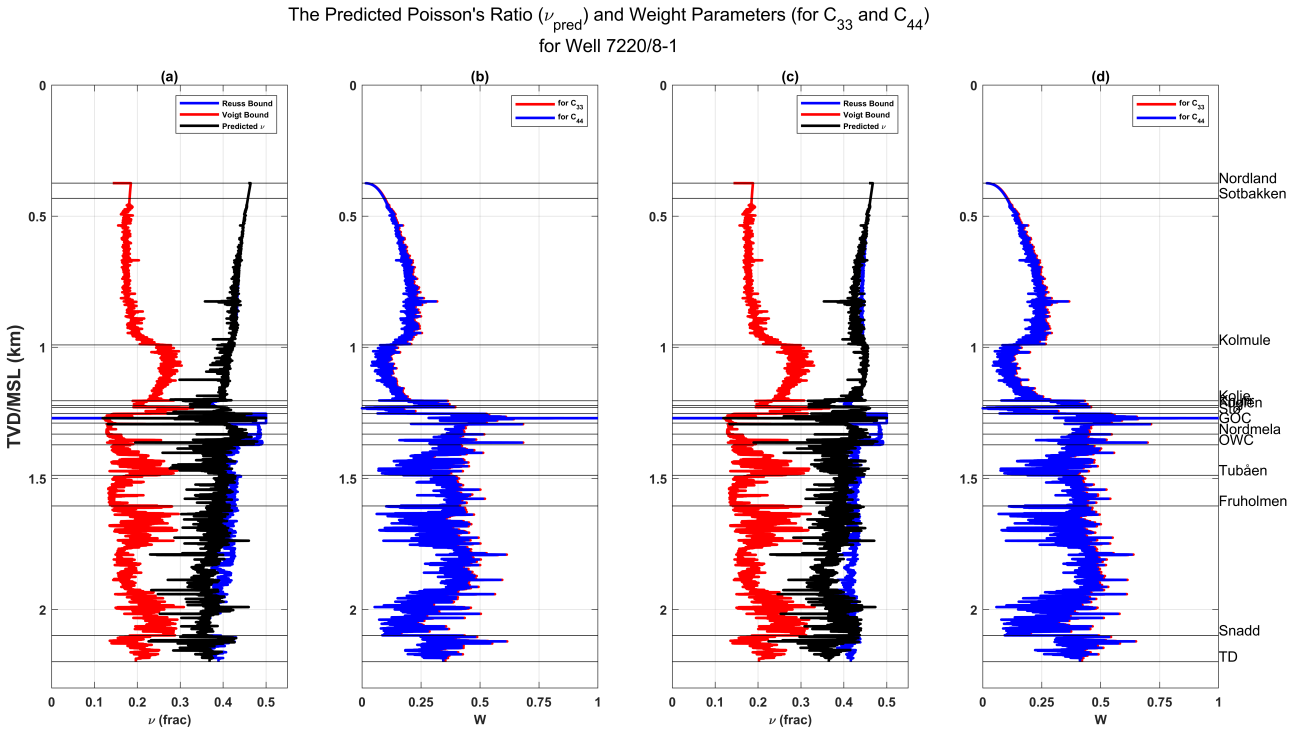

Figure 51: The predicted Poisson's ratio and weight parameters for Well 7220/8-1. subfigures a and b for Model 1 (Implicit Clay-Bound Water), while subfigures c and d for Model 2 (Explicit Clay-Bound Water).

5.7 Predicted C_{33} and C_{44}

The following figures in this subchapter are for the predicted and measured stiffness coefficients (C_{33} and C_{44}), respectively for Models 1 and 2 of Well 34/7-1 (Figure 52), Well 6704/12-1 (Figure 53), and Well 7220/8-1 (Figure 54). In all of the figures, the subfigures (a) and (b) are for Model 1, while (c) and (d) for Model 2. The red and blue curves respectively represent the measured and predicted stiffness coefficients. The procedures to calculate the predicted and measured the stiffness coefficients are shown in Equations 86-87 for C_{33} and Equations 88-89 for C_{44}.

Visually, both Models 1 and 2 show reasonable predictions to the measured stiffness coefficients, where the prediction for Model 2 is slightly lower than for Model 1. Furthermore, the predictions for both models are relatively more reliable on the deeper depth interval. The predictions for the shallower interval of Well 34/7-1 and Well 7220/8-1 are slightly different from the measured values, despite the same trend that the prediction can show. On the other hand, the predicted values for the shallower interval of Well 6704/12-1 are different from the measured values, where the measured values tend to be constant while the predicted values are not. It is also seen that both predictions of the models have a more significant variability to the measured stiffness coefficients.

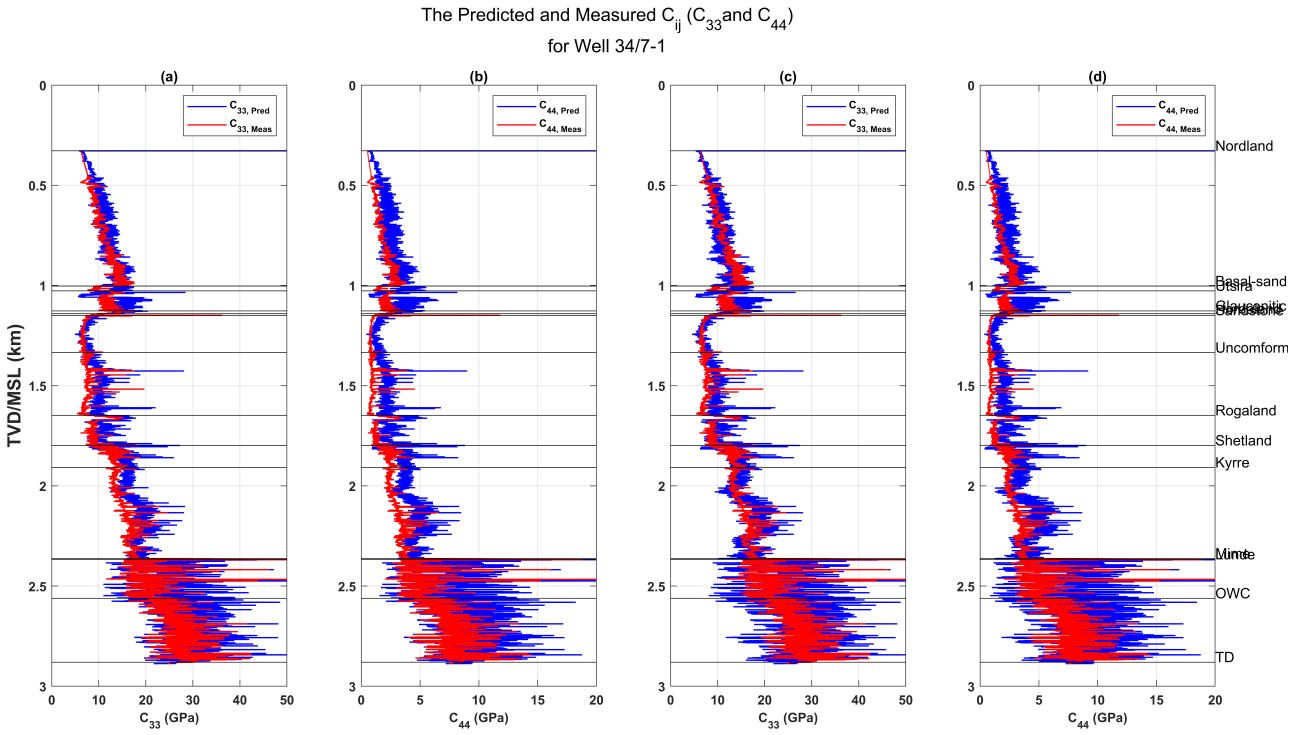

Figure 52: The predicted and measured stiffness coefficients or C_{ij} (C_{33} and C_{44}) for Well 34/7-1. subfigures a and b for Model 1 (Implicit Clay-Bound Water), while subfigures c and d for Model 2 (Explicit Clay-Bound Water).

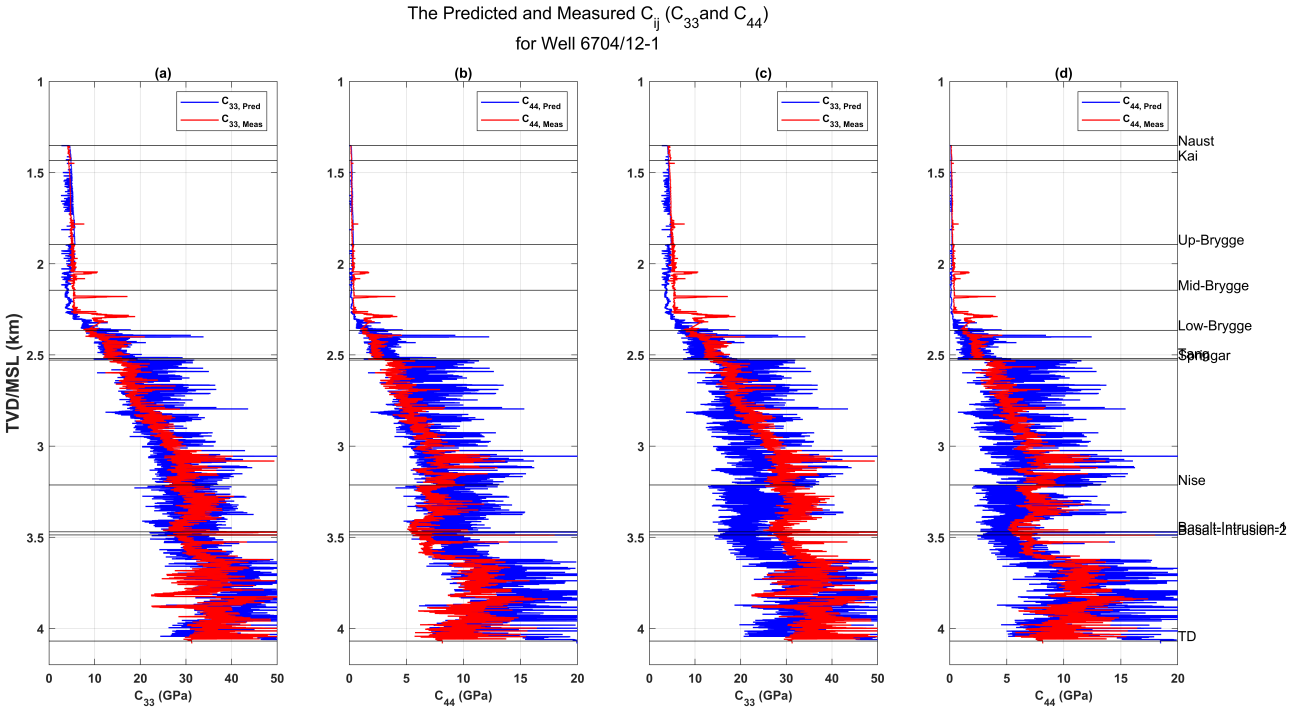

Figure 53: The predicted and measured stiffness coefficients or C_{ij} (C_{33} and C_{44}) for Well 6704/12-1. subfigures a and b for Model 1 (Implicit Clay-Bound Water), while subfigures c and d for Model 2 (Explicit Clay-Bound Water).

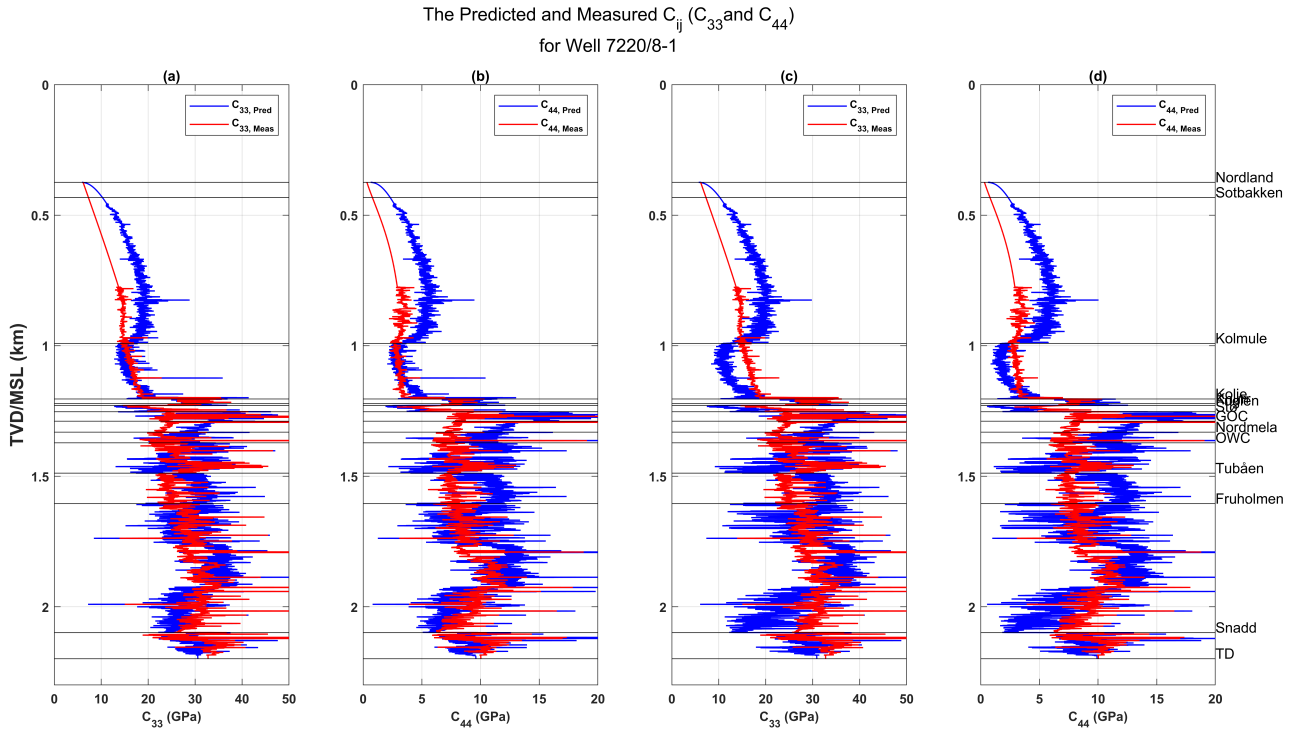

Figure 54: The predicted and measured stiffness coefficients or C_{ij} (C_{33} and C_{44}) for Well 7220/8-1. subfigures a and b for Model 1 (Implicit Clay-Bound Water), while subfigures c and d for Model 2 (Explicit Clay-Bound Water).

5.8 Predicted V_p and V_s

The following figures in this subchapter show the log comparison between predicted and measured elastic velocities (V_p and V_s), respectively for Models 1 and 2 of Well 34/7-1 (Figure 55), Well 6704/12-1 (Figure 56), and Well 7220/8-1 (Figure 57). Note that Well 34/7-1 does not have actual measured V_s since it has no shear sonic logs.

Several figures afterward show the crossplot between measured and predicted elastic velocities. Figures 58 and 59 are respectively the velocity crossplot of Well 34/7-1 concerning the lithology-fluid type and availability of the neutron porosity. Figures 60 and 61 are respectively the velocity crossplot of Well 6704/12-1 concerning the lithology and availability of the neutron porosity. Similarly for Figures 62, 63, and 64 respectively show the velocity crossplot for Well 7220/8-1 with reference to the lithologies, fluid types, and availability of the neutron porosity.

The sand interval in these crossplots refers to specific formations or groups with normalized sand volumes of more than 90%. Similarly, the clay interval refers to the interval with normalized bulk-clay volumes of more than 80%.

The 45° magenta line on these crossplot figures differentiate the overpredict and underpredict conditions. If the points are located on the right side of the magenta line, then the predicted velocities on those points overpredict the measured velocities. If the points are on the left side, then the velocities underpredict the measured velocities.

In all of these figures, the subfigures (a) and (b) are for Model 1 (Implicit Clay-Bound Water), while (c) and (d) for Model 2 (Explicit Clay-Bound Water). The procedure to obtained these predicted velocities are shown in Equations 90 and 91.

Since the predicted velocities are obtained from the previously discussed predicted stiffness coefficients, the general observations for both predicted velocities and stiffness coefficients are similar. Both models show stronger value variations (the distance between the maximum and minimum values are higher) for the predicted velocities. The velocity predictions for Model 2 have slightly more value variation than for Model 1. Despite the strong value variations, both models can pick up the general trend of the whole well. It is also seen that the velocity prediction works relatively better in the deeper depth interval.

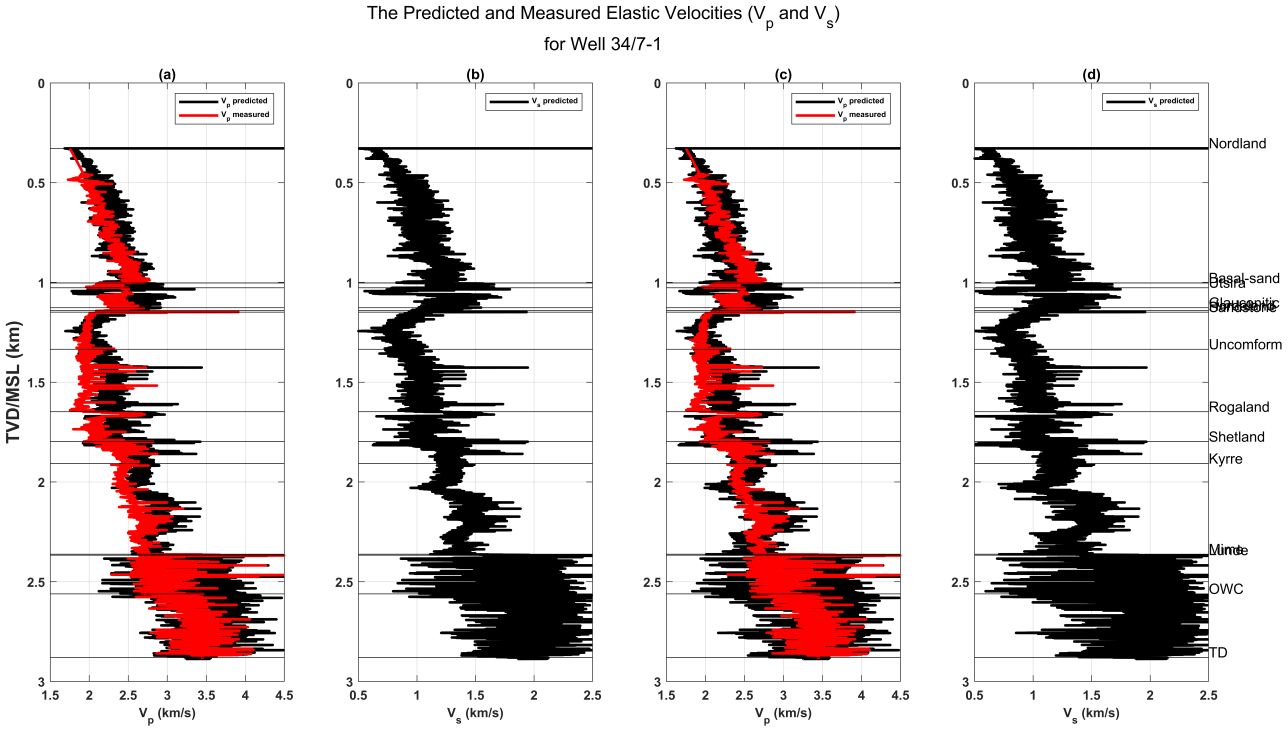

Figure 55: The predicted and measured velocities for V_p, and predicted velocity for V_s, for Well 34/7-1. subfigures a and b for Model 1 (Implicit Clay-Bound Water), while subfigures c and d for Model 2 (Explicit Clay-Bound Water).

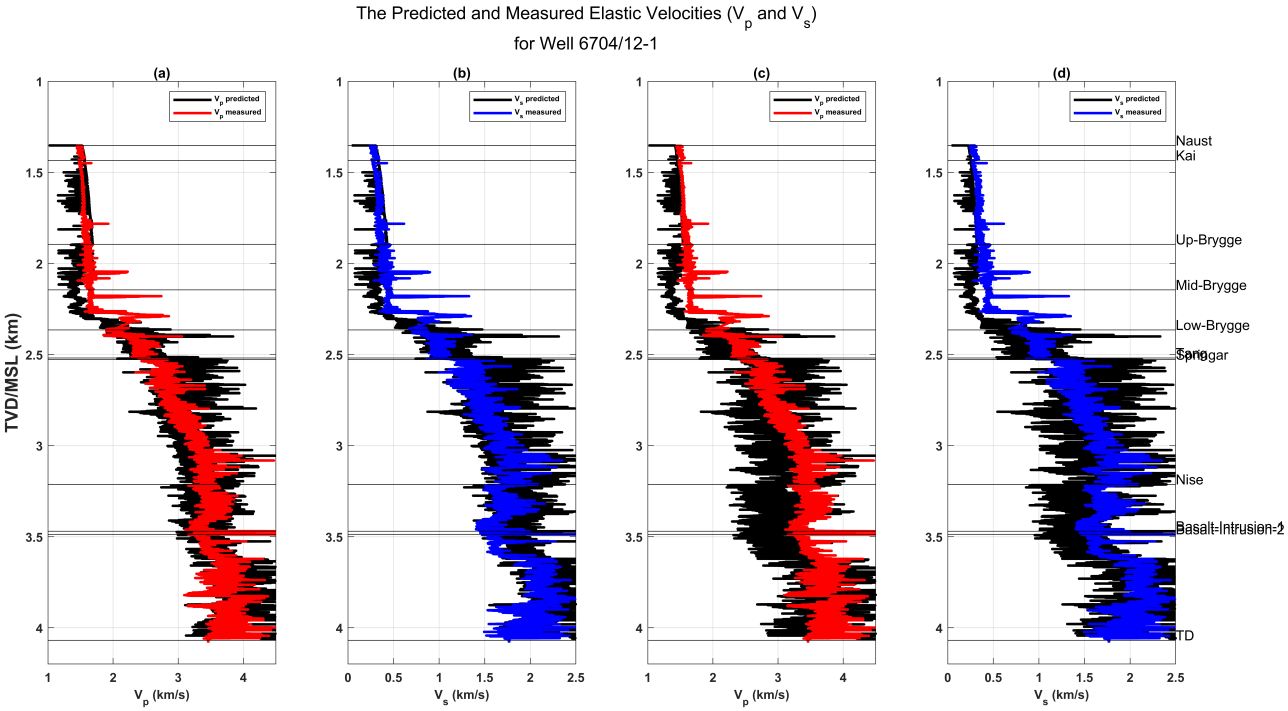

Figure 56: The predicted and measured velocities (V_p and V_s) for Well 6704/12-1. subfigures a and b for Model 1 (Implicit Clay-Bound Water), while subfigures c and d for Model 2 (Explicit Clay-Bound Water).

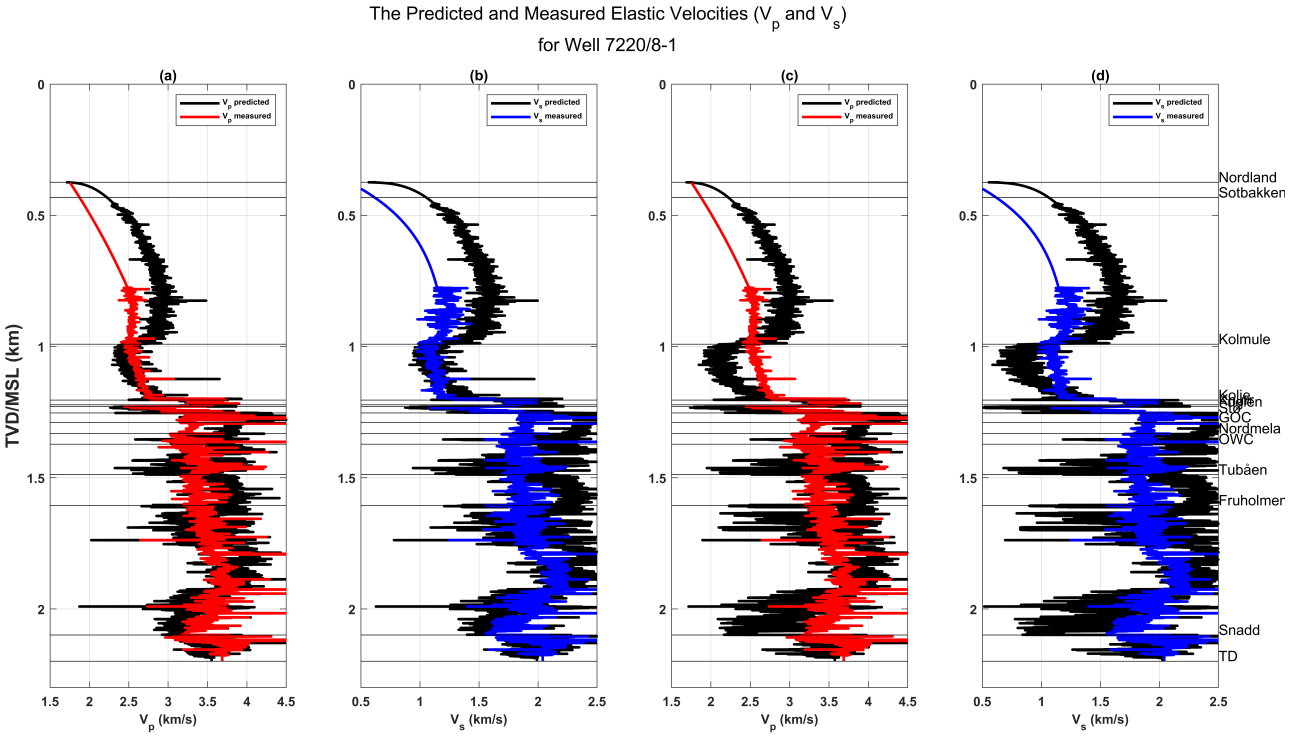

Figure 57: The predicted and measured velocities (V_p and V_s) for Well 7220/8-1. subfigures a and b for Model 1 (Implicit Clay-Bound Water), while subfigures c and d for Model 2 (Explicit Clay-Bound Water).

For the predicted-measured V_p crossplots of Well 34/7-1 (Figures 58 and 59), it is seen that the proposed model overpredicts the sand interval (basal-sand in the Nordland Group, just before reaching Utsira Formation). In contrast, the proposed model underpredicts the clay intervals of Rogaland and Shetland Groups.

The velocity prediction on the water-bearing Lunde Formation seems to be less scatter than that on the oil-bearing interval of the same interval; hence, the velocity prediction is more reliable on the water-bearing interval. Comparing the trend or gradient between the intervals with and without neutron porosity log shows that the interval with neutron porosity follows a similar gradient to the 45° magenta line; therefore, the velocity prediction on the interval that has neutron porosity logs is better. The interval that lacks the neutron porosity log is located in the shallower depth so that the velocity prediction is better on the deeper depth interval.

For the predicted-measured velocities crossplots of Well 6704/12-1 (Figures 60 and 61), the separation between sand interval and clay interval of both Springar and Nise Formation show the same observation as in Well 34/7-1; the sand and clay interval are respectively located on the right and left side of the 45° magenta line. The depth interval with neutron porosity logs follows the magenta line, while the interval that does not have neutron porosity shows a somewhat different trend from the magenta line.

Similarly, with the two previously mentioned wells, the predicted-measured velocities crossplots of Well 6704/12-1 (Figures 62, 63, and 64) show the same separation of sand-clay interval (from Tubåen and Fruholmen Formations) and better prediction for the interval that possess the Neutron porosity log. One interesting observation from this well regarding the fluid types within the reservoir is that the velocity prediction is relatively better in the water-filled Nordmela Formation, less reliable in the oil-filled Stø and Nordmela Formations, and least reliable in the gas-filled Stø Formation. From this observation, we can see that different fluid contents affect the reliability of the velocity prediction.

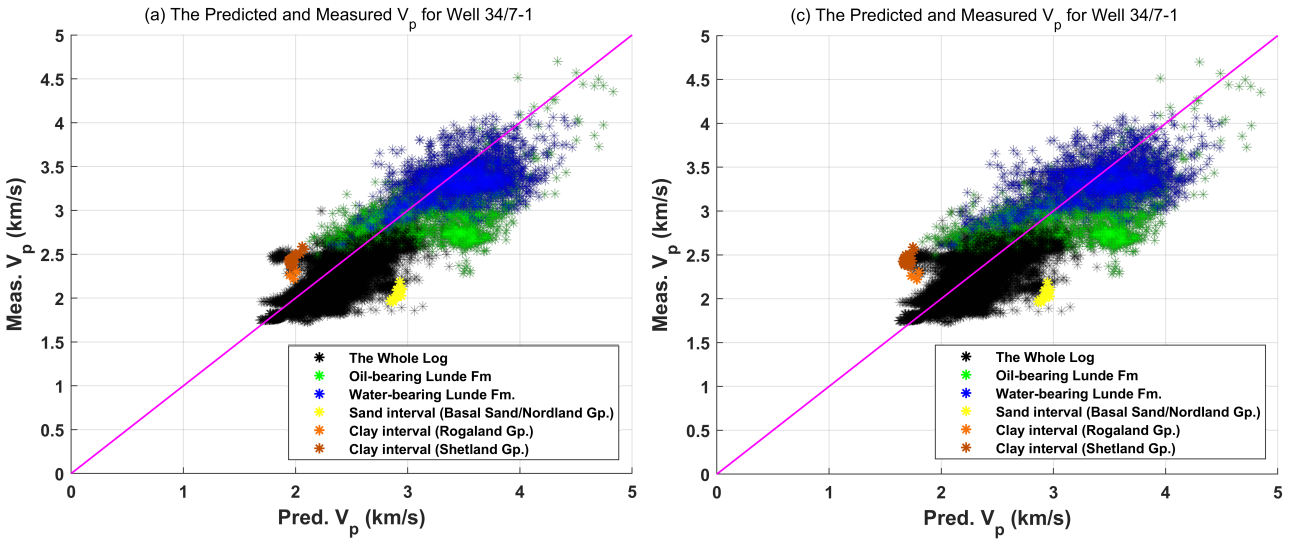

Figure 58: The crossplot between predicted and measured P-wave velocity (V_p) for **Well 34/7-1**, in respect to lithologies and fluid types. subfigure a for Model 1 (Implicit Clay-Bound Water), while subfigure c for Model 2 (Explicit Clay-Bound Water).

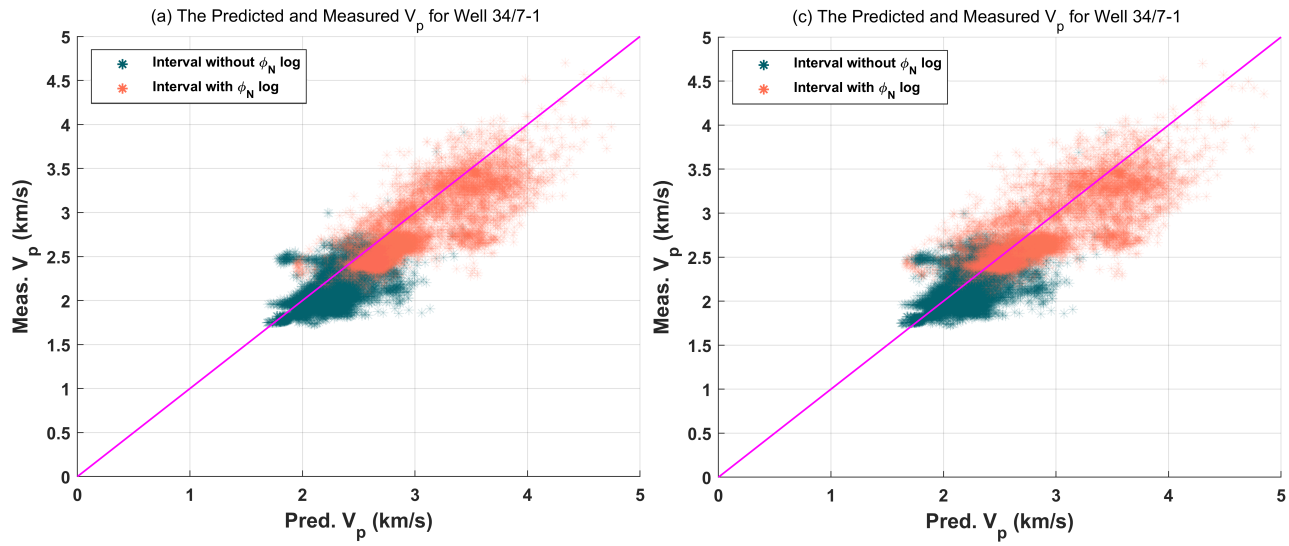

Figure 59: The crossplot between predicted and measured P-wave velocity (V_p) for **Well 34/7-1**, in respect to the availability of neutron porosity (ϕ_N) log. subfigure a for Model 1 (Implicit Clay-Bound Water), while subfigure c for Model 2 (Explicit Clay-Bound Water).

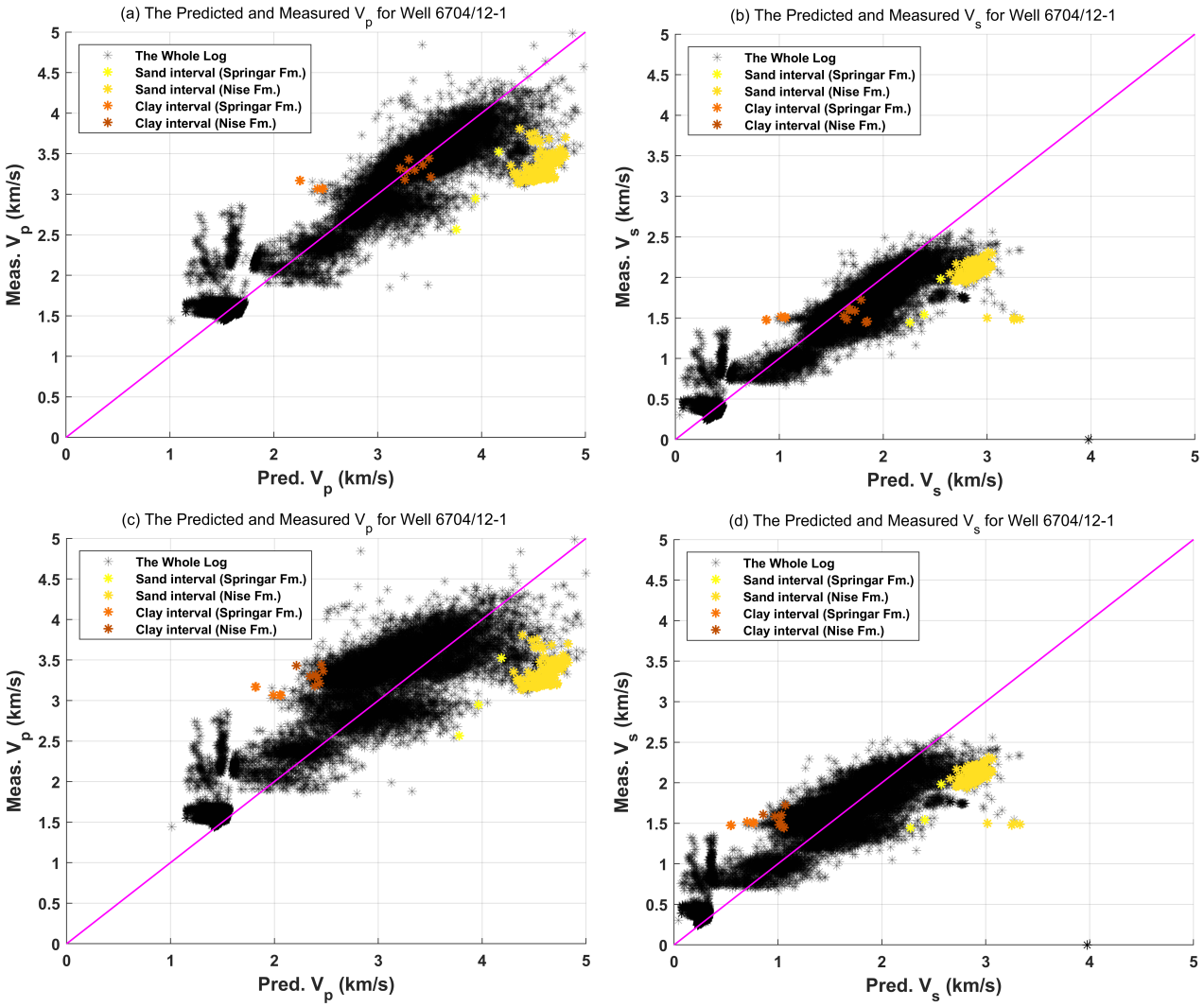

Figure 60: The crossplot between predicted and measured velocities (V_p and V_s) for **Well 6704/12-1**, in respect to lithologies and fluid types. subfigures a and b for Model 1 (Implicit Clay-Bound Water), while subfigures c and d for Model 2 (Explicit Clay-Bound Water).

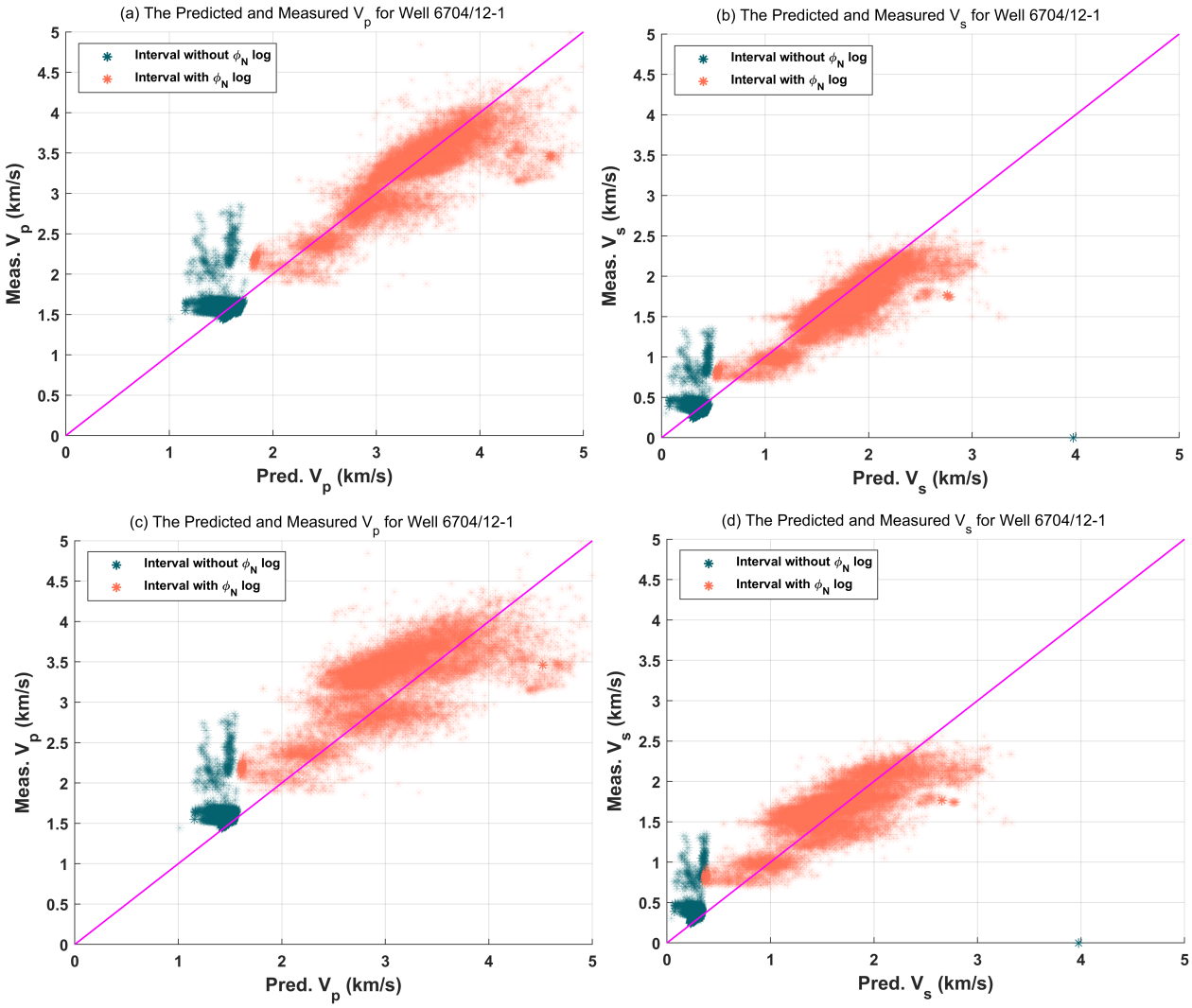

Figure 61: The crossplot between predicted and measured velocities (V_p and V_s) for **Well 6704/12-1**, in respect to the availability of neutron porosity (ϕ_N) log. subfigures a and b for Model 1 (Implicit Clay-Bound Water), while subfigures c and d for Model 2 (Explicit Clay-Bound Water).

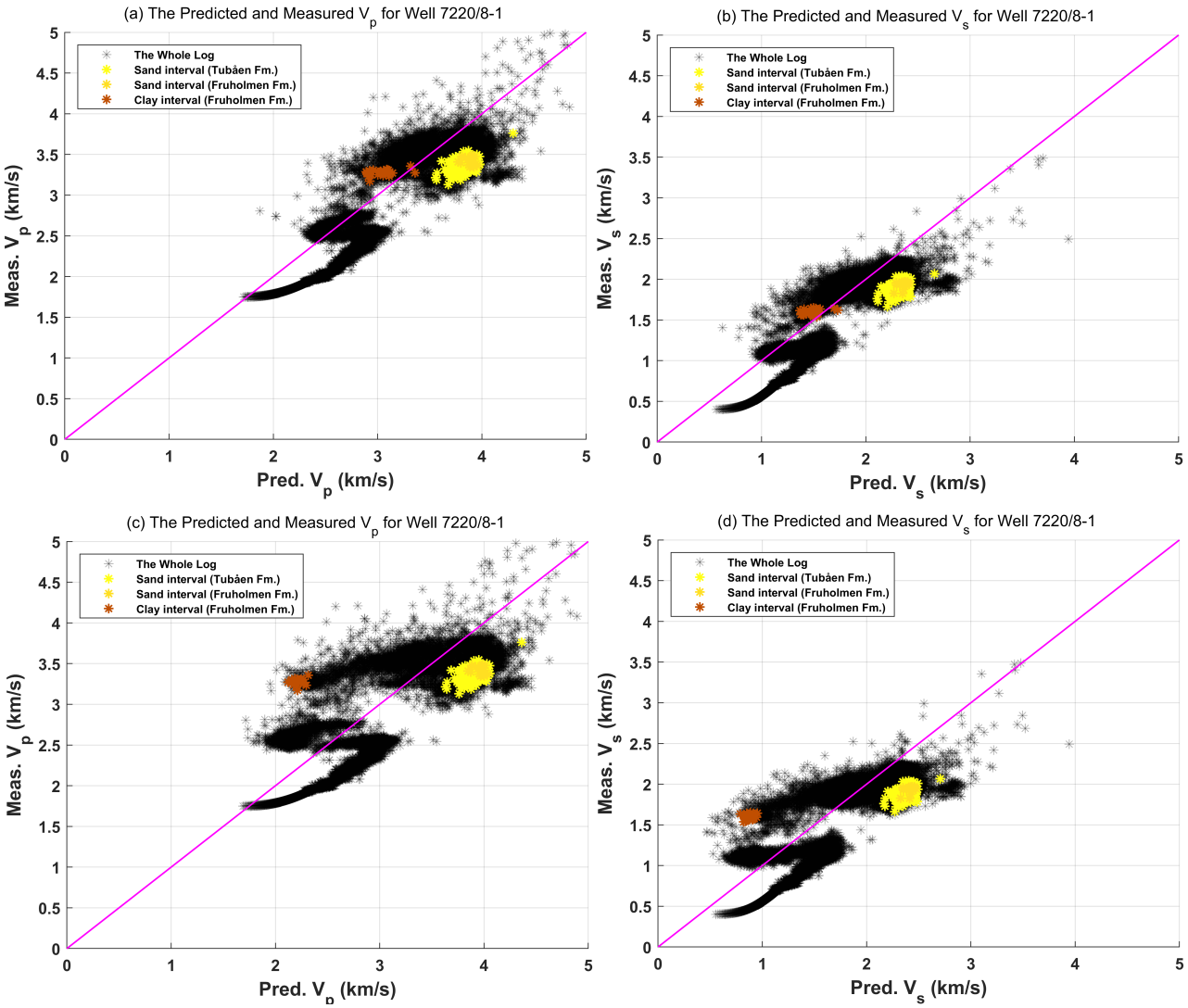

Figure 62: The crossplot between predicted and measured velocities (V_p and V_s) for **Well 7220/8-1**, in respect to lithologies. subfigures a and b for Model 1 (Implicit Clay-Bound Water), while subfigures c and d for Model 2 (Explicit Clay-Bound Water).

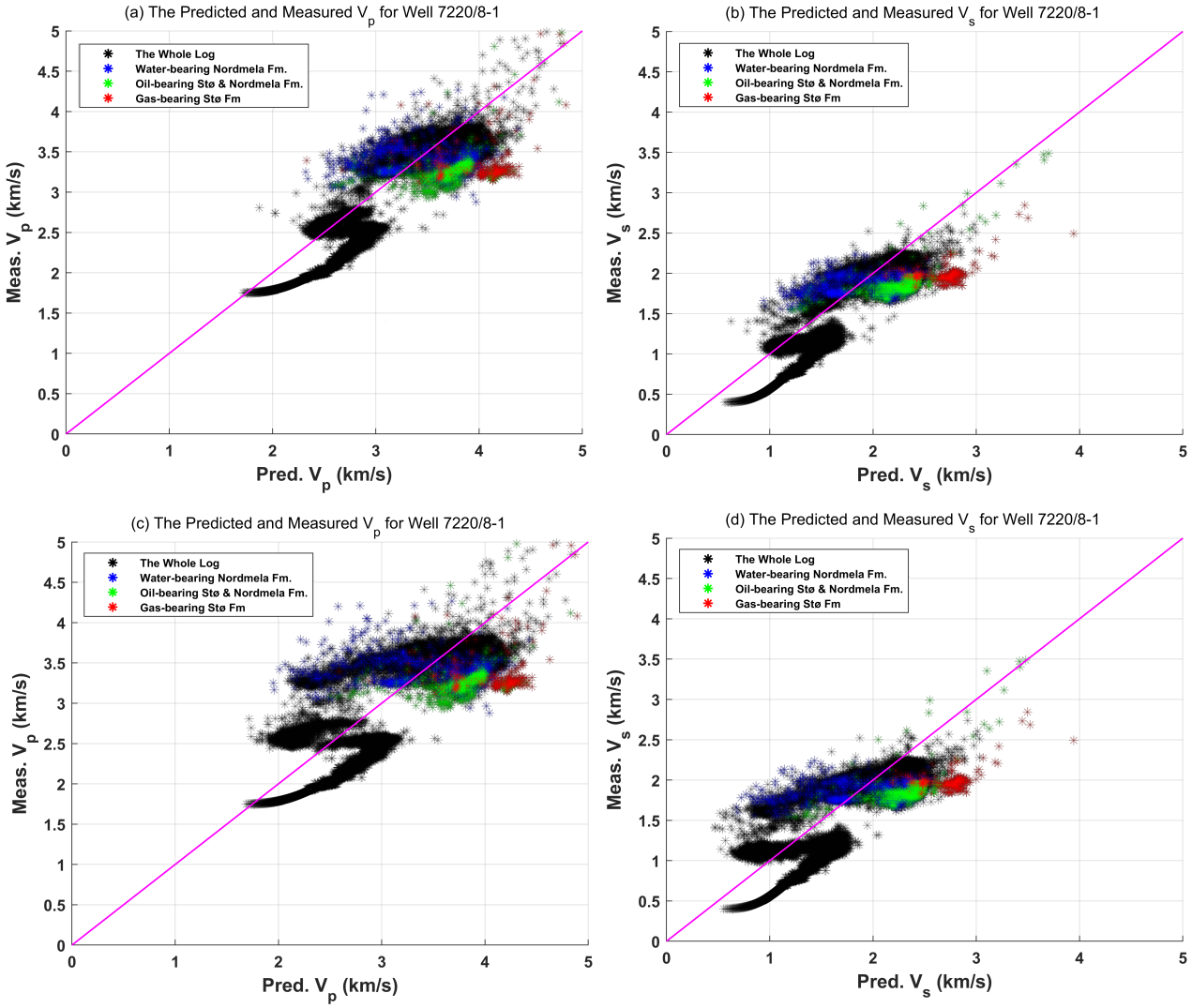

Figure 63: The crossplot between predicted and measured velocities (V_p and V_s) for **Well 7220/8-1**, in respect to fluid types. subfigures a and b for Model 1 (Implicit Clay-Bound Water), while subfigures c and d for Model 2 (Explicit Clay-Bound Water).

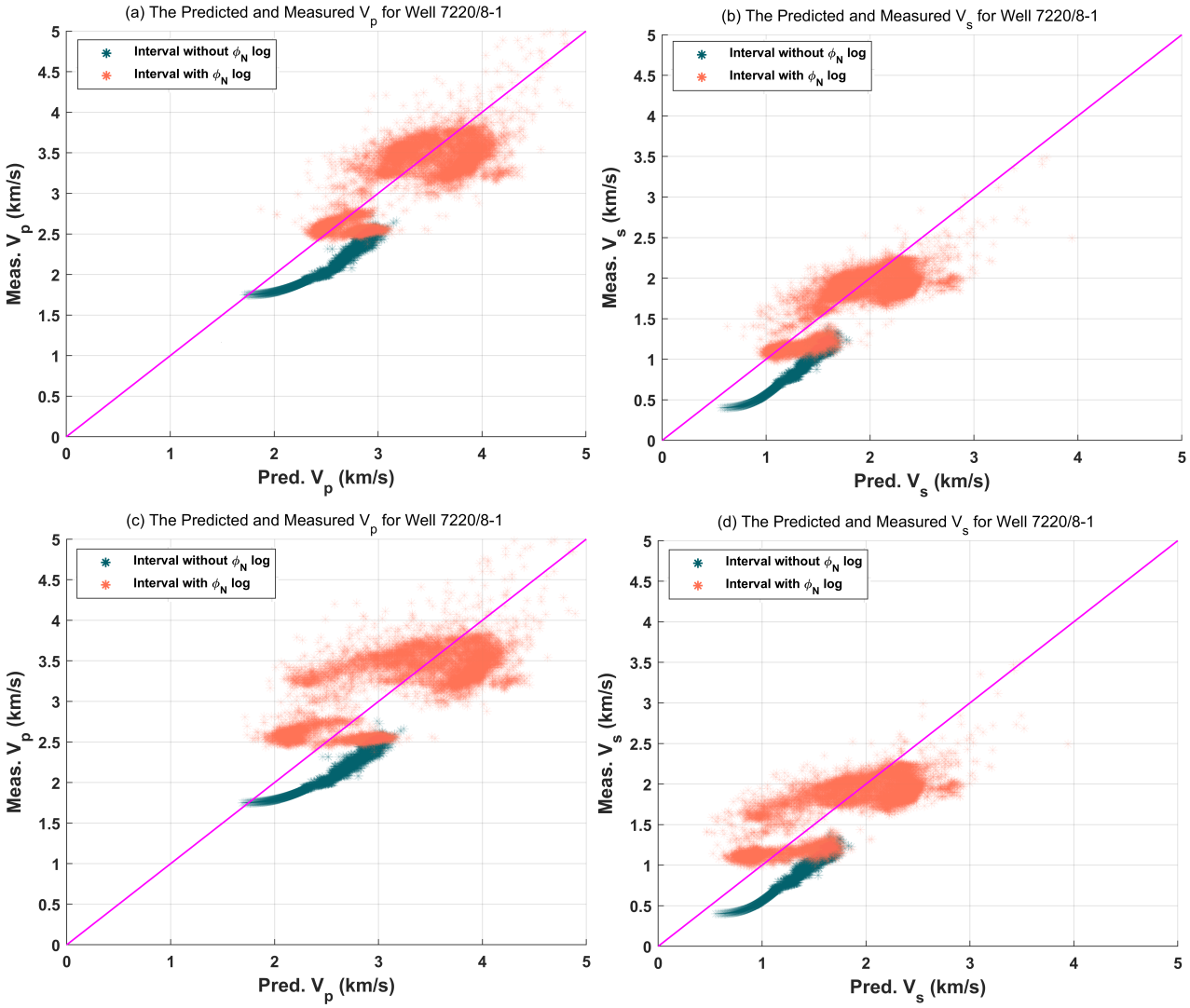

Figure 64: The crossplot between predicted and measured velocities (V_p and V_s) for **Well 7220/8-1**, in respect to the availability of neutron porosity (ϕ_N) log. subfigures a and b for Model 1 (Implicit Clay-Bound Water), while subfigures c and d for Model 2 (Explicit Clay-Bound Water).

5.9 The Correlation Coefficient and Error Percentage

After the velocity predictions are performed, then we need to assess the reliability of the prediction based on two quantification parameters, namely the correlation coefficient or R (Equation 92) and error percentage (Equations 95-96). The whole procedures to estimate these parameters could be seen in the previous chapter (subchapter 4.5). The correlation coefficients and error percentages are calculated for three different depth intervals: the whole well (from the seafloor to TD), depth interval without neutron porosity log, and depth interval with neutron porosity (Table 20).

The correlation coefficients for P-wave and S-wave velocity predictions ($R\ V_p$ and $R\ V_s$) for the whole well of the three wells are in the range of 0.8366 to 0.9585 for Model 1 and 0.7326 to 0.9336 for Model 2. The elastic velocities' (V_p and V_s) error percentages for the three wells respectively range from 22.97% to 7.73% for Model 1 and 27.66% to 8.68% for Model 2. Therefore, it is seen that the quantification parameters are consistently better for Model 1, align with the observations of the velocities and stiffness coefficients predictions in the previous subchapters. According to Schober and Schwarte (2018), the correlation coefficient for both models could be interpreted as a strong to very strong correlation (Table 19).

Further calculations of the two quantification parameters are performed between the depth intervals with a neutron porosity log and no neutron porosity log. It is seen that for all of the three wells, the quantification parameters are generally better if the depth intervals have neutron porosity logs. Generally, the S-wave velocity prediction is less reliable than the P-wave velocity prediction, which intensifies when the neutron porosity log is not available.

Table 20: The correlation coefficients and error percentages for the two models for all wells (Well 34/7-1, Well 6704/12-1, and Well 7220/8-1). Showing the values for the whole well, intervals without neutron porosity, and intervals with neutron porosity.

Quantification Parameters	**Well 34/7-1**					
	Model 1 (Implicit Clay-Bound Water)			Model 2 (Explicit Clay-Bound Water)		
	The Whole Well	Intervals without Neutron Porosity	Intervals With Neutron Porosity	The Whole Well	Intervals without Neutron Porosity	Intervals With Neutron Porosity
$R\ V_p$	**0.8889**	0.6207	0.7934	**0.8583**	0.5378	0.7549
Error Vp	**9.21%**	9.09%	9.37%	**8.68%**	8.13%	9.42%
Quantification Parameters	**Well 6704/12-1**					
	Model 1 (Implicit Clay-Bound Water)			Model 2 (Explicit Clay-Bound Water)		
	The Whole Well	Intervals without Neutron Porosity	Intervals With Neutron Porosity	The Whole Well	Intervals without Neutron Porosity	Intervals With Neutron Porosity
$R\ V_p$	**0.9521**	-0.1274	0.8334	**0.9112**	-0.1225	0.7039
$R\ V_s$	**0.9585**	0.0136	0.8573	**0.9336**	0.0972	0.7875
Error Vp	**7.73%**	8.35%	7.40%	**11.31%**	9.78%	12.13%
Error Vs	**16.2%**	20.54%	13.96%	**18.87%**	23.79%	16.23%
Quantification Parameters	**Well 7220/8-1**					
	Model 1 (Implicit Clay-Bound Water)			Model 2 (Explicit Clay-Bound Water)		
	The Whole Well	Intervals without Neutron Porosity	Intervals With Neutron Porosity	The Whole Well	Intervals without Neutron Porosity	Intervals With Neutron Porosity
$R\ V_p$	**0.8528**	0.9578	0.7768	**0.7326**	0.9447	0.7079
$R\ V_s$	**0.8366**	0.9753	0.8009	**0.7495**	0.9705	0.7606
Error Vp	**11.42%**	19.59%	8.79%	**15.07%**	20.94%	13.18%
Error Vs	**22.97%**	49.68%	14.37%	**27.66%**	53.07%	19.48%

6 Discussion

The main concepts behind the proposed methodology are the Voigt-Reuss bounding models and the Bounding Average Method (BAM). The Voigt-Reuss bounds differentiate the stiffer and softer materials in a mixture between these two endpoints; sand and clay. It is expected that the predicted elastic properties (bulk and shear moduli) of the mixture are found within the bounds. Both Voigt (1928) and Reuss (1929) bounds are among the simplest theoretical bounds based on the isostrain and isostress average of material, with three major assumptions; isotropic, elastic, and linear. However, we violate the first assumption since the proposed methodology predicts only the vertically propagating elastic wave velocities (for P-wave and S-wave, or V_p and V_s). The most significant drawback of these bounding models is that the geometrical consideration for the mixture is not taken into account.

To estimate the value of the elastic properties, we utilize a procedure to predict the exact location within the bounds. Marion (1990) proposes the Bounding Average Method, where it relies on a fitting parameter called weight parameter to locate the value between the bounds. Many studies that use BAM (Shitrit et al., 2016; Ecker 2001; Takahashi et al. 2000; Olsen et al. 2008) approximate the weight parameters without any physical reasoning or explanations. In this proposed methodology, the weight parameter (Equation 84 or 85) is a function of several parameters such as the Poisson's ratio (ν), maximum lithostatic stress (σ_{max}), critical porosity (ϕ_c), and horizontal-to-vertical net stress ratio (K_o'). Since the weight parameters rely on other physical parameters, then it is seen that the BAM improved the basic Voigt - Reuss bounding model by including the geometrical detail into consideration.

The Greenberg and Castagna (GC) approach is implemented within the proposed methodology for V_s estimation, either for predicting the V_s from the measured V_p (Subchapter 4.4.5, Equation 57) or estimating the wet C_{44} from the estimated wet V_s (Subchapter 4.4.7, Equations 77 and 78). Well 34/7-1 uses the GC approach for both cases since the shear sonic log is not available at all; Well 6704/12-1 uses the GC approach for the predicted shallower depth interval and the wet V_s; Well 7220/8-1 only uses the GC approach for estimating the wet V_s. However, the GC approach only works well for consolidated rock with V_p more than 2.6 km/s (Mavko et al., 2009). Vernik and Fisher (2002) develop non-linear regressions that solve the drawback of GC approximation in consolidated rock.

Contrary to many available empirical approaches for velocity prediction, this newly proposed methodology is designed to be robust in any given dataset, as long as we have sufficient and reliable *a priori* information regarding the wells. The completion reports from the Norwegian Petroleum Directorate (NPD) fill this part.

Based on the Voigt-Reuss bounds of several rock-physics parameters (Figures 43 to 48), the separation between the Voigt and Reuss bounds for the Model 1 (The implicit Clay-Bound Water) is significantly lesser than for the Model 2 (The explicit Clay-Bound Water). This significant separation happened because Model 1 considers the bound water volume as part of the non-solid compartment, while Model 2 considers the bound water as the solid compartment. Since elastic moduli for bound water is lower than for most of the minerals' (Table 8 and 9), the Reuss bounds are significantly affected for Model 2. Since Model 2 provides a stronger separation between the bounds, this model can better differentiate the stiffer and softer materials within the rocks.

The estimated critical porosity or ϕ_c values (Figure 41) are obtained from the lithological fractions of sand, silt, and clay (Subchapter 4.4.3, Equation 48 or 49). Since the clay volume for Model 2 is less than that for Model 1, then the ϕ_c for Model 2 is generally slightly less than for Model 1. A reason for this difference is due to the clay volumes between the two models. Model 2 uses the dry clay, while model 1 uses the bulk clay (summation of dry clay and clay-bound water). Since the ϕ_c of pure clay is around 71%, larger than for sand or silt (Table 16), then the less clay volume on model 2 means the ϕ_c is for Model 1 is expected to be lower.

The estimated maximum lithostatic stress or σ_{max} (Table 17) is obtained from the linear regression between V_p log and estimated lithostatic stress (σ). The σ_{max} represents the condition where the terminal velocity is reached; the velocity describes only the solid aggregate with no more pore left, based on each of the sand and clay ratio averages of the well. It is seen that the σ_{max} for Model 2 is consistently lower than that for Model 1 due to the reason that both models have different elements within the non-solid compartment. Model 1 has free water, bound water, and (possibly but not always) hydrocarbon, while Model 2 has the same without the bound water. Fewer elements of the non-solid compartment mean less pore space within the rock, which leads to the condition where Model 2 losses all the pore space or simultaneously reaches the terminal velocity faster.

The predicted Poisson's ratio values (Figures 49 to 51) show that the Model 2 has slightly lower (shifted toward the Voigt bound) predicted Poisson's ratio than that for Model 1. These slightly lower values for model 2 occur since the bound water is treated as part of the solid compartment, making model 2 theoretically "more solid" than model 1. The more solid Model 2, the more it tends to shift to the Voigt bound. By this nature, Model 2 has an issue of underpredict the bound water volume.

Since the predicted Poisson's ratio for Model 2 tends to be shifted into the Voigt Bound, then the estimated weight parameters for Model 2 are slightly higher than that for Model 1. This observation is reasonable since as the predicted Poisson's ratio shift to the Voigt Bound, the predicted model is stiffer. As the predicted Poisson's ratio of Model 2 becomes stiffer than for Model 1, then the weight parameter increases, which later makes the predicted C_{33} and C_{44} to be shifted into the Voigt Bound.

The predicted stiffness coefficients of C_{33} and C_{44} (Figures 52 to 54) indicate that both models consistently showing strong value variations (distance between the maximum and minimum values) in respect to the measured values along the well. Generally, Model 2 has a relatively stronger value variation than Model 1, and both models have almost the same tendency to overestimate the stiffness coefficients. An interesting observation is seen in the Well 6704/12-1, where the prediction for Model 1 tends to overestimate while Model 2 tends to underestimate. Despite these tendencies, the models can mimic the trend of the whole well with reasonable results. The predicted velocities (Figures 55 to 57) follow the same observation with the predicted stiffness coefficients, where Model 1 is more reliable than Model 2, and the prediction works better in the deeper depth interval.

The crossplots between measured-predicted velocities (Figures 58 to 64) and the quantification parameters (Pearson's correlation coefficient or R for trend similarity; error percentage for value deviation. Both are seen in Table 20) describe how well the proposed methodology predicts the velocities. Several points need to be noticed when assessing the wellness of the prediction: the lithologies (sand and clay), fluid types within the reservoir, and neutron porosity log availability.

Generally, the correlation coefficients for the velocities (V_p and V_s) range from 0.8366 to 0.9585 for Model 1 and 0.7326 to 0.9336 for Model 2. As for error percentages for the velocities range from 22.97% to 7.73% for Model 1 and 27.66% to 8.68% for Model 2. It is seen that the predictions for Model 1 are more reliable than for Model 2 due to the reason that Model 2 includes the bound water volume into the solid compartment. Hence, the value variability for Model 2 is higher than that for Model 1. Even though Model 2 shows better separation between the stiffer and softer compartments, the stronger separation intensifies the value variations, which is a disadvantage for the velocity prediction.

From the crossplots in respect to the lithologies (Figures 58, 60, and 62 are respectively for Well 34/7-1, Well 6704/12-1, and Well 7220/8-1), it is seen that the sand and clay intervals are consistently separated, where the methodology overpredicts the sand intervals and underpredicts the clay intervals. These overpredict and underpredict issues might come from to the way that the solid compartment is modelled within the proposed methodology (Equations 58-59 or Equations 60-61). We assume that the sand only consists of quartz, which in reality, could also contain other minerals such as feldspar and mica. Based on the given bulk and shear moduli of the quartz (K_{qz} and G_{qz}, Table 8), then the isotropic P-wave modulus of quartz (M_{qz}) could be estimated from Equation 63, obtaining a value of approximately 95.7 GPa. If we compare this M_{qz} to the same parameter for other typically discovered minerals within the sand (Table 9), then the value of M_{qz} is generally greater than the isotropic P-wave modulus for average feldspar (57.5 GPa) or mica (57.63 or 72.5 GPa). Neglecting the other minerals besides quartz leads to overpredict issues in the sand intervals. Similarly, for the clay intervals, we use the anisotropic P-wave modulus for clay ($C_{33,cl}$) that is smaller than the values for typical clay minerals as seen in Table 9. We use 30 GPa for the $C_{33,cl}$, while the values for typical clay minerals are in the range from 32.1 to 126.7 GPa. This significantly smaller value of $C_{33,cl}$ leads to underpredict issues for the clay intervals. Nevertheless, the proposed methodology separates sand and clay intervals, simulating the differences between stiffer and softer rocks. It is also seen

that the current velocity prediction methodology is designed to work best in a mixture between quartz-rich sand and clay.

Peltonen et al. (2008) provide the average mineralogical volumes for feldspar minerals and clay minerals from their XRD data for Well 6704/12-1, particularly for Hordaland Group (whole Brygge Formations), Rogaland Group (Tang Formation), and Shetland Group (Springer and Nise Formations). By combining the mentioned mineralogical volumes and some stiffness values as previously seen in Table 9, then we could simulate the prediction improvement by adjusting the stiffness for sand and clay, as seen in Figure 65. The same figure shows that the velocity predictions in both sand and clay intervals are slightly improved, where the clay interval points slightly move to the right while the sand interval points slightly move to the left, both getting closer to the 45° magenta line. These observations happen since the value of the P-wave modulus for clay increases while the P-wave modulus for sand decreases. Additionally, it is seen that the correlation coefficients increase while error percentages decrease as the effect of these stiffness adjustments for sand and clay, as seen in Table 21.

The crossplot for Well 34/7-1 and Well 7220/8-1 (Respectively in Figures 58 and 63) show the fluid type effect to the velocity prediction. Since Well 34/7-1 is an oil well, we can distinguish the fluid effect between water and oil. It is seen that the predicted velocities in the wet or water-bearing interval are less scatter (closer to the 45° magenta line) than that for the oil-bearing interval so that the velocity prediction is optimum in the wet interval. A similar observation in the oil-gas well of Well 7220/8-1 shows that the velocity prediction in the gas-bearing interval has the most scatter points to the 45° magenta line compared to the water- or oil- intervals. The methodology tends to overestimate the velocity prediction in the hydrocarbon-bearing intervals. One possible reason that makes this happen is the fact the estimated wet density or ρ_{wet} (subfigure d in Figures 43-44 for Well 34/7-1 or Figures 47-48 for Well 7220/8-1) is consistently underpredicts the bulk density in the hydrocarbon-bearing intervals. This underpredict issue occurs from the way we estimate the wet density (Equation 68), in which relies on how we define the density porosity or ϕ_D (Equation 8). When we estimate the ϕ_D, we follow a common practice to define the fluid density (ρ_{fl}) in the denominator to be equal to the density of water ($\rho_w = 1\ g/cc$). However, if we use either oil or gas density for the ρ_{fl}, in which they have smaller density values than water, then surely the denominator increases. As the denominator increases, the estimated ϕ_D decreases so that the ρ_{wet} increases.

In short, the common practice of using water density in the ϕ_D estimation for the hydrocarbon-bearing interval are overpredicting the ϕ_D, which intensifies the contribution of the fluid compartment in the ρ_{wet} estimation, so that the ρ_{wet} underpredicts the bulk density. This overpredict problem for ϕ_D in the hydrocarbon-bearing intervals explains why the velocity prediction works best on the wet intervals and becomes less reliable in oil-bearing intervals and least reliable in gas-bearing intervals. These unreliability problems in both oil-bearing and gas-bearing intervals occur due to different density values to water. Water has a slightly higher density value than oil, while water has a significantly higher density value than gas. A suggestion to rectify this issue is also to use oil and gas density when defining ρ_{fl} in ϕ_D estimation.

To simulate this claim, we need to define the hydrocarbon density from several references, as seen in Table 22 for oil and Table 23 for gas. The oil density is taken from the average density of several hydrocarbon (oil) constituents provided by Liu et al. (2010). On the other hand, the gas is taken from the average density from the dataset of Esfahani et al. (2015). From these tables, then we can say that the average density of oil (ρ_o) and gas (ρ_g) are respectively 0.7012 g/cc and 0.26 g/cc. Then these values are used as the ρ_{fl} when estimating the ϕ_D of each respective hydrocarbon-bearing interval. Figure 66 shows the effect of this ϕ_D adjustment, particularly for the estimated ρ_{wet} of Well 7220/8-1. On the same figure, the ϕ_D adjustment rectifies the underpredict issue of ρ_{wet} in the hydrocarbon-bearing intervals. The comparison of predicted velocities before and after ϕ_D adjustment (Figure 67) shows that the hydrocarbon-bearing interval points are slightly moving closer to the 45° magenta line after the adjustment is implemented. Therefore, the adjustment in ϕ_D is an option that solves the overpredict problem in hydrocarbon-bearing intervals.

The effect of neutron porosity log availability could be seen in Figure 59 (Well 34/7-1), Figure 61 (Well 6704/12-1), and Figure 64 (Well 7220/8-1). The interval with neutron porosity logs consistently follows the 45° magenta line, while the interval that lacks neutron porosity logs somewhat has a different trend than the 45° magenta line. The latter is either underpredicted (on Well 34/7-1) or overpredicted (on Well 6704/12-1 and Well 7220/8-1) the velocities. From these observations, we can say that the velocity prediction is preferable when the neutron porosity logs present. These observations aligned with both the correlation coefficients and error percentages for both intervals with and without neutron porosity log. The intervals with and without neutron porosity logs have correlation coefficients between 0.7039 to 0.8573 and -0.1274 to 0.9753, respectively. The error percentages for the two intervals range from 7.40% to 19.48% and 8.35% to 53.07%, respectively. From these values, it is justified that the velocity prediction for the intervals with neutron porosity is more reliable and consistent.

An explanation why these effects occur might come from the procedure of clay volume determination (Subchapter 4.3.3). When the neutron porosity log is missing, the methodology calculates the clay volume from the petrophysical baselines. This clay volume determination from baselines is prone to subjectivity and inconsistency. On the other hand, if the neutron porosity log is available, then the clay volume will be estimated using the approach of La Vigne et al. (Equation 33), where it is based on the theoretical endpoints of sand and clay. As a result, La Vigne's approach is more data-driven and objective, which explains why the interval with neutron porosity logs shows a consistent trend to the 45° magenta line and consistent values of the correlation coefficient. In order to rectify this shortcoming, we need to establish or apply an alternative way to estimate the petrophysical baselines objectively. In addition, this clay volume determination from baselines is based on the Index Gamma-Ray (IGR) approach, where it tends to overestimate the clay volume (Sharma and Chopra, 2019). Overestimating the clay could potentially lead to underpredict the velocity. Several studies suggest a non-linear correction for the IGR approach (Larionov, 1969; Clavier et al., 1971; Thomas and Stieber, 1975), as shown in Figure 23.

The depth of the logs is also affecting the velocity prediction. We agree that the interval that lacks the neutron porosity log has less reliable velocity prediction, usually located in the shallower depth interval. Hence, a more reliable prediction is expected in the deeper depth interval, where the neutron porosity is available. From this consideration, we can say that the velocity prediction works better in the deeper depth interval. Several reasons why the velocity prediction is less reliable in the shallower depth intervals are: (1) the near-seafloor or shallower logs are usually unreliable due to the unconsolidated materials (USGS, 1990; Fussi et al., 2017). (2) Those logs might just be derived from a mathematical extrapolation, which not describing the real condition. (3) The limitation of the proposed methodology itself, since the lithology is assumed to only consist of quartz-rich sand and clay (Equations 58 and 59 for Model 1; Equations 60 and 61 for model 2). We ignore the other lithologies such as limestone, dolomite, et cetera. An additional lithology of siliceous ooze sediments is introduced only for the shallower part of Well 6704/12-1. These clay-rich sediments are typically found in the seafloor of the Norwegian Sea (Awadalkarim et al., 2013). A slight adjustment to consider this ooze sediment into the solid compartment of C_{33} by replacing the P-wave modulus of quartz (M_{qz}) to be the P-wave modulus of siliceous ooze sediments (M_{oz}) in this specific depth interval, as seen in Subchapter 4.4.7. This replacement of quartz into ooze sediments is crucial to avoid a significant overpredicting tendency in the less consolidated shallow interval of the well. Ruiz (2009) provides a whole procedure to further model this ooze sediments, which could be adapted for improving the current methodology. For Well 7220/8-1, the prediction in the shallower part shows an overpredicting result, which probably occurs since that interval consist of unconsolidated rocks. An option to tackle this overprediction issue in the unconsolidated intervals is by adapting the Hertz-Mindlin contact theory to calculate the effective bulk and shear modulus into the methodology, as proposed by Bachrach and Avseth (2008).

Lastly, the methodology fitness also depends on what kind of velocity it is predicting. Visually, the V_s predictions for all the wells are relatively either more underpredict or overpredict the measured V_s, in respect to how the V_p is predicted. Furthermore, the correlation coefficients for V_p and V_s for all wells and models are between 0.7326 to 0.9521 and 0.7495 to 0.9585, in that order. The error percentages are in the range of 7.73% to 15.07% and 16.22% to 27.66%, in that order. Both correlation coefficients for V_p and V_s are pretty similar, but the error percentage for V_s is slightly more significant than that for V_p, justified the observation that V_s prediction is less reliable. A possible explanation for this comes from the whole procedure that starts only from the wet or water-saturated C_{33}, then the wet C_{44} is predicted afterward. On top of that, the V_s prediction based on the GC approach is problematic in the less consolidated rocks. A possible solution to fix this issue is to estimate the wet C_{44} in the same manner as predicting wet C_{33}, so that the GC procedure is no longer needed. Another possibility is that the mechanism to estimate the horizontal-to-vertical net stress (K'_o) is too simple, relying only on the depth interval based on Grauls (1997). This K'_o later affects the weight parameter for C_{44} afterward, which affects the V_s prediction. A viable option to improve this K'_o estimation is using the Poisson's ratio of the fracture pressure gradient (Equation 23) as proposed by Eaton (1969).

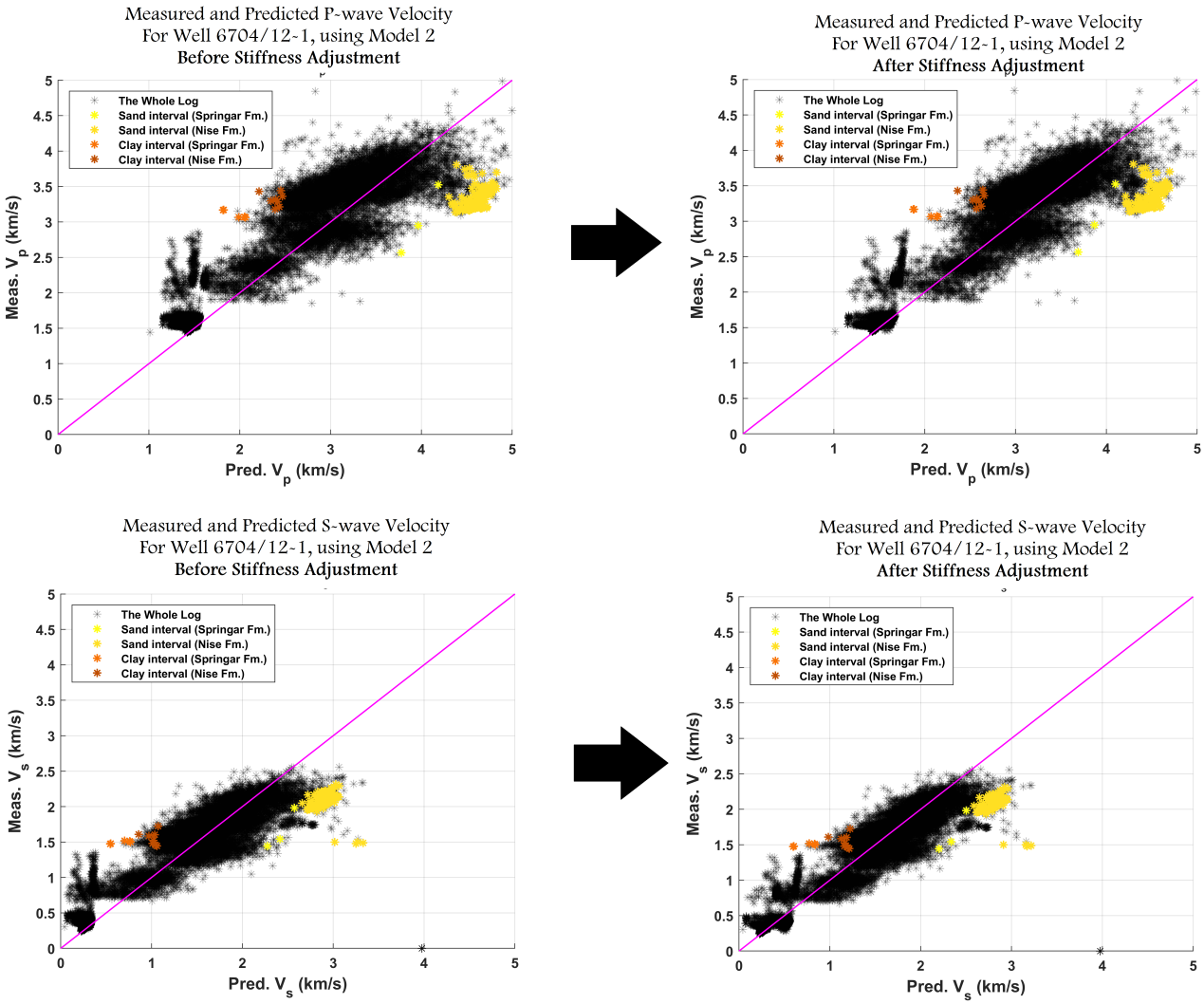

Figure 65: The comparison between the V_p and V_s predictions before stiffness adjustment (left, as seen in subfigures c and d of figure 60) and after stiffness adjustment (right), in respect to the sand and clay intervals, for **Well 6704/12-1, using Model 2**. Both intervals move slightly closer to the 45° magenta line after the stiffness adjustment.

Table 21: The correlation coefficients and error percentages of the velocities (V_p and V_s), after and before the stiffness adjustment, as previously seen in Figure 65.

Quantification Parameters	**Before Stiffness Adjustment for sand and clay (Well 6704/12-1, Model 2)**	**After Stiffness Adjustment for sand and clay (Well 6704/12-1, Model 2)**
$R\ V_p$	0.9112	0.9306
$R\ V_s$	0.9336	0.9470
Error V_p	11.31%	8.75%
Error V_s	18.87%	15.8%

Table 22: Several **oil component constituents**, taken and modified from Liu et al. (2010). The values are chosen based on the fact that the hydrocarbon in Well 7220/8-1 present in the depth intervals that have temperature between 40 - 50° C (subfigure c of Figure 33) and stress between 10 - 15 MPa (subfigure f of Figure 33).

Hydrocarbon (oil) Component Constituents	**Temperature** $[°C]$	**Pressure** $[MPa]$	**Density** $[g/cc]$	**Average Density** $[g/cc]$
n-pentane	52.7	13.8	0.613	**0.7012**
n-octane	48.7	14.3	0.688	
cyclooctane	51.3	14	0.830	
2,2,4-trimethylpentane	50.9	11.5	0.679	
2,2,4-trimethylpentane	50.9	14.4	0.683	
n-decane	51.3	14.6	0.714	

Table 23: The summarized statistical descriptions from the **gas dataset** of Esfahani et al. (2015), with some modifications or conversions for the units. The units for the temperature and pressure were originally in Fahrenheit and PSIA, respectively.

Parameters	**Minimum**	**Average**	**Maximum**
Molecular Weight	16.04	36.49	129.66
Pressure $[MPa]$	0.094	23.82	68.94
Reservoir Temperature $[°C]$	-32.06	103.25	237.78
Density $[g/cc]$	0.00038	**0.26**	0.75

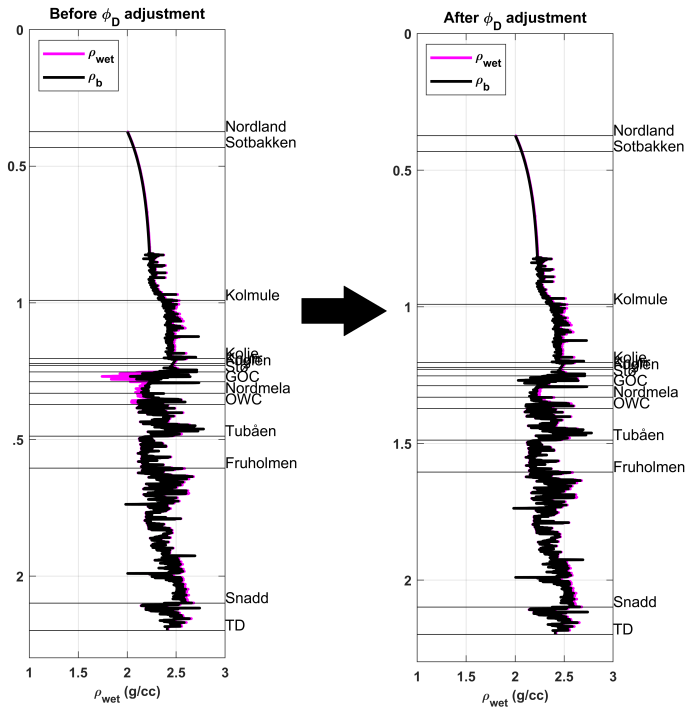

Figure 66: The comparison of the estimated wet density (ρ_{wet}) in respect to the bulk density (ρ_b), before and after the adjustment of the density porosity (ϕ_D). After the oil or gas density (ρ_o or ρ_g) is considered within the fluid density (ρ_{fl}) of ϕ_D estimation, then the underpredict issue of ρ_{wet} in the hydrocarbon-bearing intervals of **Well 7220/8-1** is solved.

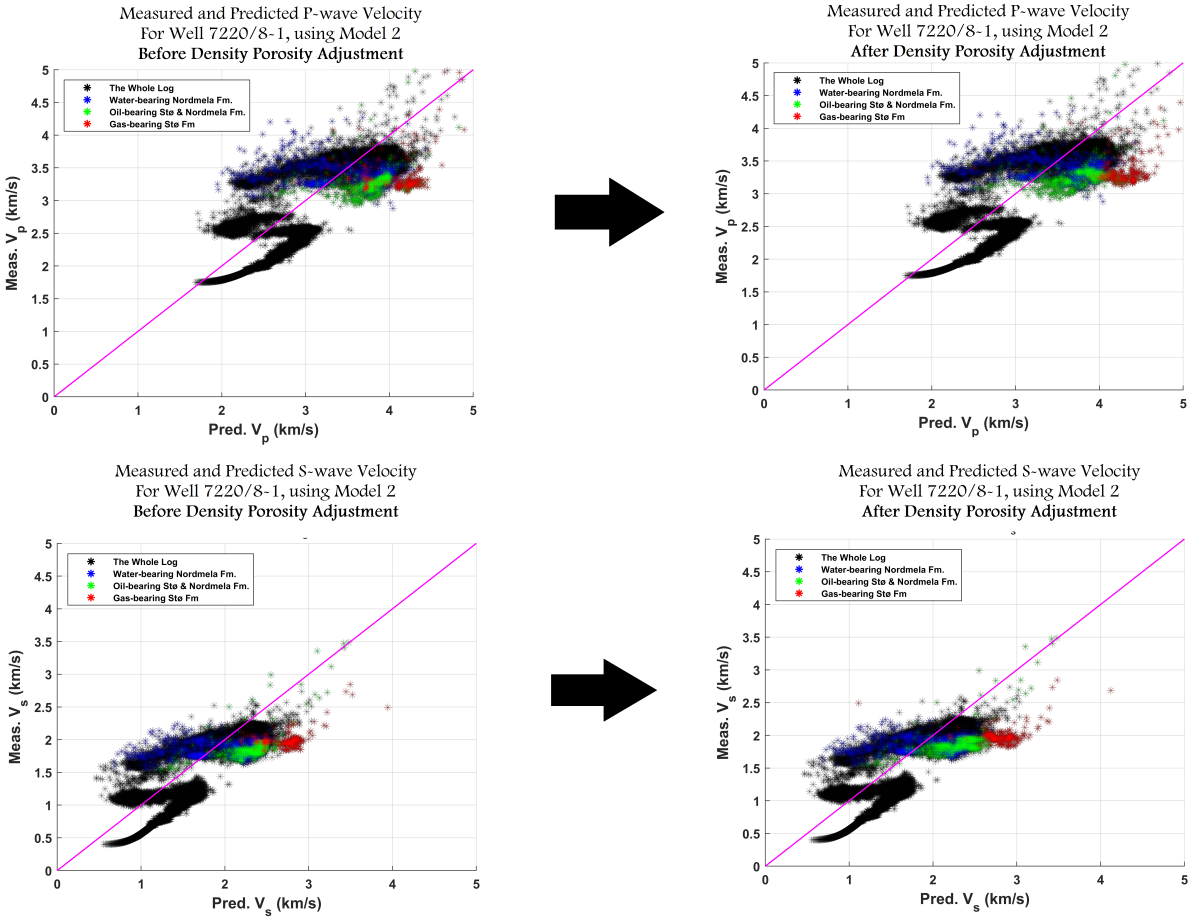

Figure 67: The comparison between the V_p and V_s predictions before density porosity or ϕ_D adjustment (left, as seen in subfigures c and d of figure 60) and after stiffness adjustment (right), in respect to the fluid-bearing intervals, for **Well 7220/8-1, using Model 2**. The hydrocarbon intervals move slightly closer to the 45° magenta line after the ϕ_D adjustment.

7 Conclusion

The proposed methodology for predicting the vertically-propagating P-wave velocity (V_p) and S-wave velocity (V_s) are mainly developed from the Voigt-Reuss bounds and the Bounding Average Method (BAM). The Voigt and Reuss bounds are used to respectively estimate the stiffer sand and softer clay endpoints of a rock, where the BAM predicts the exact position between the two bounds. The proposed methodology violates the isotropic assumption of the Voigt-Reuss bounds since it predicts only the vertically-propagating elastic velocities. The BAM relies on a fitting parameter or the weight parameter, which is defined as a function of several parameters: the Poisson's ratio, clay volume, porosity, horizontal-to-vertical net stress, and maximum lithostatic stress. The proposed methodology is designed to simulate the burial depth variations of the lithology (differentiate sand and clay using the Voigt-Reuss bounds), consolidation states (differentiate consolidated and unconsolidated sediments, based on the Poisson's ratio and critical porosity), and velocity stress-sensitivity (based on the Poisson's ratio and weight parameters).

The velocity prediction is applied to three wells within the Norwegian Continental Shelf (NCS) using consistent lithological volume estimation, pressure and temperature profiles, and rock-physics analysis. The proposed methodology generates the depth trends for vertically-propagating V_p and V_s. It works best on the implicit clay-bound water model (Model 1) since it has relatively smaller value variability than the explicit clay-bound water model (Model 2). The reliability of the velocity prediction significantly increases in the deeper depth intervals or when the neutron porosity logs are available. The velocity prediction is better for the water-bearing intervals because the estimated wet density underpredicts the bulk density in the hydrocarbon-bearing intervals. Even though the prediction for V_s is less reliable than V_p in terms of value deviation, generally, the prediction procedure can pick up the velocity depth trends reasonably good for the whole depth intervals of the three wells.

The proposed methodology has excellent predictability despite its straightforward procedures, where each of the parameters is defined and estimated accordingly. The general correlation coefficients for V_p and V_s show strong to very strong correlation, respectively, in the range of 0.7326 - 0.9521 and 0.7495 - 0.9585. The error percentage for both velocities, respectively, in the range of 7.73% - 15.07% and 16.22% - 27.66%.

Further Work

Generally, the proposed methodology is applicable only if the wells are available, especially for the bulk-density log, gamma-ray log, and neutron porosity log. However, in an exploration setting, the available wells may be located quite far from the target area; hence, the well data are unavailable. To solve this issue, then we should estimate the smooth lithological curve trend based on several depth variations of (1) porosity trends following the compaction trends, (2) sand and shale changes, and (3) temperature and stress profiles. This lithological curve trend estimation could be done by cooperating with a petrophysicist or geologist. For the compaction trend estimation, we need to consider both mechanical and chemical compaction, which the latter occurs after the temperature of a certain depth reaches around $70°C$ (Bjørlykke, 1989; Lander and Walderhaug, 1999; Goulty et al., 2012). The chemical compaction could be simulated by a quartz cementation model in sandstone, as proposed by Walderhaug (1996).

The explicit clay-bound water model (Model 2) distinguishes the bound water as a separate compartment. This approach is valuable when we need to accurately estimate the vertically propagating S-wave stiffness (C_{44}) in a VTI medium. It might be wise to estimate the C_{44} similarly as the vertically propagating P-wave stiffness (C_{33}) is estimated. The proposed methodology might also be linked for further anisotropy studies, mainly to estimate the horizontally propagating P-wave and S-wave stiffness (respectively, C_{11} and C_{66}), the same way as for the C_{33}. We should also consider other lithologies besides only quartz and clay into the solid compartment. A more data-driven approach to estimate the horizontal-to-vertical net stress (K'_o) is also needed; the proposed methodology determines the K'_o only from its depth as proposed by Grauls (1997). One option is to apply the fracture gradient approach as proposed by Eaton (1969).

The velocity prediction fails in the hydrocarbon-bearing intervals, especially for gas. As previously discussed, it happened because the wet density (ρ_{wet}) underpredicts the bulk density. A suggestion to rectify this problem is to use both water and hydrocarbon densities when defining the fluid density (ρ_{fl}) for density porosity (ϕ_D) estimation. The velocity prediction seems to fail also in the shallower unconsolidated intervals. For general unconsolidated intervals, we could implement the procedure to calculate the effective bulk and shear moduli by adapting the Hertz-Mindlin contact theory (Bachrach and Avseth, 2008), into the proposed methodology. For a particular case of Ooze sediments such as in Well 6704/12-1, we could implement the specific procedure proposed by Ruiz (2009). The reliability of V_s prediction could also be improved by using other $V_p - V_s$ relations other than Greenberg and Castagna's, such as using the Vernik and Fisher's non-linear equations.

More objective approaches for the lithological baseline estimations are needed to improve the prediction in the depth intervals that lack neutron porosity. The salinity within the well could be estimated from the available shallow to deep resistivity logs. Another consideration is to estimate each of the clay minerals' volume from the spectral gamma-ray logs when estimating the average dry-clay neutron porosity ($\phi_{N,dry-cl}$).

Lastly, it is also interesting to implement this whole methodology for several purposes: (1) Quality control of the sonic log. (2) To generate elastic velocities when we need to make a seismic section or map if the well data is not available on that specific area of interest. (3) To simulate fluid substitution analysis; One real example for this is for Carbon, Capture, and Storage (CCS) monitoring of CO_2 gas. Another example is to simulate the water-flooding effect in secondary oil recovery procedures, which benefit the production sector in the hydrocarbon industry. The velocity is expected to decreases when the gas is stored within the reservoir in CCS monitoring or increases when the injected water decreases the hydrocarbon saturation in the water-flooding process.

Acknowledgement

As the author of this MSc thesis, I would like to thank my supervisor, Professor Kenneth Duffaut, for his guidance along the way. He provides the three Norwegian offshore well data (Well 34/7-1, Well 6704/12-1, and Well 7220/8-1) for the study. He also suggested many approaches to solve problems when formulating the whole methodology for this elastic velocity prediction. I would also like to thank Dominique Paul Marion for his Bounding Average Method (BAM), which it acts as the primary mechanism for the velocity prediction in this study.

I want to thank the Norwegian Petroleum Directorate (NPD) for the available completion reports of the wells. The geological and reservoir information from the reports acts as the needed *a priori* information for the methodology. Lastly, I would like to thank the Norwegian University of Science and Technology (NTNU) for providing the MATLAB license for students and allowing me to pursue and eventually obtain my MSc degree.

References

Allen, P. A. and Allen, J. R. (2006). *Basin Analysis - Principles and Applications*. Blackwell Publishing Company, 2^{nd} edition. ISBN: 978-0-632-05207-3.

Athy, L. F. (1930). Density, porosity, and compaction of sedimentary rocks. *Bulletin of the American Association of Petroleum Geologist*, 14. DOI: 10.1306/3D93289E-16B1-11D7-8645000102C1865D.

Aubert, K., Elseth, T., Ellevset, H., Sandvik, J., Bakøy, P., and Skottlien, E. (1999). Final Well Report 6704/12-1. Technical report, Saga Petorleum. https://factpages.npd.no/pbl/wellbore_documents/3759_6704_12_1_COMPLETION_REPORT.pdf; Last checked on April 25, 2021.

Avseth, P., Mukerji, T., Mavko, G., and Dvorkin, J. (2010). Rock-physics diagnostics of depositional texture, diagenetic alterations, and reservoir heterogeneity in high-porosity siliciclastic sediments and rocks — A review of selected models and suggested work flows. *Geophysics*, 75(5). DOI: 10.1190/1.3483770.

Awadalkarim, A., Sørensen, M. K., and Fabricius, I. L. (2013). Petrophysical analysis of siliceous ooze sediments, ormen lange field, Norway. *Petrophysics*, 55(August 2014). DOI: 10.3997/2214-4609.20130800.

Bachrach, R. and Avseth, P. (2008). Rock physics modeling of unconsolidated sands: Accounting for nonuniform contacts and heterogeneous stress fields in the effective media approximation with applications to hydrocarbon exploration. *Geophysics*, 73(6). DOI: 10.1190/1.2985821.

Batzle, M. and Wang, Z. (1992). Seismic properties of pore fluids. *Geophysics*, 57(11):1396–1408. DOI: 10.1190/1.1443207.

Belyadi, H., Fathi, E., and Belyadi, F. (2019). Rock mechanical properties and in situ stresses. In *Hydraulic Fracturing in Unconventional Reservoirs*, chapter Thirteen, pages 215–231. Elsevier, 2^{nd} edition. DOI: 10.1016/b978-0-12-817665-8.00013-8.

Bent, A. (2013). Secondary Wave (S-wave). In Bobrowsky, P. T., editor, *Encyclopedia of Natural Hazards*, page 21. Springer-Verlag Berlin Heidelberg. DOI: 10.1007/978-1-4020-4399-4_311.

Berg, R. R. (1986). *Reservoir sandstones*. Prentice-Hall, Inc., New Jersey. ISBN: 0-13-774373-4.

Bjørlykke, K. (1989). *Sedimentology and Petroleum Geology*. Springer-Verlag Berlin Heidelberg, 1^{st} edition. ISBN: 978-3-540-17691-6.

Boadu, F. K. (2018). Regression Models to Estimate Critical Porosity of Soils from Basic Soil Properties Based on Percolation Theory. *Geotechnical and Geological Engineering*, 36(2):1207–1216. DOI: 10.1007/s10706-017-0387-5.

Bodaghabadi, S. and Moosavi, S. J. (2008). Simple practical method to determine the biot coefficient for hydromechanical analyses. *ISRM International Symposium - 5th Asian Rock Mechanics Symposium 2008, ARMS 2008*, (November):227–229. Paper Number: ISRM-ARMS5-2008-020.

Breitzke, M. (2000). Acoustic and elastic characterization of marine sediments by analysis, modeling, and inversion of ultrasonic P-wave transmission seismograms. *Journal of Geophysical Research*, 105(139):21411–21430. DOI: 10.1029/2000JB900153.

Brocher, T. M. (2005). *Compressional and Shear Wave Velocity Versus Depth in the San Fransisco Bay Area, California: Rules for USGS Bay Area Velocity Model 05.0.0*. USGS. https://pubs.usgs.gov/of/2005/1317/of2005-1317.pdf; Last checked on April 25, 2021.

Castagna, J. P., Batzle, M. L., and Kan, T. K. (1993). Rock physics - the link between rock properties and AVO response. In Castagna, J. P. and Backus, M. M., editors, *Offset-dependent Reflectivity — Theory and practice of AVO analysis*, pages 135–171. Society of Exploration Geophysicists. DOI: 10.1190/1.9781560802624.

Castagna, J. P., Chopra, S., and Al-Jarrah, F. (2014). Rock-physics Foundation for AVO Analysis. In *AVO*, chapter 2, pages 15–33. Society of Exploration Geophysicists. DOI: 10.1190/1.9781560803201.ch2.

Castagna, P., Batzle, M. L., and Eastwood, R. L. (1985). Relationships between compressional-wave and shear-wave velocities in clastic silicate rocks. *Geophysics*, 50(4):571–581. DOI: 10.1190/1.1441933.

Castro, P. and Huber, M. E. (2003). Chemical and physical features of seawater and the world ocean. In *Marine biology*, pages 48–71. McGraw-Hill, 4^{th} edition. ISBN: 978-0-071-19929-2.

Chen, C.-T. A. and Millero, F. J. (1977). Speed of sound in seawater at high pressures. *The Journal of the Acoustical Society of America*, 62(5):1129–1135. DOI: 10.1121/1.381646.

Clavier, C., Hoyle, W., and Meunier, D. (1971). Quantitative Interpretation of Thermal Neutron Decay Time Logs: Part I. Fundamentals and Techniques. *Journal of Petroleum Technology*, 23:743–763. DOI: 10.2118/2658-a-pa.

Dong, J. J., Hsu, J. Y., Wu, W. J., Shimamoto, T., Hung, J. H., Yeh, E. C., Wu, Y. H., and Sone, H. (2010). Stress-dependence of the permeability and porosity of sandstone and shale from TCDP Hole-A. *International Journal of Rock Mechanics and Mining Sciences*, 47(7):1141–1157. DOI: 10.1016/j.ijrmms.2010.06.019.

Duffaut, K. (2011). *Stress sensitivity of elastic wave velocities in granular media*. Doctoral thesis, Norwegian University of Science and Technology. https://ntnuopen.ntnu.no/ntnu-xmlui/handle/11250/239672; Last checked on April 25, 2021. ISBN: 978-82-471-2613-4.

Duffaut, K., Hokstad, K., Kyrkjeb, R., and Wiik, T. (2018). A simple relationship between thermal conductivity and seismic interval velocity. *Leading Edge*, 37(5):381–385. DOI: 10.1190/tle37050381.1.

Durrani, M. Z., Willson, K., Chen, J., Tapp, B., and Akram, J. (2014). Rational rock physics for improved velocity prediction and reservoir properties estimation for granite wash (Tight Sands) in Anadarko Basin, Texas. *International Journal of Geophysics*, 2014. DOI: 10.1155/2014/209351.

Dvorkin, J. and Nur, A. (2000). Critical porosity models. pages 1–12. http://pangea.stanford.edu/~jack/GP170/Reading%234.pdf; Last checked on May 18, 2021.

Dvorkin, J., Walls, J., Taner, T., Derzhi, N., and Mavko, G. (2003). Attenuation at Patchy Saturation – A Model. *Conference Proceedings, 65th EAGE Conference Exhibition, Jun 2003.*, pages 2–5. DOI: 10.3997/2214-4609-pdb.6.E23.

Eaton, B. A. (1969). Fracture gradient prediction and its application in oilfield operations. *Journal of Petroleum Technology*, 21(10):1353–1360. DOI: 10.2118/2163-pa.

Eberhart-Phillips, D., Han, D.-H., and Zoback, M. (1989). Empirical relationships among seismic velocity, effective pressure, porosity, and clay content in sandstone. *Geophysics*, 54(1):82–89. DOI: 10.1190/1.1442580.

Ecker, C. (2001). Methane Hydrate Rock Physics Models for the Blake Outer Ridge. *Standford Exploration Project Report*. http://sepwww.stanford.edu/public/docs/sep80/christine2.pdf; Last checked on May 18, 2021.

Egemen, Y. (2015). *Petrophysical analysis and rock-physics based prediction of sonic velocities in carbonates*. Master thesis, Michigan Technological University. https://digitalcommons.mtu.edu/cgi/viewcontent.cgi?article=1980&context=etds; Last checked on April 25, 2021.

Esfahani, S., Baselizadeh, S., and Hemmati-sarapardeh, A. (2015). On determination of natural gas density : Least square support vector machine modeling approach. *Journal of Natural Gas Science and Engineering*, 22:348–358. DOI: 10.1016/j.jngse.2014.12.003.

Ezekwe, N. (2010). *Petroleum Reservoir Engineering Practice*. Pearson Education, Inc., Massachusetts, 1^{st} edition. ISBN: 0-13-715283-3.

Fawad, M., Mondol, N. H., Jahren, J., and Bjørlykke, K. (2010). Microfabric and rock properties of experimentally compressed silt-clay mixtures. *Marine and Petroleum Geology*, 27(8):1698–1712. DOI: 10.1016/j.marpetgeo.2009.10.002.

Folk, R. L. (1965). *Petrology of the sedimentary rocks*. Hemphill Publishing Company, Austin, 2nd edition. https://web.archive.org/web/20060213013413/http://www.lib.utexas.edu/geo/folkready/entirefolkpdf.pdf; Last checked on June 8, 2021.

Fournier, F. R. and Borgomano, J. R. (2009). Critical porosity and elastic properties of microporous mixed carbonate-siliciclastic rocks Critical porosity and elastic properties of microporous mixed carbonate-siliciclastic rocks. *Geophysics*, 74(2):93–109. DOI: 10.1190/1.3043727.

Fussi, F. F., Fumagalli, L., Fava, F., Di Mauro, B., Kane, C. H., Niang, M., Wade, S., Hamidou, B., Colombo, R., and Bonomi, T. (2017). Classifying zones of suitability for manual drilling using textural and hydraulic parameters of shallow aquifers: a case study in northwestern Senegal. *Hydrogeology Journal*, 25:2263–2279. DOI: 10.1007/s10040-017-1642-9.

Gardner, G., Gardner, L., and Gregory, A. (1974). Formation velocity and density — The diagnostic basics for stratigraphic traps. *Geophysics*, 39(6):770–780. DOI: 10.1190/1.1440465.

Gercek, H. (2007). Poisson's ratio values for rocks. *International Journal of Rock Mechanics and Mining Sciences*, 44(1):1–13. DOI: 10.1016/j.ijrmms.2006.04.011.

Glover, P. W. J. (2005). Petrophysics (Chapter 11 - The total gamma ray log). http://homepages.see.leeds.ac.uk/~earpwjg/PG_EN/CD%20Contents/GGL-66565%20Petrophysics%20English/; Last checked on June 10, 2021.

Goulty, N. R., Ramdhan, A. M., and Jones, S. J. (2012). Chemical compaction of mudrocks in the presence of overpressure. *Petroleum Geoscience*, 18(4):471–479. DOI: 10.1144/petgeo2012-018.

Grandis, H. (2009). *Pengantar Pemodelan Inversi Geofisika*. Himpunan Ahli Geofisika Indonesia (HAGI), Bandung. http://geofisika.net/wp-content/uploads/2015/03/buku_inversi.pdf; Last checked on May 26, 2021.

Grauls, D. (1997). Minimum Principal Stress as Control of Overpressures in Sedimentary Basins. In Hendry, J. P., editor, *Geofluids II'97 - Extended Abstract (1^{st} Edition)*, pages 219–222. ISBN: 1-8977-9983-7.

Greaves, G. N., Greer, A. L., Lakes, R. S., and Rouxel, T. (2011). Poisson's ratio and modern materials. *Nature Materials*, 10:823–837. DOI: 10.1038/nmat3134.

Greenberg, M. L. and Castagna, J. P. (1992). Shear-wave velocity estimation in porous rocks: theoretical formulation, preliminary verification and applications'. *Geophysical Prospecting*, 40:195–209. DOI: 10.1111/j.1365-2478.1992.tb00371.x.

Grogan, P., Østvedt-Ghazi, A. M., Larssen, G. B., Fotland, B., Nyberg, K., Dahlgren, S., and Eidvin, T. (1999). Structural elements and petroleum geology of the Norwegian sector of the northern Barents Sea. *Petroleum Geology Conference Proceedings*, 5:247–259. DOI: 10.1144/0050247.

Guo, Z. and Li, X.-Y. (2015). Rock physics model-based prediction of shear wave velocity in the Barnett Shale formation. *Journal of Geophysics and Engineering*, 12(3):527–534. DOI: 10.1088/1742-2132/12/3/527.

Hamilton, E. L. (1956). Low Sound Velocities in High-Porosity Sediments. *The Journal of the Acoustical Society of America*, 28(16). DOI: 10.1121/1.1908208.

Han, D.-H. (1986). *Effects of Porosity and Clay Content on Acoustic Properties of Sandstones and Unconsolidated Sediments*. Dissertation for the degree of doctor of philosophy, Stanford University. https://earthsciences.stanford.edu/research/srb/docs/theses/SRB_28_OCT86_Han.pdf; Last checked on May 18, 2021.

Hansen, B. E. (2019). *Imaging Reservoir Properties of the Loppa High, Norwegian Barents Sea - Examples from Alta Discovery*. PhD thesis, University of Oslo. https://www.duo.uio.no/handle/10852/70026; Last checked on May 18, 2021.

Hantschel, T. and Kauerauf, A. I. (2009). *Fundamentals of basin and petroleum systems modeling*. 1^{st} edition. DOI: 10.1007/978-3-540-72318-9.

Hill, H., Shirley, O., and Klein, G. E. (1979). Bound water in shaly sands - its relation to Q and other formation properties. *The Log Analyst*, 20(03). Paper Number: SPWLA-1979-vXXn3a1.

Hubbert, M. K. and Willis, D. G. (1957). Mechanics of hydraulic fracturing. *Transactions of the AIME*, 210(01):153–168. DOI: 10.2118/686-G.

Juhasz, I. (1979). The critical role of Qv and formation water salinity in the evaluation of shaly formations. *The Log Analyst*, 20(04). https://www.osti.gov/biblio/6485792; Last checked on May 18, 2021.

Kolstø, M. I. (2012). *Water in shale : Molecular modeling and Rock Physics Experiments*. Phd thesis, Norwegian University of Science and Technology. https://ntnuopen.ntnu.no/ntnu-xmlui/handle/11250/239945; Last checked on May 18, 2021.

La Vigne, J., Herron, M., and Hertzog, R. (1994). Density-neutron interpretation in shaly sands. *SPWLA 35th Annual Logging Symposium 1994*. Paper Number: SPWLA-1994-EEE.

Lander, R. H. and Walderhaug, O. (1999). Predicting porosity through simulating sandstone compaction and quartz cementation. *AAPG Bulletin (American Association of Petroleum Geologists)*, 83:433–449. DOI: 10.1306/00AA9BC4-1730-11D7-8645000102C1865D.

Larionov, V. (1969). Radiometrija skwaschin. Nedra Verlag, Moscow, U.S.S.R.

Liu, K., Wu, Y., Mchugh, M. A., Baled, H., Enick, R. M., and Morreale, B. D. (2010). Equation of state modeling of high-pressure, high-temperature hydrocarbon density data. *The Journal of Supercritical Fluids*, 55(2):701–711. DOI: 10.1016/j.supflu.2010.10.004.

MacBeth, C. (2004). A classification for the pressure-sensitiviy properties of a sandstone rock frame. *Geophysics*, 69(2):497–510. DOI: 10.1190/1.1707070.

Magara, K. (1980). Comparison of Porosity-Depth Relationships of Shale and Sandstone. *Journal of Petroleum Geology*, 3(2):175–185. DOI: 10.1306/bf9ab5c4-0eb6-11d7-8643000102c1865d.

Marion, D. P. (1990). *Acoustical, Mechanical, and Transport Properties of Sediments and Granular Materials*. PhD thesis, Stanford University. https://pangea.stanford.edu/departments/geophysics/dropbox/SRB/public/docs/theses/SRB_039_FEB90_Marion.pdf; Last checked on May 18, 2021.

Mavko, G., Mukerji, T., and Dvorkin, J. (2009). *The Rock Physics Handbook, Tools for Seismic Analysis of Porous Media*. Cambridge University Press, New York, 1^{st} edition. DOI: 10.1017/CBO9780511626753.

McDonald, D. A. and Schmidt, V. (1991). *Porosity Evolution of Sandstone Reservoirs*. BP Exploration Petroleum Engineering Library. http://oilcraft.io/books/McDonald%20Schmidt%20%E2%80%93%20Porosity%20Evolution%20in%20sandstone%20reservoirs.pdf; Last checked on April 25, 2021.

Mondol, N. H., Bjørlykke, K., Jahren, J., and Høeg, K. (2007). Experimental mechanical compaction of clay mineral aggregates—Changes in physical properties of mudstones during burial. *Marine and Petroleum Geology*, 24(5):289–311. DOI: 10.1016/j.marpetgeo.2007.03.006.

Moss, B., Barson, D., Rakhit, K., Dennis, H., and Swarbrick, R. (2003). Formation pore pressures and formation waters. In Evans, D., Graham, C., Armour, A., and Bathurst, P., editors, *The Millennium Atlas: petroleum geology of the central and northern North Sea*, chapter 18, pages 317–329. The Geological Society of London, London. ISBN: 978-1-862-39119-2.

NPD (2021). 7220/8-1. https://factpages.npd.no/en/wellbore/PageView/Exploration/All/6484; https://factpages.npd.no/pbl/geochemical_pdfs/6484_1.pdf; https://factpages.npd.no/pbl/geochemical_pdfs/6484_2.pdf; Last checked on April 25, 2021.

Nur, A., Marion, D., and Yin, H. (1991). Wave velocities in sediments. In Hovem, J. M., Richardson, M., and Stoll, R., editors, *Shear Waves in Marine Sediments*, pages 131–140. Kluwer Academic Publishers. DOI: 10.1007/978-94-011-3568-9_15.

Nur, A., Mavko, G., Dvorkin, J., and Galmudi, D. (1998). Critical porosity : A key to relating physical properties to porosity in rocks. *The Leading Edge*, 17(3):357–362. DOI: 10.1190/1.1437977.

Nystuen, J. P. and Fält, L. M. (1995). Upper Triassic-Lower Jurassic reservoir rocks in the Tampen Spur area, Norwegian North Sea. *Norwegian Petroleum Society Special Publications*, 4:135–179. DOI: 10.1016/S0928-8937(06)80041-X.

Odden, W., Patience, R. L., and Van Graas, G. W. (1998). Application of light hydrocarbons (C_4-C_{13}) to oil/source rock correlations: A study of the light hydrocarbon compositions of source rocks and test fluids from offshore Mid-Norway. *Organic Geochemistry*, 28(12):823–847. DOI: 10.1016/S0146-6380(98)00039-4.

Olsen, C., Hedegaard, K., Fabricius, I. L., and Prasad, M. (2008). Prediction of Biot's coefficient from rock-physical modeling of North Sea chalk. *Geophysics*, 73(2). DOI: 10.1190/1.2838158.

Peeters, M. and Holmes, A. (2014). Review of existing shaly sand evaluation models and introduction of a new method based on dry clay parameters. *Petrophysics*, 55(06):543–553. Paper Number: SPWLA-2014-v55n6a1.

Peltonen, C., Marcussen, Ø., Bjørlykke, K., and Jahren, J. (2008). Mineralogical control on mudstone compaction: A study of late cretaceous to early tertiary mudstones of the Vøring and Møre basins, Norwegian Sea. *Petroleum Geoscience*, 14(2):127–138. DOI: 10.1144/1354-079308-758.

Poisson, S. D. (1829). *Mémoire sur l'équilibre et le mouvement des corps élastiques*. Mémoires de l'académie royal des sciences de l'institut de France.

Prakoso, S., Permadi, P., Winardhi, S., and Marhaendrajana, T. (2018). Dependence of critical porosity on pore geometry and pore structure and its use in estimating porosity and permeability. *Journal of Petroleum Exploration and Production Technology*, 8:431–444. DOI: 10.1007/s13202-017-0411-6.

Raymer, L. L., Hunt, E. R., and Gardner, J. S. (1980). An improved sonic transit time-to-porosity transform. *SPWLA Twenty-First Annual Logging Symposium*. Paper Number: SPWLA-1980-P.

Reuss, A. (1929). Berechnung der Fließgrenze von Mischkristallen auf Grund der Plastizitätsbedingung für Einkristalle . *Journal of Applied Mathematics and Mechanics / Zeitschrift für Angewandte Mathematik und Mechanik*, 9(1):49–58. DOI: 10.1002/zamm.19290090104.

Rider, M. (1999). The Geological Interpretation of Well Logs. Whittles Publishing Services, 2^{nd} edition. ISBN: 978-0-9541906-0-6.

Rieke, H. H. and Chilingarian, G. V. (1974). *Compaction of Argillaceous Sediments, Volume 16*. Elsevier Science, 1^{st} edition. ISBN: 978-0-080-86927-8.

Ruiz, F. J. (2009). *Porous Grain Model and Equivalent Elastic Medium Approach For Predicting Effective Elastic Properties of Sedimentary Rocks*. Dissertation, Stanford University. https://earthsciences.stanford.edu/research/srb/docs/theses/SRB_120_AUG09_Ruiz1.pdf; Last checked on May 18, 2021.

Saga Petroleum (1985). Final Well Report 34/7-1. Technical report, Saga Petroleum. https://factpages.npd.no/pbl/wellbore_documents/111_01_34_7_1_Completion_Report_and_Log.pdf; Last checked on April 25, 2021.

Schlumberger (1990). *Log Interpretation Principles/Applications*. Schlumberger, Texas, 7^{th} edition. SMP-7017.

Schlumberger (2009). *Log Interpretation Charts*. Schlumberger, Texas, 2013 edition. ISBN: 978-1-937949-10-5.

Schober, P. and Schwarte, L. A. (2018). Correlation coefficients: Appropriate use and interpretation. *Anesthesia and Analgesia*, 126(5):1763–1768. DOI: 10.1213/ANE.0000000000002864.

Schön, J. H. (2015). *Physical Properties of Rocks - Fundamentals and Principles of Petrophysics*. Elsevier, 2^{nd} edition. ISBN: 978-0-08-100404-3.

Serra, O. (1979). Les diagraphies différées: leur emploi en géologie sédimentaire. *Bulletin des centres de recherches exploration - Production Elf-Aquitaine*, 10(2):205–227. ISBN: 978-2-901-02606-8.

Sharma, R. K. and Chopra, S. (2019). Uncertainty in the Estimation of Volume of Shale from Well Log Data. *Search and Discovery Article #42342*. https://www.searchanddiscovery.com/documents/2019/42342sharma/ndx_sharma.pdf; Last checked on May 18, 2021.

Shitrit, O., Hatzor, Y. H., Feinstein, S., Palchik, V., and Vinegar, H. J. (2016). Effect of kerogen on rock physics of immature organic-rich chalks. *Marine and Petroleum Geology*, 73:392–404. DOI: 10.1016/j.marpetgeo.2016.03.023.

Simm, R. (2007). Practical Gassmann fluid substitution in sand / shale sequences. *First Break*, 25(12):61–68. DOI: 10.3997/1365-2397.2007030.

Smith, B. and Brown, L. (2005). Extrapolation to critical porosity with the Hashin-Shtrikman Lower Bound. In *SEG Technical Program Expanded Abstracts 2005*, pages 1485–1489. DOI: 10.1190/1.2147971.

Takahashi, I., Mukerji, T., and Mavko, G. (2000). Vp - Vs relations of sandstones and carbonates: Implication about the pore structure. *SEG 2000 Expanded Abstracts*. Paper Number: SEG-2000-1838.

Teng, L. (1997). RPHtools. https://pangea.stanford.edu/departments/geophysics/dropbox/SRB/public/data/RPHtools.htm; Last checked on April 17, 2021.

Thomas, E. C. and Stieber, S. J. (1975). The distribution of shale in sandstones and its effect upon porosity. *SPWLA 16th Annual Logging Symposium 1975*. Paper Number: SPWLA-1975-T.

Tiab, D. and Donaldson, E. (2004). *Petrophysics - Theory and Practice of Measuring Reservoir Rock and Fluid Transport Properties*. Gulf Professional Publishing (Elsevier), 2^{nd} edition. ISBN: 978-0-750677-11-0.

Tosaya, C. and Nur, A. (1982). Effects of diagenesis and clays on compressional velocities in rocks. 9(1):5–8. DOI: 10.1029/GL009i001p00005.

Tucker, M. E. (2003). *Sedimentary rocks in the field (Geological Field Guide)*. John Wiley Sons Inc., West Sussex, 3^{rd} edition. ISBN: 978-0-470851-23-4.

USGS (1990). *Safe Disposal of Radionuclides in Low-Level Radioactive-Waste Repository Sites: Low-Level Radioactive-Waste Disposal Workshop, U.S. Geological Survey, July 11-16, 1987, Big Bear Lake, California., Proceedings*. Washington. https://pubs.usgs.gov/circ/1990/1036/report.pdf; Last checked on April 25, 2021.

Vernik, L. and Fisher, D. (2002). Estimation of net-to-gross from P and S impedance in deepwater turbidites. *Leading Edge*, 21(4). DOI: 10.1190/1.1471602.

Vernik, L. and Kachanov, M. (2010). Modeling elastic properties of siliciclastic rocks. *Geophysics*, 75(6). DOI: 10.1190/1.3494031.

Voigt, W. (1928). *Lehrbuch der Kristallphysik (mit Ausschluss der Kristalloptik)*. Teubner-Verlag. ISBN: 978-3-663-15884-4.

Vyzhva, S. A., Prodayvoda, G. T., and Vyzhva, A. S. (2014). Elastic properties of some clay minerals. *Nafta-gaz, Monthly journal of the Oil and Gas Institute – National Research Institute*, 70(11):743–756. http://archiwum.inig.pl/INST/nafta-gaz/nafta-gaz/Nafta-Gaz-2014-11-01.pdf; Last checked on May 22, 2021.

Walderhaug, O. (1996). Kinetic modeling of quartz cementation and porosity loss in deeply buried sandstone reservoirs. *AAPG Bulletin*, 80(5):731–745. DOI: 10.1306/64ED88A4-1724-11D7-8645000102C1865D.

Weaver, C. and Pollard, L. (1973). The Chemistry of Clay Minerals, Volume 15. In *Developments in Sedimentology*. Elsevier, Amsterdam, 1^{st} edition. ISBN: 978-0-080-86926-1.

Williams, D. M. (1990). The acoustic log hydrocarbon indicator. *SPWLA 31st Annual Logging Symposium*. Paper Number: SPWLA-1990-W.

Wyllie, M., Gregory, A., and Gardner, L. (1955). Elastic wave velocities in hetereogeneous and porous media. *Geophysics*, 21(1):41–70. DOI: 10.1190/1.1438217.

Xu, S. and White, R. E. (1996). A physical model for shear-wave velocity prediction. *Geophysical Prospecting*, 44(4):687–717. DOI: 10.1111/j.1365-2478.1996.tb00170.x.

Yale, D. P. and Jamieson, W. H. (1994). Static and dynamic rock mechanical properties in the Hugoton and Panoma fields, Kansas. *Proceedings of the Mid-Continent Gas Symposium*, pages 209–219. DOI: 10.2523/27939-ms.

Yin, H. (1992). *Acoustic Velocity and Attenuation of Rocks, Isotropy, Intrinsic Anisotropy, and Stress Induced Anisotropy*. Dissertation for the degree of doctor of philosophy, Standford University. https://pangea.stanford.edu/departments/geophysics/dropbox/SRB/public/docs/theses/SRB_052_DEC92_YIN.pdf; Last checked on April 25, 2021.

Appendices

Appendix A:

Formation Pressure Profile/Data for Well 34/7-1.
Taken and modified from the final well report, provided by the NPD (Saga Petroleum, 1985)

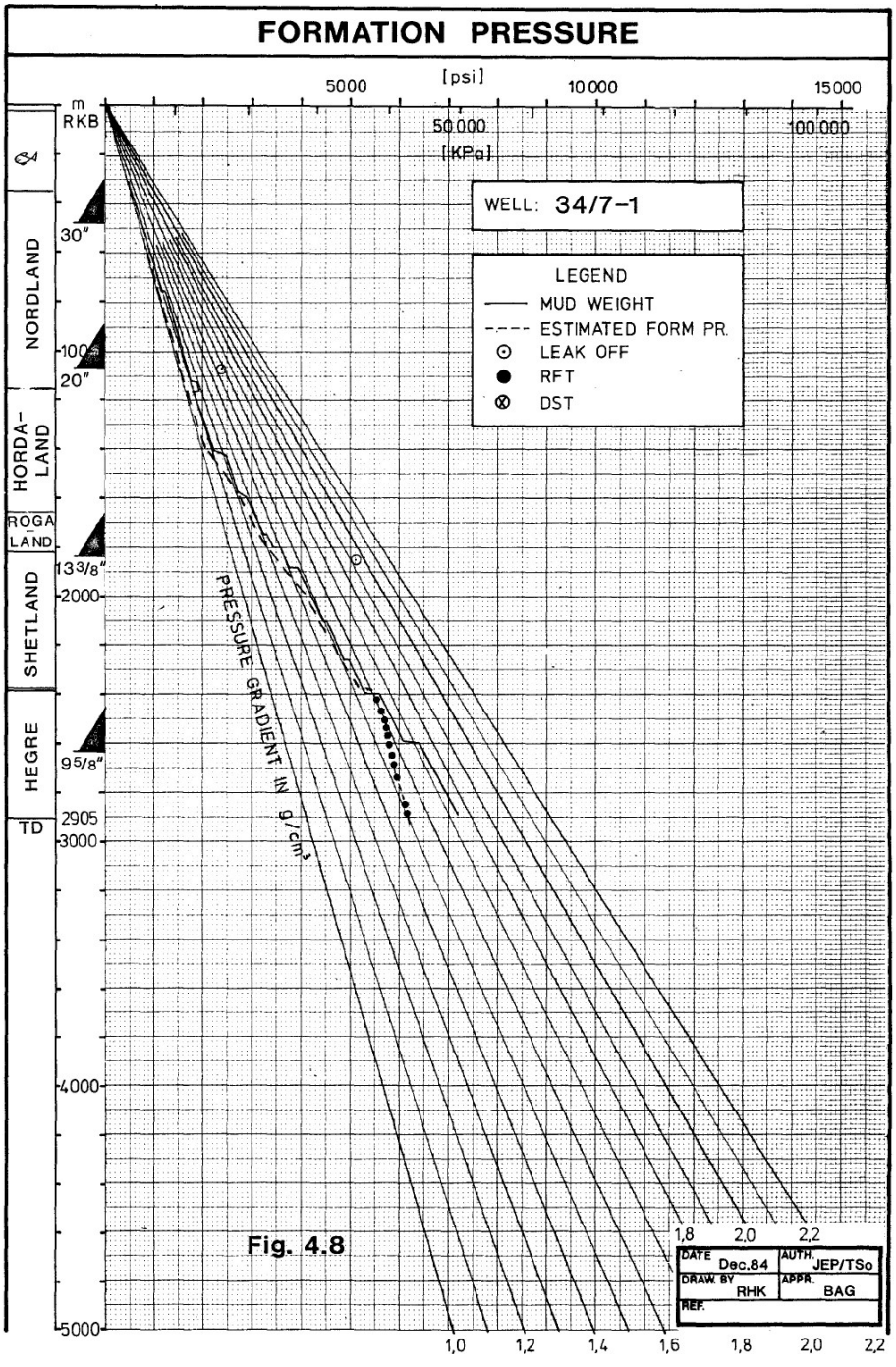

Fig. 4.8

Formation Pressure Measurements						
Depth [m RKB]	**Hydrostatic Mud Pressure [Psia]**	**Measured Formation Pressure [Psia]**	**Temperature Corrected Formation**		**Equivalent Pressure Gradient (ref to MSL)**	
			Pressure [Psia]	**Pressure [Bar]**	$[g/cc]$	**[ppg]**
Run 3A (HP GAUGE)						
2394	5705	5455	5455	376.1	1.619	13.51
2401	5710	5463	5463	376.7	1.616	13.49
2414	5734	5475	5475	377.5	1.611	13.44
2430	5771	5491	5491	378.6	1.605	13.39
2460	5844	5520	5520	380.6	1.594	13.3
2476	5881	5536	5536	381.7	1.588	13.25
2497	5931	5556	5556	383.1	1.58	13.19
2506	5952	5569	5569	384	1.578	13.17
2520	5983	5580	5580	384.7	1.572	13.12
Run 3A-II (HP GAUGE)						
2414	5761	5474	5474	377.4	1.611	13.44
2552	6074	5611	5611	386.9	1.561	13.03
2566	6091	5625	5625	387.8	1.556	12.99
2576	6116	5635	5635	388.5	1.553	12.96
Run 3A-III (HP GAUGE)						
2414	5762	5475	5475	377.5	1.611	13.44
2592.5	6185	5655	5655	389.9	1.549	12.93
2595	6176	5657	5657	390	1.548	12.92
2616	6230	5700	5700	393	1.547	12.91
2619.5	6226	5699	5699	392.9	1.544	12.89
2618.5	6213	5693	5693	392.5	1.543	12.88
2616	6207	5687	5687	392.1	1.543	12.88
2595	6155	5653	5653	389.8	1.546	12.9
2593	6152	5652	5652	389.7	1.547	12.91
2592.5	6152	5653	5653	389.8	1.548	12.92
2397	5693	5457	5457	376.2	1.617	13.49
Run 4B (STRAIN GAUGE)						
2580	6485	5634	5632	388.3	1.550	12.94
2594	6515	5659	5657	390	1.548	12.92
2617	6556	5688	5686	392	1.542	12.87
2639	6601	5720	5718	394.2	1.538	12.84
2683	6708	5780	5778	398.4	1.528	12.75
2735	6842	5857	5855	403.7	1.519	12.68
2847	7122	6018	6016	414.8	1.499	12.51
2874	7185	6058	6056	417.5	1.494	12.47
2497	6288	5595	5593	385.6	1.591	13.28

Appendix B:

Conventional Core Analysis Data of Well 34/7-1
Taken and modified from the final well report, provided by the NPD (Saga Petroleum, 1985)

Conventional Core Analysis Data											
Depth [m RKB]	Porosity [frac]	Horizontal Permeability [mD]	Oil Saturation [frac]	Depth [m RKB]	Porosity [frac]	Horizontal Permeability [mD]	Oil Saturation [frac]	Depth [m RKB]	Porosity [frac]	Horizontal Permeability [mD]	Oil Saturation [frac]
2398	0.179	18	0.168	**2485**	0.275	320	0.225	**2557**	0.11	1.2	0.124
2399	0.183	55	0.291	**2486**	0.302	2220	0.21	**2558**	0.091	8.9	0.131
2400	0.277	440	0.21	**2487**	0.279	1440	0.249	**2562**	0.286	170	0.202
2401	0.234	520	0.228	**2488**	0.271	1140	0.24	**2563**	0.184	3.5	0.101
2402	-		0	**2489**	0.273	310	0.197	**2564**	0.235	105	0.168
2406	0.127	0.3	0	**2489.75**	0.253	600	0.276	**2565**	0.303	260	0.158
2407	0.267	120	0.198	**2490**	0.255	560	0.202	**2566**	Rubble		0.215
2408	0.277	1070	0.209	**2491**	0.052	0.06	0.127	**2567**	0.286	5070	0.25
2409	0.209	38	0.181	**2493**	0.134	0.05	0.029	**2573**	-		0
2412	0.278	290	0.252	**2494**	0.265	240	0.186	**2573.25**	0.251	7	0.017
2413	0.269	405	0.216	**2495**	0.263	196	0.201	**2574**	0.276	650	0.111
2414	0.285	810	0.258	**2496**	0.095	0.4	0.211	**2575**	Preserved Sample		0.132
2415	0.282	1870	0.246	**2497**	0.243	1170	0.187	**2576**	0.286	1460	0.115
2416	0.257	750	0.318	**2498**	Preserved Sample		0.205	**2577**	0.284	1580	0.133
2418	0.182	2.2	0.194	**2499**	0.187	20.03	0.231	**2578**	0.286	2800	0.135
2419	0.15	3.4	0.214	**2502**	0.183	1	0.138	**2579**	0.236	3150	0.186
2424	0.2	2.6	0.277	**2503**	0.178	3.43	0.112	**2580**	0.127	7	0.1
2425	0.201	37	0.278	**2505**	0.219	1.4	0.092	**2585**	0.113	1.4	0.041
2426	0.23	62	0.289	**2506**	Preserved Sample		0.218	**2586**	0.114	1.1	0
2427	0.274	340	0.246	**2507**	0.241	13	0.168	**2587**	0.122	2.53	0
2428	0.287	1800	0.239	**2513**	0.171	2.23	0	**2590**	0.168	13	0.024
2429	0.24	680	0.22	**2516**	0.268	620	0.193	**2591**	0.284	5390	0.061
2430	0.266	180	0.181	**2517**	Rubble		0.085	**2592**	0.238	5080	0.144
2454	0.22	-	0.104	**2518**	Shale		0.093	**2593**	Rubble		0.091
2455	0.147	0.53	0.156	**2519**	0.271	92	0.147	**2606**	0.221	47	0
2456	0.167	13	0.189	**2520**	0.263	330	0.198	**2613**	0.251	8	0
2457	0.109	0.09	0.12	**2521**	0.235	40	0.073	**2617**	0.167	22.03	0
2458	0.258	290	0.206	**2522**	0.254	11	0.139	**2618**	0.132	8.1	0
2459	0.254	550	0.245	**2523**	0.244	22	0.15	**2619**	0.265	49	0
2460	0.294	390	0.182	**2524**	0.235	66	0.04	**2620**	0.274	230	0
2461	0.302	1450	0.264	**2525**	0.243	59	0.194	**2621**	0.187	81	0
2462	0.279	210	0.267	**2526**	0.2	49	0.194	**2622**	0.287	640	0
2463	-		0.228	**2527**	0.183	0.78	0.04				
2463.25	0.281	910	0.285	**2529**	0.202	4.3	0.136				
2464	0.31	1660	0.321	**2530**	0.072	-	0.157				
2465	0.266	145	0.266	**2539**	0.182	2.8	0.128				
2466	0.26	140	0.244	**2540**	0.191	2	0.123				
2467	0.132	0.26	0.254	**2541**	0.211	13	0.105				
2468	0.08	0.2	0.054	**2550**	0.295	830	0.189				
2469	0.187	0.23	0.158	**2551**	0.271	210	0.173				
2470	0.269	96	0.271	**2552**	0.183	9.8	0.169				
2473	-		0.111	**2553**	0.258	195	0.163				
2474	0.199	1.8	0.209	**2554**	0.189	8.5	0.076				
2475	0.271	90	0.272	**2555**	0.219	14	0.077				
2476	0.166	90	0.273	**2556**	0.292	490	0.233				

Appendix C:

Temperature Profile / Data for Well 34/7-1.
Taken and modified from the final well report, provided by the NPD (Saga Petroleum, 1985)

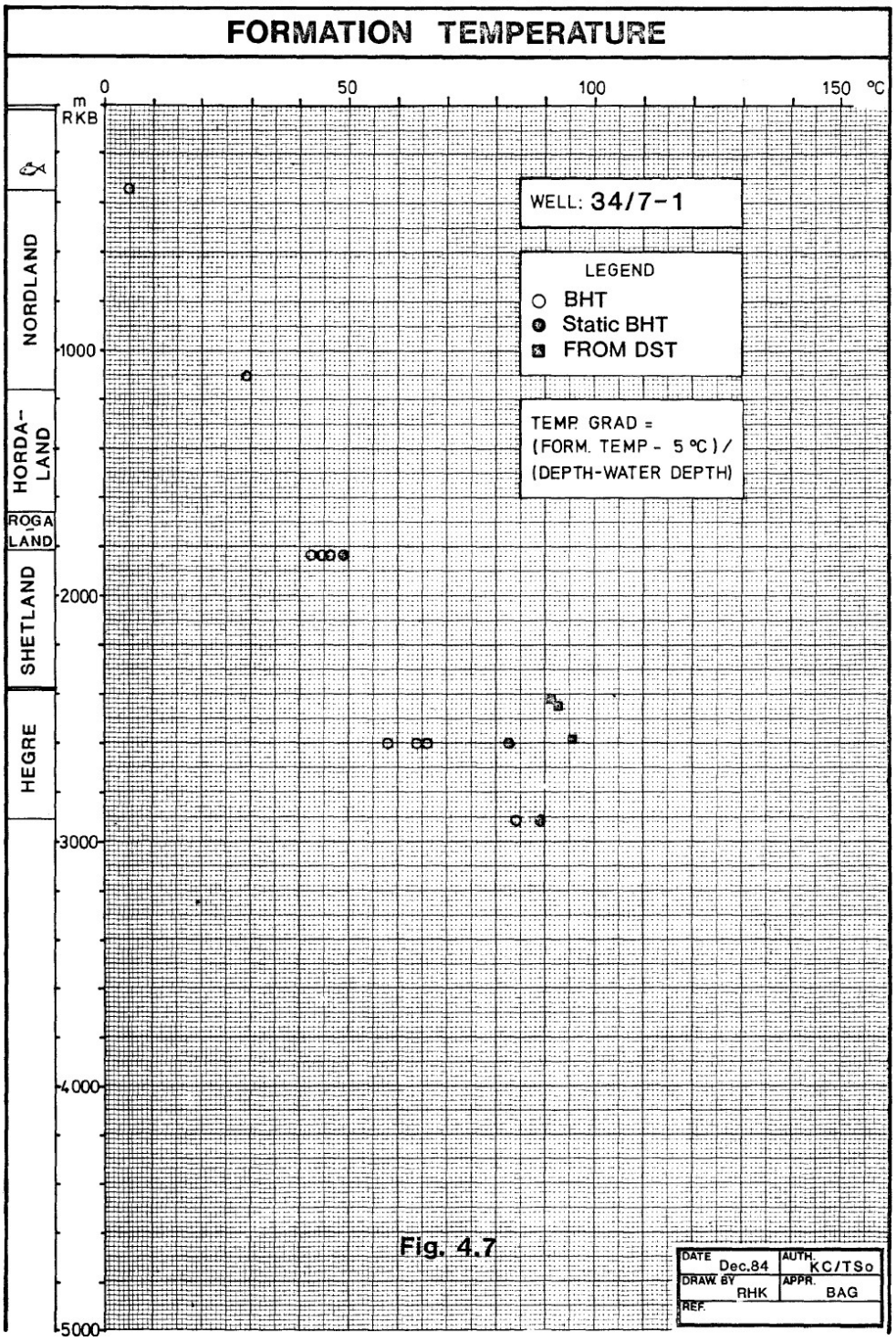

Three measured bottom hole temperatures during testing

Depth [m RKB]	**Temp** [$°C$]
2577.5	95.6
2461	92.2
2412.5	91.1

Average bottom hole temperature (BHT) and statis formation temperatures (T_f)

Depth [m RKB]	**No. of BHT readings**	**Maximum BHT** [$°C$]	T_f [$°C$]
1094.5	3	29	-
1837	3	43	49.5
1846	3	44	
1848	3	46	
2600	3	59	84
2600	3	65	
2600	3	67	
2904	3	84.5	90
2905	3	84.5	
2906	3	86	

Appendix D:

Formation Pressure and Temperature Profile/Data for Well 6704/12-1. Taken and modified from the final well report, provided by the NPD (Aubert et al., 1999)

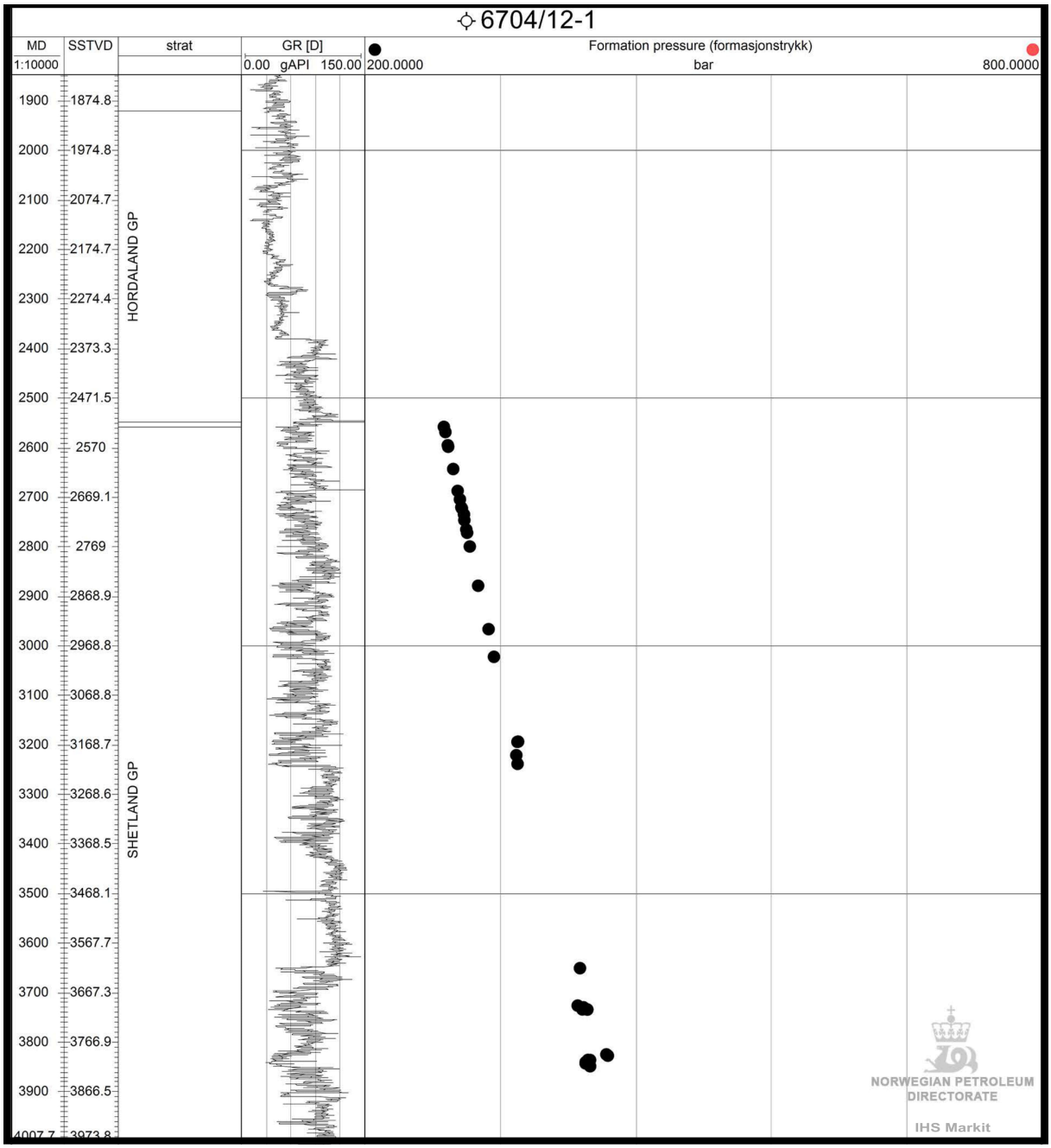

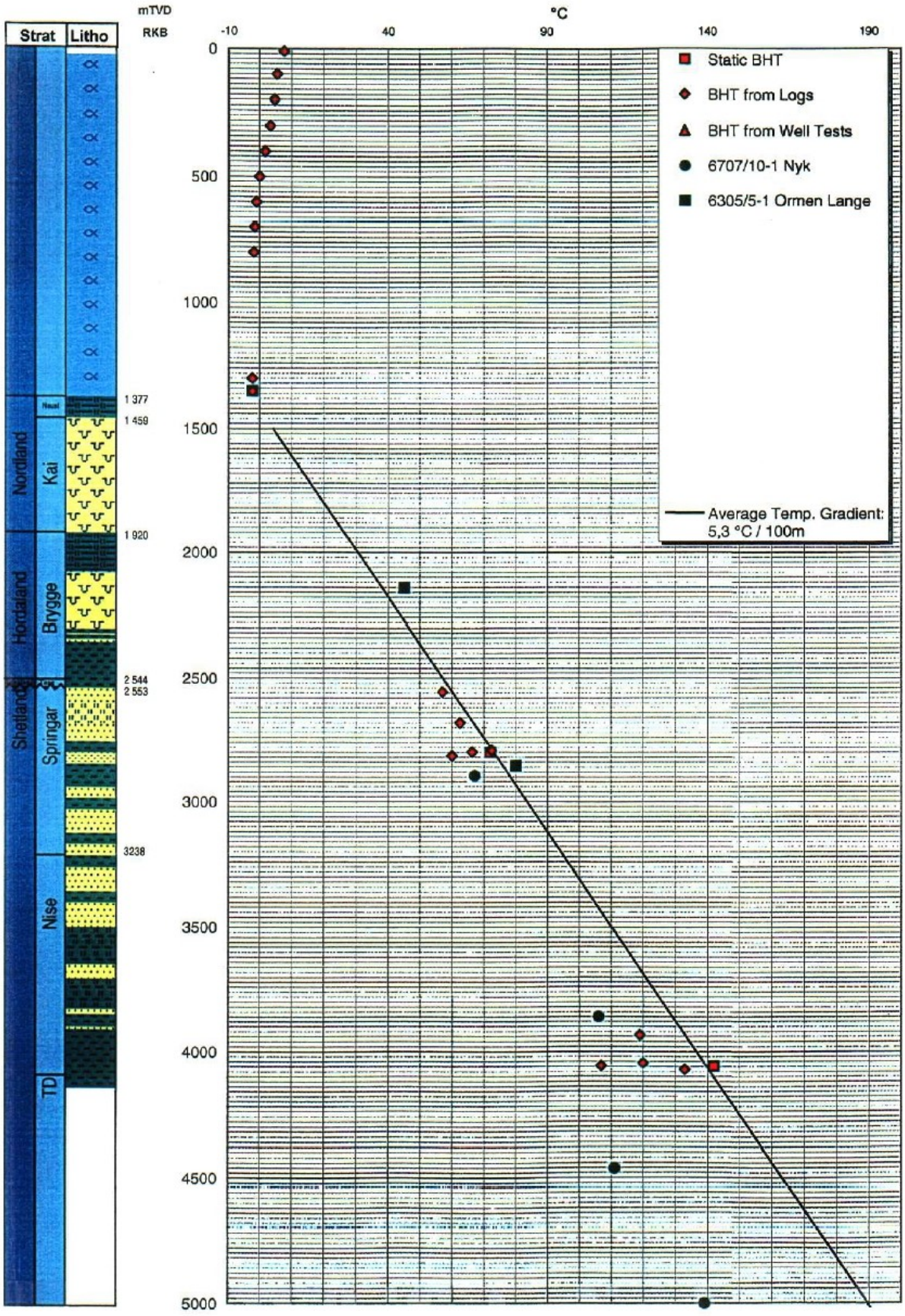
Strat
Litho
mTVD
RKB
°C
-10
40
90
140
190
0
500
1000
1500
2000
2500
3000
3500
4000
4500
5000
Nordland
Kai
Hordaland
Brygge
Shetland
Springar
Nise
TD
Naust
1 377
1 459
1 920
2 544
2 553
3238
Static BHT
BHT from Logs
BHT from Well Tests
6707/10-1 Nyk
6305/5-1 Ormen Lange
Average Temp. Gradient:
5,3 °C / 100m

Formation tester wellsite worksheet for Well 6704/12-1 (Modified from Aubert et al., 1999)

Formation Tester Wellsite Worksheet											
Test No.	**Depth [m RKB]**	**Formation Pressure**		**Temp After [°C]**	**Mobility Index [mD/cP]**	**Test No.**	**Depth [m RKB]**	**Formation Pressure**		**Temp After [°C]**	**Mobility Index [mD/cP]**
		[EMW]	**[Bar]**					**[EMW]**	**[Bar]**		
MDT wellsite worksheet run # 1A						**17**	3828.5	1.061	399.25	119.6	
1	2557.7	1.074	269.899	55.8	297.8	**18**	3835.8	1.049	395.4	120.3	4.2
1	2557.7	1.073	269.866	57	282.3	**19**	3840.1	1.048	395.331	120.1	10.7
2	2568.2	1.075	271.275	57.7	3	**20**	3842.5	1.057	399.321	120.1	92.6
3	2578.7	-	-	58.6	-	**21**	3848.4	-	-	120.3	1.9
4	2594.8	1.072	273.419	59.2	379	**22**	3903	-	-	121	0.7
5	2597.9	1.072	273720	59.6	401	**23**	3905.7	-	-	121.5	0.4
6	2614.8	-	-	60.2	-	**24**	3909.9	-	-	122.1	0.6
7	2616	-	-	60,4	-	**25**	3925	-	-	122.3	1.9
8	2642.8	1.071	278.165	61.1	7	**26**	3960	-	-	123.4	-
9	2687	1.069	282.099	62,5	16	**27**	3961	-	-	123.9	-
10	2704	l.069	284.085	63.7	2	**28**	3960.5	-	-	124.2	-
11	2720.2	1.068	285.35	64.6	13	**29**	3908.5	-	-	124	-
12	2722.5	1.069	285.889	65.3	4.3	**30**	3907.5	-	-	123.4	-
13	2734.5	1.071	287.72	66.3	4	**31**	3906.5	-	-	122.9	-
14	2746	1.068	288.012	67.3	53	**32**	3904.5	1.048	395.329	122.8	-
15	2765	1.067	289.727	68.8	95	**33**	3842.5	-	-	121.4	-
16	2771.5	1.067	290.46	70.3	82	**MDT wellsite worksheet run # 2C**					
17	2799.2	1.065	292.868	72.4	251	**1**	3840.8	1.049	395.451	127.9	39.4
18	2425.5	-	-	63.2	-	**2**	3840.7	1.049	395.447	127.8	4
MDT wellsite worksheet run # 2B						**3**	3840.6	-	-	127.7	-
1	2878.4	1.062	300.238	84.2	12.3	**4**	3842.4	1.049	395.536	127.7	8.9
2	2966.1	1.062	309.479	86.3	2.1	**5**	3842.5	1.049	395.532	128.1	18,0
3	3021.9	1.059	314.21	90	3.8	**6**	3842.6	1.048	395.315	128	50.5
4	3193.1	1.07	335.58	91.6	0.2	**7**	3960.7	-	-	133.5	0.5
5	3193.6	1.068	335	95.7	0.3	**8**	3924.7	-	-	132	5.9
6	3220.5	1.056	334.018	97.8	7.7	**9**	3909.8	-	-	131.6	0.9
7	3238	1.054	335.116	98.2	12.7	**10**	3907.2	-	-	131.1	4.4
8	3650.4	1.089	390.334	111.4	-	**11**	3905.4	-	-	131	4
9	3698.5	-	-	115.3	-	**12**	3902.7	-	-	130.9	0.9
10	3726	1.062	388.306	116.1	1.4	**13**	3835.6	1.056	397.49	130.1	6.1
11	3733.5	1.082	396.58	116.7	0.7	**14**	3733.6	1.071	392.47	127.9	-
12	3734	1.083	396.85	117.2	0.4	**15**	3729.5	1.075	393.427	126.8	0.3
13	3752	-	-	117.8	-						
14	3823	-	-	118.6	-						
15	3824.5	1.102	413.67	119.3	0.1						
16	3827	1.105	415	119.6	0.4						

Appendix E:

Formation pressure profile/data for Well 7220/8-1
Taken and modified from the NPD fact pages for Well 7220/8-1

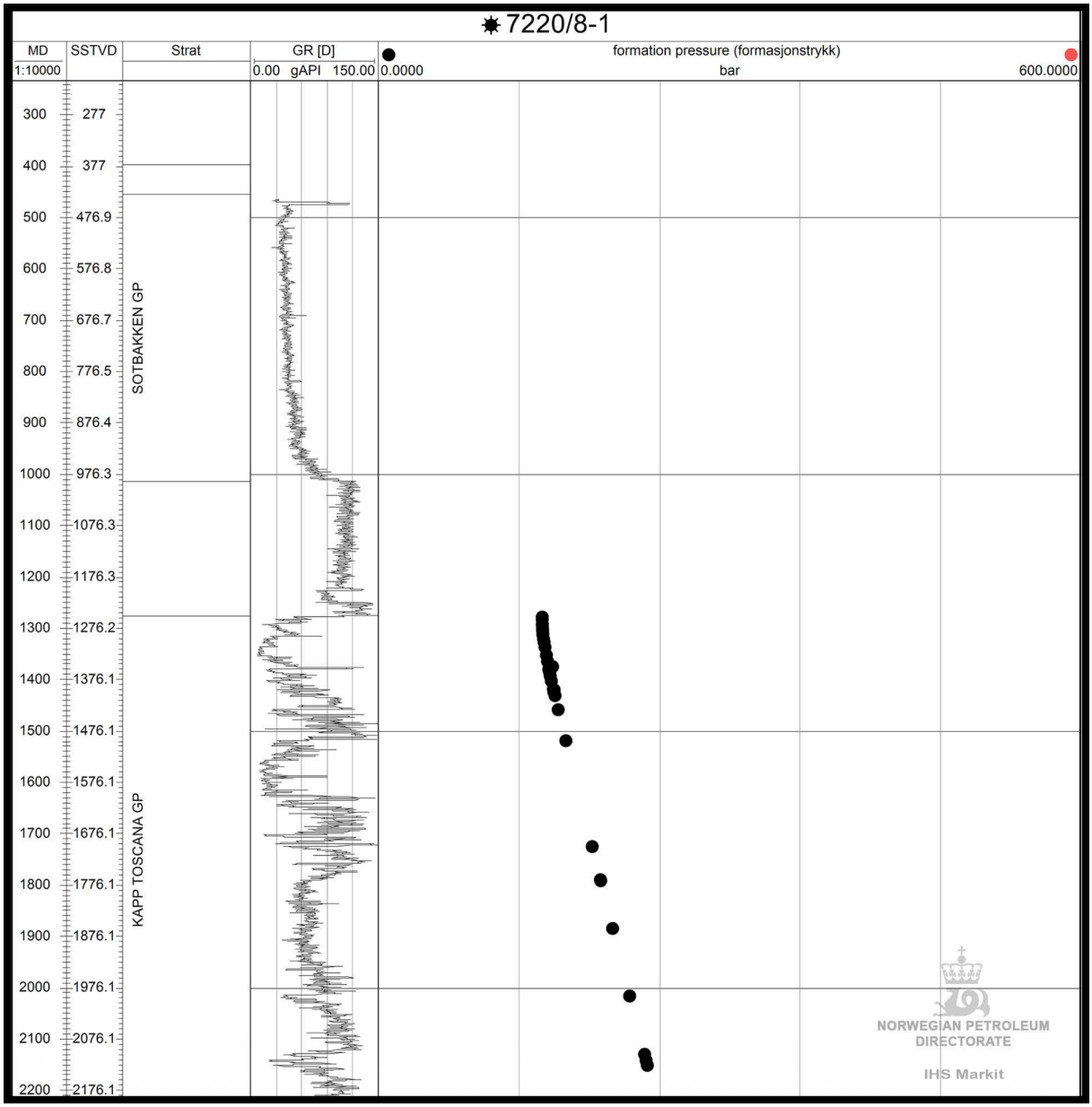

The exact values for the formation pressure from the previously shown stress profile is not available. The following values are obtained from digitize the available stress profile.

Depth [m RKB]	**Formation Pressure [Bar]**
1289.428	140.0273
1323.124	140.4181
1356.74	143.2742
1388.096	146.6633
1423.489	149.6213
1458.987	153.1074
1522.175	160.1651
1726.496	182.7726
1791.294	189.8018
1884.47	200.2506
2014.861	214.689
2141.946	228.5575

Appendix F:

Formation temperature data for Well 7220/8-1
Taken and modified from the Geochemistry report, provided by the NPD

Only oil samples were collected in this well. Schlumberger MDT single probe was used for all samples. 12 MDT sample chambers were filled with oil for analysis.

Sample Station No.	Depth [m MD RT]	Chamber Number	Chamber Volume	Temp [$^{\circ}C$]	Drawdown [Bar]	Max shut-in Pressure [Bar]
1	1336.8	MPSR#2826	420 cc	36.0	1.7	473.8
	1336.8	MPSR#4687	420 cc	36.0	1.6	472.8
	1336.8	MPSR#4367	420 cc	36.0	1.6	473.8
	1336.8	MPSC#419	1 gallon	36.0	1.7	471.8
2	1320.6	MPSR#4550	420 cc	35.5	4.4	474.8
	1320.6	MPSR#4692	420 cc	35.5	4.4	474.8
	1320.6	MPSR#4357	420 cc	35.5	4.2	474.8
	1320.6	MPSC#496	1 gallon	35.5	4.7	474.8
3	1380.5	MPSR#	420 cc	37.5	3.2	429.0
	1380.5	MPSR#	420 cc	37.5	3.2	429.0
	1380.5	MPSR#	420	37.5	3.2	429.0
	1380.5	MPSR#	420	37.5	3.2	429.0

Appendix G:

MATLAB function for log extrapolation to the seafloor

log_2_sea_level_new_2.m

```
%%
%
%% Code written by Kenneth Duffaut. Use of this SOFTWARE is for non-profit organization such as education and reserach
%
%
%
% Model for mergeing logs from start log to seabed, i.e. Vp and RhoB
%
 function [x_log_merge,z_log_merge] = ...
       log_2_sea_level_new_2(z_water,x_water,x_seabed,x_log,z_log,top_merge,gammabefore,gammaafter);
%
% Log depth in TVD MSL in meters
%
%  save('sangussi.mat','z_water','x_water','x_seabed','x_log','z_log','top_merge','gammabefore','gammaafter');
%%
 x_log(:); % Force vector to be vertical nx1
 z_log(:); % Force vector to be vertical nx1
%%
% Resample logs with a sample rate in depth 0.1524 m. Both new depth (new_tvdmsl) and
% property log (new_x)
%
 new_tvdmsl = [0:0.1524:max(z_log)]';
 new_x = zeros(length(new_tvdmsl),1);
 new_x = new_x.*0 - 999.250;
 new_x = interp1(z_log,x_log,new_tvdmsl,'linear'); %
%%
% Fill holes
%
 id_seabed = find(new_tvdmsl <= (z_water + 0));
 new_x(id_seabed) = -999.250; % -999.250
%
 new_x(new_x < 0) = nan; % Insert NaN values
%%
 id_nonan = find(isnan(new_x) == 0); % Find real values
%
 [xlout,zout] = fillholes(new_x,'linear',30); % default is 10 samples
 x_log_merge = zeros(length(xlout),1);
 x_log_merge = xlout;
%
 x_log_merge(1:id_nonan(1)-1) = nan; % Insert NaN values from top of log to seabed
 x_log_merge(id_nonan(end)+1:end) = nan; % Insert NaN values from base of log to TD

%%
% Water layer
%
 x_log_merge(id_seabed) = x_water; % Property of the water layer
%
% Seafloor to top of log
%
 id_merge = find(new_tvdmsl > top_merge); % Find depth in TVD/MSL to do the log merge
 merge_log = id_merge(1); % This is depth in TVD MSL
%
 nonan_xlog_top = x_log_merge(merge_log);
 nonan_zlog_top = new_tvdmsl(merge_log);
 id_overburden = find(new_tvdmsl > (new_tvdmsl(id_seabed(end)) + 0) & new_tvdmsl <= new_tvdmsl(merge_log));
%%
% Insert model of overburden
%
 [x_deep] = merge_log_seabed(x_seabed,nonan_xlog_top,((nonan_zlog_top - z_water)/1e3),gammabefore);
 x_log_merge(id_overburden) = x_deep - (x_deep - x_seabed).*exp(-gammabefore*((new_tvdmsl(id_overburden) - ...
       z_water)/1e3)); % km TVD BSF
%%
% End log measurments to end depth of log
%
 nonan_xlog_base = new_x(id_nonan(end));
 nonan_zlog_base = new_tvdmsl(id_nonan(end));
 id_underburden = find(new_tvdmsl > nonan_zlog_base & new_tvdmsl <= z_log(end));
%%
% Insert model of underburden
%
 [x_deep] = merge_log_seabed(x_seabed,nonan_xlog_base,((nonan_zlog_base - z_water)/1e3),gammaafter);
 x_log_merge(id_underburden) = x_deep - (x_deep - x_seabed).*exp(-gammaafter*((new_tvdmsl(id_underburden) - ...
       z_water)/1e3)); % km TVD BSF
%%
%
%
 z_log_merge = new_tvdmsl;
%
 end
```

merge_log_seabed.m

```
%%
%
%% Code written by Kenneth Duffaut. Use of this SOFTWARE is for non-profit organization such as education and reserach
%
%
%
% Model can be used for both Vp and RhoB
%
 function [x_deep] = merge_log_seabed(x_seabed,x_log,z_log,gamma)
%
%% x_seabed = value you want to use at the seabed. Can be velocity (in km/s) or density (in g/cc)
%
%% x_log = value at the top of the wireline log. Can be velocity (in km/s) or density (in g/cc)
%
%% z_log = depth to either the top or base well log to be merged. TVD Below Sea Floor in (km)
%
%% gamma = value controls the slope of the expontional decay.
%
%% x_deep = value to estimated to fit either the vaule at the top or
%%          base of the log. Can be velocity (km/s) or density (g/cc)
%
%% Shallow depth use a gamma between 8 to 10. I use 8
%
%% Deep depth, use a gamma between 1 to 3. I use 2
%
% P-wave velocity in shallow sediments. Use either of these as x_seabed
%     Soft wet shale = 1.550 km/s
%     Soft wet sand = 1.700 km/s
%
% Density in shallow sediments. Use either of these as x_seabed
%     Soft wet shale = 1.5 - 1.7 g/cc
%     Soft wet sand = 1.9 - 2.0 g/cc
%%
% The x_deep is the phsyical value to be estimated from the values of
% either the top og base of the log
%
    x_deep = (x_log - x_seabed*exp(-gamma.*z_log))./(1 - exp(-gamma.*z_log));
%
 end
```

Appendix H:

MATLAB function for Batzle and Wang (1992) Approach

flprop.m

```
function [Kreuss,rhoeff,Kvoigt,vpb,rhob,Kb,vpo,rhoo,Ko,vpg,rhog,Kg,gor]=flprop(method,sal,og,gg,gor,giib,giio,P,T,So,Sg)
% FLPROP - Batzle-Wang relations for reservoir fluid properties
%
%[Kreuss,rhoeff,Kvoigt,vpb,rhob,Kb,vpo,rhoo,Ko,vpg,rhog,Kg,gor]
%                              =flprop(method,sal,og,gg,gor,giib,giio,P,T,So,Sg)
%
% vpb,vpo,vpg: Vp of brine, oil, and gas in km/s
% rhob, rhoo, rhog: Density of brine, oil, and gas in g/cc
% Kb, Ko, Kg: Bulk Moduli of brine, oil, and gas in GPa
% rhoeff: effective density of mixed fluid
% Kreuss: Reuss bound of mixed fluid's bulk modulus, homogeneous saturation
% Kvoigt: Voigt bount of mixed fluid's bulk modulus, patchy saturation
%%
% method: 1, use Gas Index in Oil other numbers, use GOR (L/L)
% sal: NaCl Sal (e.g. 34000 ppm)
% og: Oil Gravity (e.g. 30 API number)
% gg: Gas Gravity (e.g. 0.6 Specific Gravity)
% gor: Gas Oil Ratio (L/L), e.g. 100
% giib: Gas Index in Brine, e.g. 0
% giio: Gas Index in Oil, e.g. 0
% P: Pore Pressure    (MPa)
% T: Rock Temperature (oC)
% So: Saturation of oil, between 0 and 1
% Sg: Saturation of gas, between 0 and 1
%%
% Sb = 1-So-Sg: Saturation of water
%
% See also FLPROPUI

% The results have been compared with Petrotools results.
% The errors are within 0.2%, and maybe caused by the precision in Petrotools.

% Written by Li Teng (1997)

% salinity is in ppm divided by 1e6
 sal = sal./1e6;

% ideal gas constant
 R = 8.31441; % J/g-mole deg
%%
% gas density=====================================================================
 Pr = P./(4.892 - 0.4048.*gg);
 Tr = (T + 273.15)./(94.72 + 170.75.*gg);
 E = 0.109.*(3.85 - Tr).^2.*exp(-(0.45 + (8.*(0.56 - 1./Tr).^2)).*(Pr.^1.2./Tr));
 Z = (0.03 + 0.00527.*(3.5 - Tr).^3).*Pr + (0.642.*Tr - 0.007.*Tr.^4 - 0.52) + E;
 rhog = (28.8.*gg.*P)./(Z.*R.*(T + 273.15));
%%
% gas adiabatic bulk modulus=======================================================
 gamma = 0.85+5.6./(Pr+2)+27.1./(Pr+3.5).^2-8.7.*exp(-0.65.*(Pr+1));
 f = E.*1.2.*(-(0.45+8.*(0.56-1./Tr).^2).*Pr.^0.2./Tr)+(0.03+0.00527.*(3.5-Tr).^3);
 Kg = P.*gamma./(1-Pr./Z.*f)./1000;
 vpg = sqrt(Kg./rhog);
%%
% oil density=====================================================================
 rho0 = 141.5./(og + 131.5);
%%
% calculate GOR for method 1
 if (method == 1)
   gormax = 2.03.*gg.*(P.*exp(0.02878.*og-0.00377.*T)).^1.205;
   gor = gormax.*giio;
 end
%%
% dead oil vs. live oil
 if (gor == 0)
   rhoog = rho0;
   rhop = rhoog + (0.00277.*P-1.71e-7.*P.^3).*(rhoog - 1.15).^2 + 3.49e-4.*P;
   rhoo = rhop./(0.972 + 3.81e-4.*(T + 17.78).^1.175);
 else
   B0 = 0.972 + 0.00038.*(2.4.*gor.*sqrt(gg./rho0) + T + 1.78).^1.175;
   rhoog = (rho0 + 0.0012.*gg.*gor)./B0;
   rhoo = rhoog + (0.00277.*P - 1.71e-7.*P.^3).*(rhoog - 1.15).^2 + 3.49e-4.*P;
 end
%%
% oil velocity====================================================================
% live oil use pseudo density
 if (gor≠0)
   rho0 = rho0./B0./(1 + 0.001.*gor);
 end
% the following formula is for dead oil only
%vpo=15450./sqrt(77.1+og)-3.7.*T+4.64.*P+0.0115.*(0.36.*sqrt(og)-1).*T.*P;
% the following formula is for dead oil and live oil
 vpo = 2096.*sqrt(rho0./(2.6 - rho0)) - 3.7.*T + 4.64.*P + 0.0115.* ...
```

```
 (4.12.*sqrt((1.08./rho0) - 1) - 1).*(T.*P);
 vpo = vpo./1000;
 Ko = (vpo.^2).*rhoo;
%%
% brine density============================================================
 rhow = 1 + 1e-6.*(-80.*T - 3.3.*T.^2 + 0.00175.*T.^3 + 489.*P - 2.*T.*P + 0.016.*T.^2.*P - 1.3e-5.*T.^3.*P - ...
       0.333.*P.^2 - 0.002.*T.*P.^2);
 rhob = rhow + sal.*(0.668 + 0.44.*sal + 1e-6.*(300.*P - 2400.*P.*sal + T.*(80 + 3.*T - 3300.*sal - 13.*P + ...
       47.*P.*sal)));
%%
% brine velocity===========================================================
 matrixw = [1402.85 4.871 -0.04783 1.487e-4 -2.197e-7
 1.524 -0.0111 2.747e-4 -6.503e-7 7.987e-10
 3.437e-3 1.739e-4 -2.135e-6 -1.455e-8 5.230e-11
 -1.197e-5 -1.628e-6 1.237e-8 1.327e-10 -4.614e-13]';
%%
% water velocity
 velw = 0;
 for i = 1:5
   for j = 1:4
     velw = velw + matrixw(i,j).*T.^(i-1).*P.^(j-1);
   end
 end
%%
% gas water ratio
 gwrmax = 10.^(log10(0.712.*P.*(abs(T-76.71)).^1.5+3676.*P.^0.64)-4- ...
 7.786.*sal.*(T+17.78).^(-0.306));
 gwr = gwrmax.*giib;
%%
% gas-free brine and brine with gas
 vpb0 = velw+sal.*(1170-9.6.*T+0.055.*T.^2-8.5e-5.*T.^3+2.6.*P- ...
 0.0029.*T.*P-0.0476.*P.^2)+sal.^1.5.*(780-10.*P+0.16.*P.^2)-1820.*sal.^2;
 vpb = vpb0./(sqrt(1+0.0494.*gwr));
 vpb = vpb./1000;
 Kb = vpb.*vpb.*rhob;
%%
% fluid mixer==============================================================
% Effective density
 Sb = 1 - (So + Sg);
 rhoeff = Sb.*rhob + So.*rhoo + Sg.*rhog;
%%
% Reuss Average
 if ( Kb.*Ko.*Kg~=0 )
   Kreuss = 1./(Sb./Kb + So./Ko + Sg./Kg);
 elseif (Sb==0)
   Kreuss = 1./(So./Ko + Sg./Kg);
 elseif (So==0)
   Kreuss = 1./(Sb./Kb + Sg./Kg);
 elseif (Sg==0)
   Kreuss = 1./(Sb./Kb + So./Ko);
 else
   Kreuss = 0;
 end
%%
% Voigt Average
 Kvoigt = Sb.*Kb + So.*Ko + Sg.*Kg;
 end
```

Nandito Davy

Velocity Depth Trends Prediction on the Norwegian Continental Shelf Wells Using the Bounding Average Method

NTNU
Norwegian University of
Science and Technology